UNIVERSITATEA BABEŞ-BOLYAI
BABEŞ-BOLYAI TUDOMÁNYEGYETEM
BABEŞ-BOLYAI UNIVERSITÄT
BABEŞ-BOLYAI UNIVERSITY
TRADITIO ET EXCELLENTIA

CHEMIA

STUDIA UNIVERSITATIS BABEȘ-BOLYAI CHEMIA

4/2023

S T U D I A
UNIVERSITATIS BABEŞ–BOLYAI
CHEMIA

4

CONTENT/ SOMMAIRE/ INHALT/ CUPRINS

Studia Universitatis Babes-Bolyai Chemia has been selected for coverage in Thomson Reuters products and custom information services. Beginning with V. 53 (1) 2008, this publication is indexed and abstracted in the following:

- Science Citation Index Expanded (also known as SciSearch®)
- Chemistry Citation Index®
- Journal Citation Reports/Science Edition

STRUCTURAL AND OPTICAL INSIGHTS INTO A PHENOTHIAZINE-DERIVED CHALCONE SYNTHESIZED VIA ECO-FRIENDLY METHODS

Stefana GRAMA[a], Bianca STOEAN[a,*], Alexandru TURZA[b], Dan PORUMB[a], Castelia CRISTEA[a], and Luminita SILAGHI-DUMITRESCU[a]

ABSTRACT. A novel chalcone containing (hetero)aromatic units was obtained by the Claisen-Schmidt condensation of phenothiazinyl-3-carbaldehyde with 4-hydroxy-acetophenone under three experimental approaches based on classical, mechanochemical and ultrasound-assisted procedures. A comparison between the experimental outcomes emphasizes shorter reaction time and lower energy usage in the case of mechanochemical and ultrasound-assisted procedures, recommending these methods as more environmentally friendly synthetic options. Moreover, the use of the sonochemical method resulted in the formation of the reaction product in crystalline state thus simplifying the purification process. The optical properties of the new chalcone were assessed by UV-vis spectroscopy. (E)-1-(4-hydroxyphenyl)-3-(10-methyl-10H-phenothiazin-3-yl)prop-2-en-1-one exhibited an intense absorption in the UV region (λ_{max}=408 nm) and low intensity fluorescence emission in DMSO solution (λ_{em}=560 nm, Stokes shift 7558 cm^{-1}). The X-ray diffraction on monocrystal technique which was employed to ascertain the solid-state structure of the new chalcone revealed strong O-H···O hydrogen bonds and weak dispersive van der Waals interactions such as π···π and C-H···π contacts ensuring its supramolecular architecture, crystal cohesion and stability.

Keywords: *Phenothiazine; Chalcone; Sonochemistry; Mechanochemistry, UV-vis spectroscopy, XRD.*

---

a   *Babeş-Bolyai University, Faculty of Chemistry and Chemical Engineering, 11 Arany Janos str., RO-400028, Cluj-Napoca, Romania*
b   *Department of Mass Spectrometry, Chromatography and Applied Physics, National Institute for Research and Development of Isotopic and Molecular Technologies, 67-103 Donat str., RO-400293 Cluj-Napoca, Romania*
*   *Corresponding author: bianca.stoean@ubbcluj.ro*

STEFANA GRAMA, BIANCA STOEAN, ALEXANDRU TURZA, DAN PORUMB,
CASTELIA CRISTEA, LUMINITA SILAGHI-DUMITRESCU

INTRODUCTION

In the last decades, the chemistry of methine dyes has received increasing interest because of the wide range of uses and applications of these dyes in many sectors such as technology, engineering, pharmacology, and medicine [1]. Cyanines, a classes of methine dyes, found various applications such as acid-base indicators in analytical chemistry, anti-tumor and anti-cancer agents, bactericidal and fungicidal agents in medicine [2]. Additionally, they are exploited in nucleic acids or protein detection, biomolecules labeling and laser technology [2].

Besides cyanines, another intensively studied class of methine dyes is represented by chalcones. Chalcones are biologically active diaryl-α,β-unsaturated carbonyl compounds, being precursors of various heterocyclic compounds [3]. Chalcones serve as a pharmacophore in a variety of physiologically active compounds and have multiple uses, including anticancer [4], anti-inflammatory and antioxidant compounds [5]. Some chalcone-isoflavone dimers have shown promising results in being used as anti-inflammatory, and some phenyl coumarins and chalcones were proposed as suppressors of LTR-dependent transcription in 2007–in an attempt to find new anti-HIV treatments however, the mechanism of action has not been fully characterized [6]. Keeping the same principles as the previous anti-HIV active compounds, in 2016, Cole et al. synthesized some butein- and xanthohumol-based chalcones that have shown promising results in anti-HIV studies [7].

Despite the fact that chalcones have great promise as medicinal agents, this class of compounds is also renowned for their photochemical, optical, and non-linear optical characteristics (NLO), being employed as fluorophores in Organic Light-Emitting Diodes (OLED) [8], chemosensors, and fluorescent nano-probes [9]. By integrating optical characteristics with biocompatibility and biological functionality, chalcones can effectively serve as fluorescent labels in cellular imaging for the identification of tumor tissue (B16-F10 murine melanoma) [10] and specific staining of cellular organelles [11], cell nucleus and the intercalation between the nitrogenous bases of the nucleus [12]. High selectivity towards mitochondria was observed with fluorescent probes based on polyfluorinated cyanine dyes, polymethine dyes, and the cyanine-benzothiazole hybrid system, which emitted predominantly in the near infrared region [10]. Selective labelling was performed on the lysosomes of various cell lines, including HF-P4, BLM, U-2 OS, and A-2058, using fluorescent Coumarin Troger's base derivatives with cyanine substituents [13]. The cytoplasm was selectively stained through the use of a variety of organic dyes. As an illustration, boron-based Schiff bases complexes were effectively utilized to stain the cytoplasm

of B16-F10 murine melanoma cells in vitro [14]. Similarly, live mouse embryonic fibroblasts were selectively stained with fluorophores that contained thiophene moieties [15].

In our quest for more environmentally benign methods applicable in the synthesis of heterocyclic compounds, previous studies focused on the condensation of 10-methyl-10*H*-phenothiazine-carbaldehyde under microwave assisted conditions pointed out superior reaction rates and product yields in the preparation of Schiff bases [16], acetals [17] and chalcones [18-20] containing phenothiazine units, as well as in the synthesis of their oxidation [21] or cyclization [22] products. Building upon our prior research regarding the application of other greener methodologies in the syntheses of (phenothiazinyl)vinyl dyes [10,23,24], in this work we developed two alternative experimental procedures for the condensation of phenothiazinyl-3-carbaldehyde with acetophenone derivatives under mechano- and sonochemical conditions. The structure of the novel phenothiazinyl-chalcone was assigned unambiguously by NMR and XRD, while its optical absorption/ emission properties were assessed by UV-vis spectroscopy.

RESULTS AND DISCUSSION

(*E*)-1-(4-hydroxyphenyl)-3-(10-methyl-10*H*-phenothiazin-3-yl)prop-2-en-1-one **2**, was obtained by the condensation of 10-methyl-10*H*-phenothiazine-3-carbaldehyde **1** with 4-hydroxy acetophenone according to Scheme 1.

a) Ethanol, KOH, 60 °C, 24h	33%
b) Grinding, KOH, 30min	20%
c) Ethanol, KOH, 3h,))	47%
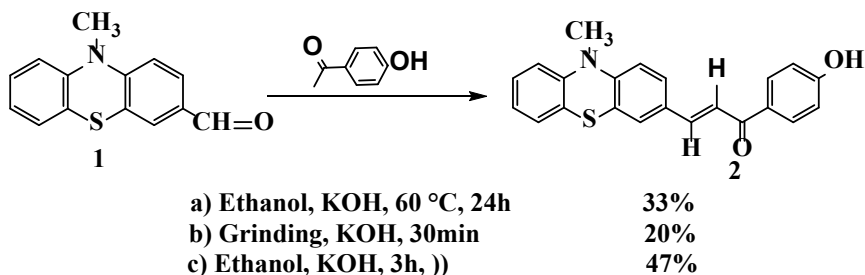
Scheme 1.

Three alternative experimental procedures were tested to optimize the reaction conditions: a) classical convective heating in a homogeneous ethanol solution, b) solvent-free mechanochemical conditions and c) ultrasound irradiation conditions. Notwithstanding the fact that the reaction yields achieved

through the implementation of mechano- and sonochemical conditions were lower (20% mechanochemical) or not too much higher (47% sonochemical) than those achieved through conventional methods (33%), these alternative processes can be deemed "greener" due to their significantly reduced energy consumption and shorter reaction time (30-180 minutes *versus* 24 hours). Furthermore, the ultrasound-assisted procedure yielded a crystalline reaction product that required only simple purification and finally provided single crystals suitable for X-ray diffraction.

The *E* configuration of the C=C bond present in the chalcone **2** structure was suggested by high resolution NMR based on a large vicinal coupling constant between the protons attached to the vinyl unit (^3J=15.48 Hz) and conclusively confirmed by the recorded XRD pattern in the monocrystal.

The optical properties of **2** displayed a weak solvatochromism as it may be seen from the data listed in **Table 1** emphasizing the absorption/emission wavelength maxima in various solvents. **Figure 1a** reveals the slight bathochromic shift (806.7 cm^{-1}) recorded in the UV-vis absorption spectrum of **2** when transitioning from ethyl acetate or toluene to dimethylsulfoxide (DMSO)- a solvent recognized for its stabilizing capacity *via* hydrogen bonding. A broad fluorescence emission band was recorded upon excitation of **2** with its longest absorption maxima (**Figure 1b**); the most intense fluorescence emission and the highest value of the Stokes shift were recorded for chalcone **2** in the polar aprotic solvent acetone, while the fluorescence emission was quenched in DMSO solvent which apparently favored the non-radiative relaxation processes.
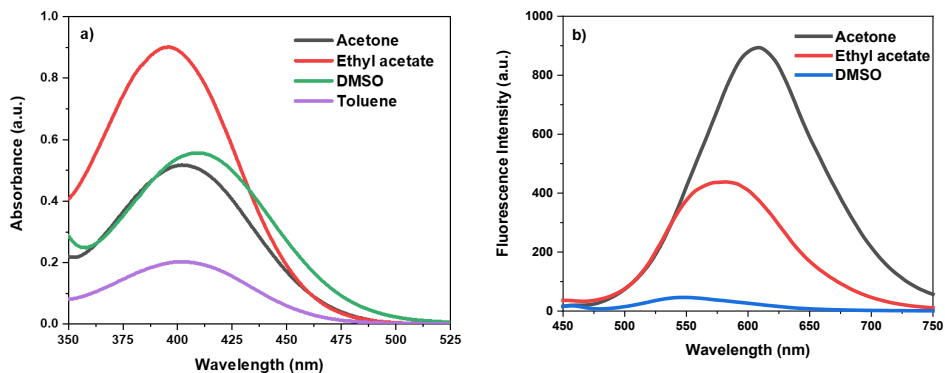
Figure 1. UV-vis spectra of chalcone **2** in various solvents: a) absorption spectra (C_M=4x10^{-5}M), b) fluorescence emission spectra (C_M=8x10^{-7}M).

Table 1. UV-vis absorption/emission wavelength maxima, molar extinction
coefficients and Stokes shifts of chalcone **2** in various solvents.

Solvent	λ_{abs} (nm)	ε ($cm^{-1}M^{-1}$)	λ_{em} (nm)	Stokes Shift (cm^{-1})
Acetone	400	1.3×10^4	607	8526
Ethyl acetate	395	2.2×10^4	577	7986
DMSO	408	1.3×10^4	560	7558
Toluene	400	0.5×10^4	-	-

The crystal structure of **2** within solid state was completely elucidated
by single crystal X-ray diffraction technique. It crystallizes centrosymmetrically
in the body-centered I2/a monoclinic space group. The structure is embedding
isopropyl alcohol molecules in the lattice in a stoichiometric ratio of 1:1 between
chalcone **2** and alcohol. The molecular perspective of the asymmetric unit
along with the atom numbering scheme is presented in **Figure 2a**.

In the formation of supramolecular architectures, crystal cohesion
and stability are involved strong classical O-H···O hydrogen bonds and other
weak dispersive van der Waals interactions such as π···π and C-H···π contacts
(see table 2). An isopropyl alcohol molecule is bounded within the lattice by
O-H···O hydrogen bonds, the hydroxyl group of alcohol molecule serving
both as donor and acceptor. O2-H2A···O3 interaction is characterized by a
separation distance of 1.951 Å linking the hydroxyl group of the alcohol with the
carbonyl group of the chalcone. Further the alcohol molecule is involved in
hydrogen bonds with the hydroxyl substituent of the aromatic ring, the recorded
O1-H1···O2 distance being 1.863 Å. Both phenyl rings of phenothiazine
moiety participate in mutual π···π interactions characterized by intermolecular
C4···C7 distances of 3.365 Å. These are completed by C-H···π interactions
linking isopropanol molecule to chalcone **2** adjacent molecules. An extended
packing diagram of compound **2** is illustrated in Figure 2b.

Table 2. Intermolecular interactions in compound **2** (Å).

D-H···A	D-H	H···A	D···A	<(D-H···A)
O1-H1···O2	0.820	1.863(3)	2.765(4)	170.2(4)
O2-H2···O3	0.820	1.951(2)	2.271(1)	177.8(4)
π···π				
C4···C7			3.365(4)	
C-H···π				
C22-H22···C1	0.930	2.859(3)	3.546(2)	131.7(2)
C24-H24···C19	0.980	2.837(4)	3.731(2)	151.8(2)

(a)

(b)
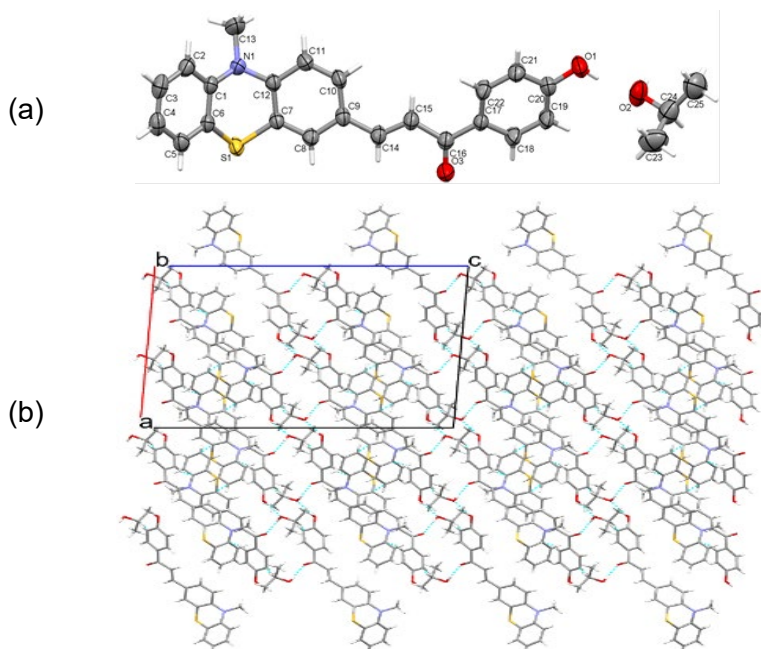
Figure 2. Chalcone **2** a) ORTEP illustration of the asymmetric unit presenting the atoms as ellipsoids at 50% probability level; b) packing perspective along ab-axis.

CONCLUSIONS

This work described three alternative experimental procedures applicable in the synthesis of (*E*)-1-(4-hydroxyphenyl)-3-(10-methyl-10H-phenothiazin-3-yl)prop-2-en-1-one **2**, based on i) the conventional convective heating in homogeneous solution, ii) the solventless mechanochemical grinding and iii) the ultrasound irradiation techniques. The mechano- and sonochemical procedures may be qualified as greener synthetic approaches requiring much shorter reaction times and lower energy inputs. A major advantage of the sonochemical procedure is its capacity to induce the precipitation of the reaction product in a solid microcrystalline state, much simplifying its purification. The electronic properties of **2** displayed a strong absorption peak in the UV region (408 nm) and fluorescence emission in the visible range (560 nm) of low intensity but large Stokes shift 7558 cm^{-1}).

EXPERIMENTAL SECTION

Materials and Methods

All the materials for experiments, reagents, and solvents were obtained from commercial suppliers and used without further purification unless otherwise noted. UV-vis absorption respective emission spectra in a solvent were recorded with Perkin Elmer Lambda 35 and Perkin Elmer LS55 spectrophotometers. NMR spectra were recorded on Brucker NEO-1 600 MHz instrument. Single crystals of compound **2** were successfully grown and analyzed by X-Ray diffraction. A suitable single crystal of **2** was mounted on the goniometer of a SuperNova diffractometer using inert Paratone oil and a nylon loop. The collection of diffraction intensities was carried out by CrysAlis PRO software at room temperature using CuKα radiation. The diffractometer is equipped with an X-Ray tube operating at X-ray 50 kV and 0.8 mA and an Eos CCD detector. The crystal structure was solved by the SHELXT [25] solution program via Intrinsic Phasing and further was refined by the least-squares minimization method with the SEHLXL [26] refinement package in Olex2 software [27]. H and O atoms were treated as riding considering an isotropic displacement parameter $U_{iso}(H)=1.2U_{eq}(C)$ for CH [C-H=0.93 Å], $U_{iso}(H)=1.5U_{eq}(C)$ for CH_3 groups [C-H=0.96 Å] and OH groups [O-H=0.82 Å]. The CIF files of 2 have been deposited with the Cambridge Crystallographic Data Centre, having the associated deposition number 2304437. A copy can be obtained free of charge on written application to CCDC, 12 Union Road, Cambridge, CB2 1EZ, UK (Fax: +44-12-2333-6033); on request via e-mail to deposit@ccdc.cam.uk or by access to http://www.ccdc.cam.ac.uk.

Starting material, 10-methyl-10*H*-phenothiazine-3-carbaldehyde **1**, was prepared by Vilsmeier-Haack Formylation with trichlorophosphate in N,N,-dimethyl-formamide and dichloroethane as following the previously reported methods [28].

Experimental procedures for the synthesis of (E)-1-(4-hydroxy-phenyl)-3-(10-methyl-10H-phenothiazin-3-yl)prop-2-en-1-one 2

a) Classical synthesis

In a three-necked flask fitted with a reflux condenser, thermometer and septum were introduced 10-methyl-10*H*-phenothiazine-3-carbaldehyde **1** 0.73g (3.02 mmol) of and a saturated solution of potassium hydroxide in ethanol. The mixture was stirred and heated to 60°C until the raw material **1** was completely dissolved and further it was added 4-hydroxy acetophenone 0.72 g (5.29 mmol). The reaction mixture was stirred for 24 hours at 60°C.

STEFANA GRAMA, BIANCA STOEAN, ALEXANDRU TURZA, DAN PORUMB,
CASTELIA CRISTEA, LUMINITA SILAGHI-DUMITRESCU

After the completion of the reaction, the solvent was partially removed by vacuum distillation. The orange-red precipitate obtained was filtered and recrystallized from 2-propanol and acetonitrile (10:2 v/v), affording 0.36 g product (yield 33%).

b) Mechanochemical synthesis

In a mortar, 10-methyl-10*H*-phenothiazine-3-carbaldehyde **1** (0.73g, 3.02 mmol) and KOH (0.34g, 6 mmol) were added and the mixture was ground with a pestle until a homogeneous mixture was obtained. Over this mixture, 4-hydroxy acetophenone 0.72 g (5.29 mmol) was added in portions, the blend being homogenized after each added portion. After adding the last portion, the mixture was grounded with the pistil for another 30 minutes. The orange paste was recrystallized from 2-propanol and acetonitrile (10:2 v/v), affording 0.22 g pure product (yield of 20%).

c) Ultrasound assisted synthesis

10-methyl-10*H*-phenothiazine-3-carbaldehyde **1** (0.73g, 3.02 mmol), 50 mL of ethanol and KOH (0.34g, 6 mmol) were introduced into a pear-shaped flask. After 10 min of ultrasonating, 4-hydroxy acetophenone 0.72 g (5.29 mmol) was added and the mixture was ultrasonated for another 3 hours in an ultrasonic bath. After the completion of the reaction, small red crystals appeared in the reaction mass. After filtration, 0.51 g pure product (yield 47%) was obtained after recrystallization from 2-propanol.

2 Melting point (from 2-propanol): 185°C

^{1}H-NMR (600 MHz, acetone-d_6) δ (ppm): 8.11(d, 2H, J=8.76 Hz); 7.8(d, 1H, J=15.48 Hz); 7.68(d, 1H, J=7.62 Hz); 7.67(d, 1H, J=15.48 Hz); 7.63(dd, 1H, J=8.34 Hz); 7.24(dd, 1H, J=7.32 Hz); 7.18(dd, 1H, J=2.56 Hz); 7.02(m, 1H); 7.00(m, 1H); 6.99 (m, 1H); 6.97(m, 2H); 3.45(s, 3H).

^{13}C-NMR (150 MHz, acetone-d_6) δ (ppm): 34.5, 114.4, 114.7, 115.2 (2C), 119.0, 122.3, 122.9, 123.5, 126.0, 126.8, 127.8, 129, 130.4, 131.5 (2C), 143.0, 145.0, 147.5, 148.0, 161.2, 187.5.

ACKNOWLEDGMENTS

REFERENCES

1   D. M. Dereje, C. Pontremoli, M. J. Moran Plata, S. Visentin and N. Barbero, *Photochem. Photobiol. Sci.*, **2022**, *21*, 397–419.
2   H. A. Shindy, *Dye. Pigment.*, **2017**, *145*, 505–513.
3   D. Çakir, T. Arslan and Z. Biyiklioglu, *Dalt. Trans.*, **2015**, *44*, 20859–20866.
4   C. F. Lipinski, A. A. Oliveira, K. M. Honorio, P. R. Oliveira and A. B. F. da Silva, *Struct. Chem.*, **2018**, *29*, 957–965.
5   C. Zhuang, W. Zhang, C. Sheng, W. Zhang, C. Xing and Z. Miao, *Chem. Rev.*, **2017**, *117*, 7762–7810.
6   J. C. Trivedi, J. B. Bariwal, K. D. Upadhyay, Y. T. Naliapara, S. K. Joshi, C. C. Pannecouque, E. De Clercq and A. K. Shah, *Tetrahedron Lett.*, **2007**, *48*, 8472–8474.
7   A. L. Cole, S. Hossain, A. M. Cole and O. Phanstiel, *Bioorganic Med. Chem.*, **2016**, *24*, 2768–2776.
8   P. Mahesha, N. S. Shetty and S. D. Kulkarni, *J. Fluoresc.*, **2022**, *32*, 835–862.
9   A. M. Craciun, M. Focsan, L. Gaina and S. Astilean, *Dye. Pigment.*, **2017**, *136*, 24–30.
10 B. Stoean, D. Rugina, M. Focsan, A. M. Craciun, M. Nistor, T. Lovasz, A. Turza, I. D. Porumb, E. Gál, C. Cristea, L. Silaghi-dumitrescu, S. Astilean and L. I. Gaina, *Int. J. Mol. Sci.*, **2021**, *22*, 1–21.
11 A. Pandith, R. G. Siddappa and Y. J. Seo, *J. Photochem. Photobiol. C Photochem. Rev.*, **2019**, *40*, 81–116.
12 B. Stoean, L. Gaina, E. Gal, C. Cristea, T. Lovasz and L. Silaghi-Dumitrescu, *Stud. Univ. Babes-Bolyai Chem.*, **2021**, *66*, 59–66.
13 V. Talianová, T. Bříza, L. Krčová, B. Dolenský, J. Králová, P. Martásek, V. Král and M. Havlík, *Bioorg. Chem.*, **2020**, *94*, 103447.
14 M. M. Corona-López, V. M. Jiménez Pérez, R. Chan-Navarro, M. Ibarra-Rodríguez, H. V. Rasika Dias, A. Chávez-Reyes and B. M. Muñoz-Flores, *J. Organomet. Chem.*, **2017**, *852*, 64–73.
15 F. Di Maria, I. E. Palamà, M. Baroncini, A. Barbieri, A. Bongini, R. Bizzarri, G. Gigli and G. Barbarella, *Org. Biomol. Chem.*, **2014**, *12*, 1603–1610.
16 L. Gaina, T. Lovasz, I.A. Silberg, C. Cristea, S. Udrea, *Het. Commun.*, **2001**, *6*, 549–554.
17 L. Gaina, E. Gal, L. Matarânga-Popa, D. Porumb, A. Nicolescu, C. Cristea, L. Silaghi-Dumitrescu, *Tetrahedron*, **2012**, *68*, 2465–2470.
18 L. Găină, C. Cristea, C. Moldovan, D. Porumb, E. Surducan, C. Deleanu, A. Mahamoud, J. Barbe, I.A. Silberg, *Int. J. Mol. Sci.*, **2007**, *8*, 70–80.
19 L. Gaina, C. Cristea, I.A. Silberg, T. Lovasz, *Rev Roum. Chim*, **2002**, *47*, 983–988.
20 C. A. Lovasz, T, Oltean, G, Toma, AM, Gaina, L, Silaghi-Dumitrescu, L, Jitaru, M, Cristea, C, Sohar P, *Stud. UBB Chem.*, **2007**, *52*, 31–38.
21 L. Gaina, A. Csampai, G. Turos, T. Lovasz, V. Zsoldos-Mady, I.A. Silberg, *Org. Biomol. Chem.*, **2006**, *4*, 4375–4386.

22 E. Gál, C. Cristea, L. Silaghi-Dumitrescu, T. Lovász and A. Csámpai, *Tetrahedron*, **2010**, *66*, 9938–9944.

23 L. Găină, I. Torje, E. Gal, A. Lupan, C. Bischin, R. Silaghi-Dumitrescu, G. Damian, P. Lönnecke, C. Cristea and L. Silaghi-Dumitrescu, *Dye. Pigment.*, **2014**, *102*, 315–325.

24 E. Gal, B. Brem, I. Pereţeanu, L. Găină, T. Lovasz, M. Perde-Schrepler, L. Silaghi-Dumitrescu, C. Cristea and L. Silaghi-Dumitrescu, *Dye. Pigment.*, **2013**, *99*, 144–153.

25 G. M. Sheldrick, *Acta Crystallogr. Sect. A Found. Crystallogr.*, **2015**, *71*, 3–8.

26 G. M. Sheldrick, *Acta Crystallogr. Sect. C Struct. Chem.*, **2015**, *71*, 3–8.

27 O. V. Dolomanov, L. J. Bourhis, R. J. Gildea, J. A. K. Howard and H. Puschmann, *J. Appl. Crystallogr.*, **2009**, *42*, 339–341.

28 E. Molnar, E. Gal, L. Gaina, C. Cristea, E. Fischer-Fodor, M. Perde-Schrepler, P. Achimas-Cadariu, M. Focsan and L. Silaghi-Dumitrescu, *Int. J. Mol. Sci.*, **2020**, *21*, 3178.

SYNTHESIS AND OPTICAL PROPERTIES OF
NOVEL STRONTIUM TETRANITROPHTHALOCYANINE

**Silviu GROZA[a], Bianca STOEAN[a], Adriana GROZAV[b,*],
Ana-Maria CRACIUN[c], Castelia CRISTEA[a],
Luminita SILAGHI-DUMITRESCU[a], Dan PORUMB[a]**

ABSTRACT. Two convenient alternatives for the synthesis of metal(II) 2,9,16,23-tetranitrophthalocyanines (TNPc) were applied in the synthesis of the novel Strontium(II)TNPc and its Zinc(II)TNPc, Copper(II)TNPc and Cobalt(II)TNPc analogues. The thermal activation required for the tetramerization of the phthalic acid derivatives used as substrates (4-nitro-phthalimide or 4-nitrophthalodinitrile) was provided by convective heating in solution or solvent free conditions. The optical properties of the synthesized metal(II)TNPc were compared by means of UV-vis spectroscopy. In solution, the novel Sr(II)TNPc was characterized by absorption bands with maxima situated around 690 nm (similar to Cu(II)TNPc), while its fluorescence emission maxima lays close to Zn(II)TNPc (710 nm), with a three times longer fluorescence emission life time in solid state (3.04 ns).

Keywords: phthalocyanine; strontium-complex; UV-vis spectroscopy; fluorescence emission life time

---

[a] *Faculty of Chemistry and Chemical Engineering, Babeş-Bolyai University, 11 Arany Janos str., RO-400028, Cluj-Napoca, Romania*
[b] *Department of Organic Chemistry, "Iuliu Hatieganu" University of Medicine and Pharmacy, 41 Victor Babes, Street, 400012 Cluj-Napoca, Romania*
[c] *Nanobiophotonics and Laser Microspectroscopy Center, Interdisciplinary Research Institute in Bio-Nano-Sciences, Babes-Bolyai University, 42 Treboniu Laurian Street, 400271 Cluj-Napoca, Romania*
[*] *Corresponding author: adriana.ignat@umfcluj.ro*

SILVIU GROZA, BIANCA STOEAN, ADRIANA GROZAV, ANA-MARIA CRACIUN,
CASTELIA CRISTEA, LUMINITA SILAGHI-DUMITRESCU, DAN PORUMB

INTRODUCTION

Phthalocyanine (**Pc**) is a macrocyclic compound belonging to the class of aza[18]anulenes which was discovered at the beginning of the 20th century. The macrocyclic structure of **Pc** embodies four isoindole ([3,4]benzopyrrole) moieties connected by imine bridges (-N=) enabling a continuous conjugated system of 18 π-electrons complying with the aromaticity Huckel's rule [1]. Functionalization of **Pc** imply peripheral substitution, core metalation and axial substitution. Various metallophthalocyanines (**MPc**) containing a metal ion coordinated in the central cavity of the macrocyclic dianion ligand were reported with the aim of tuning the **Pc**s' chemical and dyeing properties. The properties of **Pc** derivatives were subsequently investigated leading to their use as pigments and dyes in various inks, paints and varnishes formulations due to their exceptional thermal stability and resilience to the action of acids and bases [2]. **Pc** derivatives exhibit high values of molar extinction coefficients for the main absorption bands situated in visible and near-infrared spectra.

Currently, **Pc** derivatives are utilized in industrial sectors, such as dyes industry, molecular electronics, and solar cells, due to their distinctive characteristics [3]. Recently, there has been a significant interest in the study of **Pc** and **MPc** derivatives containing core substitution with transition metals. This is due to their exceptional features, which make them very promising for modern growing sectors including liquid crystals, catalysts, and photochromic materials [4]. **Pc** derivatives have also found application in medicinal preclinical investigations due to their biological activity, potential usage as photosensitizers in photodynamic therapy and ability to provide fluorescence imaging of tumour tissues [5-7]. Nanomedicine has come a long way in the past few years, especially when it comes to synthesize multifunctional theragnostic drugs that can be used for specific cancer imaging and treatment. Two new ways to obtain protein-based (anti-folate receptor anti-body) nanoparticles that encapsulate (Zn(II)-2,9,16,23-tetranitrophthalocyanine for specific fluorescence imaging and dual treatment of ovarian cancer have been reported [8]. Further, nanoparticles made of bovine serum albumin that are loaded with (Zn(II)-2,9,16,23-tetraaminphthalocyanine showed great biocompatibility and efficient photothermal conversion, suggesting a potential for biomedical applications [9]. **MPc** derivatives are redox active compounds which were exploited in the preparation of modified gold electrodes for electrocatalytic oxidation and detection of different analytes. Unlike redox active phenothiazine derivatives mediators which strongly adsorb directly on gold electrodes (based on the the presence of the sulphur atom in the structure of the heterocycle) [10], self-assembled monolayer films of Fe(II)Pc were axially ligated to mercaptopyridine modified gold electrodes [11].

Pc derivatives can be synthesized by the cyclization of precursors based on an array of phthalic acid derivatives (anhydride, imide, diamide, dinitrile) [12,13] and metal salts containing the metal ion as template for the cyclotetramerization which proceeds in a melt or in a high boiling solvent (Scheme 1).
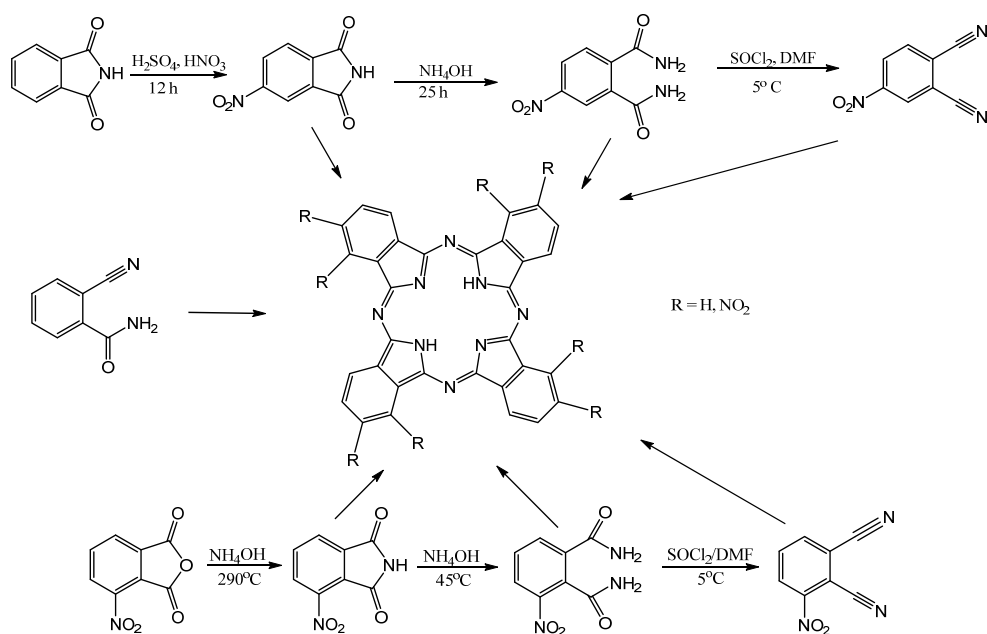
Scheme 1. Synthesis of **Pc**s from phthalic acid derivatives

Many **MPc** derivatives were synthesized using a wide array of metal salts. Free phthalocyanines (**H$_2$-Pc**) can be obtained directly by the macrocyclization of the above mentioned precursors or by reducing a **MPc** in pyridine and hydrochloric acid [14]. The majority of **Pc** exhibit limited solubility in various solvents, such as water, bases, and acids. However, they do exhibit solubility in dimethylsulfoxide (DMSO) and concentrated sulfuric acid (H$_2$SO$_4$). In order to enhance their applicability in photodynamic therapy and other bio-medical fields, there are currently explored new analogues of phthalocyanines that contain hydroxyl, carboxyl, amino or sulfonyl groups, which significantly enhance their solubility in water [15].

In this work are presented two alternative synthetic routes validated in the preparation of four **MPc** derivatives branded by the macrocycle peripheral substitution with nitro auxochromic groups and core metalation with the divalent

cations: strontium(II), copper(II), cobalt(II) and zinc(II) respectively. The electronic properties of the novel Sr(II)**MPc** are compared with the Cu(II), Co(II) and Zn(II) **MPc** analogues based on the recorded UV-vis spectroscopic data.

RESULTS AND DISCUSSION

The target metallocomplexes of 2,9,16,23–tetranitro-phthalocyanine (**TNPc***)* were successfully obtained by two synthetic pathways as presented in Scheme 2.
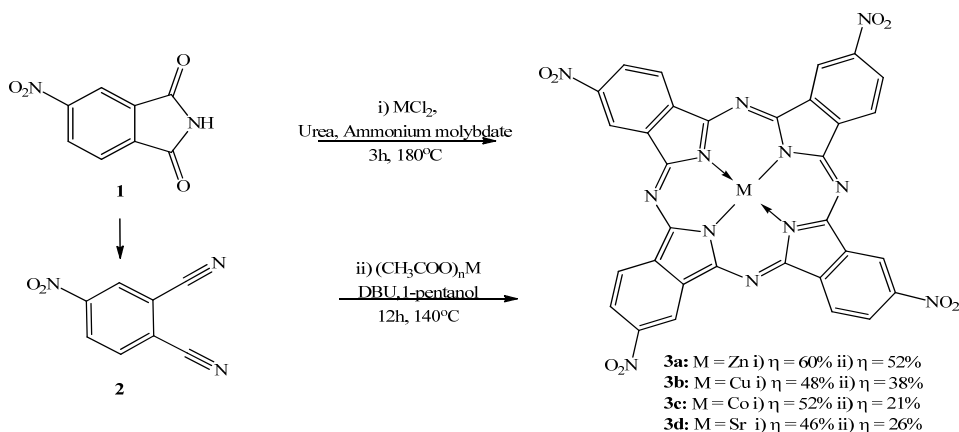
Scheme 2. Alternative syntheses of metal(II)**TNPc**

The first approach for the synthesis of Zn(II)TNPc **3a,** Cu(II)TNPc **3b,** Co(II)TNPc **3c** and Sr(II)TNPc **3d** respectively, involves a solvent-free method utilizing 4-nitro-phthalimide **1** as the starting material, urea as a source of nitrogen, ammonium molybdate catalyst and the metal chloride template.

The second method employs 4-nitro-phthalodinitrile **2** substrate dissolved in a high boiling point solvent, specifically 1-pentanol, along with the non-nucleophilic hindered base1,8-diazabicyclo(5.4.0)undec-7-ene (DBU) and the metal acetate template. Given that 4-nitro-phthalodinitrile **2** is the starting material in this process, the presence of an additional nitrogen source was no longer necessary.

As it may be seen from Scheme 1, 4-nitro-phthalodinitrile **2** can be obtained from 4-nitro-phthalimide **1** in two additional reaction steps (ammonolysis followed by dehydration of the 4-nitro-phthalamide intermediate) and thus, overall reaction yields of metal(II)**TNPc** are not higher. While the solvent-free approach offers benefits such as increased yields and reduced expenses,

there is a potential issue related to the convective heating ensuring an uneven distribution of the temperature within the reaction mixture. Consequently, when temperature rise above 180°C, a potential risk of partial carbonization of the reaction mixture may occur.

A comparative study of the optical properties displayed by the synthesized metal(II)**TNPc 3a-d** was performed. Table 1 provide the typical visible absorption and fluorescence emission data recorded by UV-vis spectroscopy in dimethylsulfoxide (DMSO) solution. As it may be seen in Figure 1a showing the overlaid visible absorption spectra of metal(II)**TNPc 3a-d,** a slight bathochrome shift was recorded for the novel Sr(II)TNPc **3d**, while Co(II)TNPc **3c** exhibited an apparent hyperchromic effect. While the absorption characteristics of Sr(II)TNPc **3d** are similar to that of Cu(II)TNPc **3a**, its fluorescence emission maxima is situated in the near-infrared region similar to Zn(II)TNPc **3a** (Figure 1b). Co(II)TNPc **3c** was characterized by the greatest Stokes shift value (645 cm^{-1}).
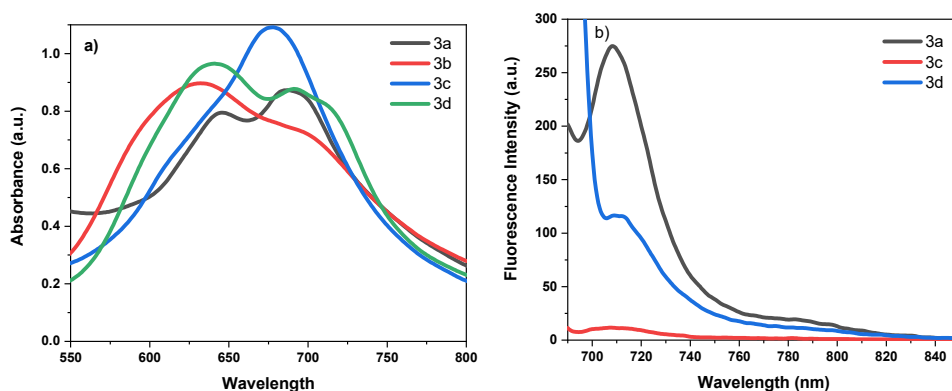
Figure 1. UV-vis spectra of metal(II)TNPc **3a-d** in DMSO solution: a) absorption spectra (C$_M$=4x10^{-5}M), b) fluorescence emission spectra (C$_M$=4x10^{-8}M).

Table 1. UV-vis absorption/emission wavelength maxima, molar extinction coefficients, Stokes shifts and fluorescence lifetime of metal(II)**TNPc 3a-d** in DMSO solutions.

Cpd.	λ_{abs} (nm)	ε (cm^{-1}M^{-1})	λ_{em} (nm)	Stokes Shift (cm^{-1})	Fluorescence lifetime (ns)
3a	687	16578	708	432	0.9
3b	690	18500	-	-	-
3c	678	27288	709	645	0.8
3d	691	21935	710	387	3.04
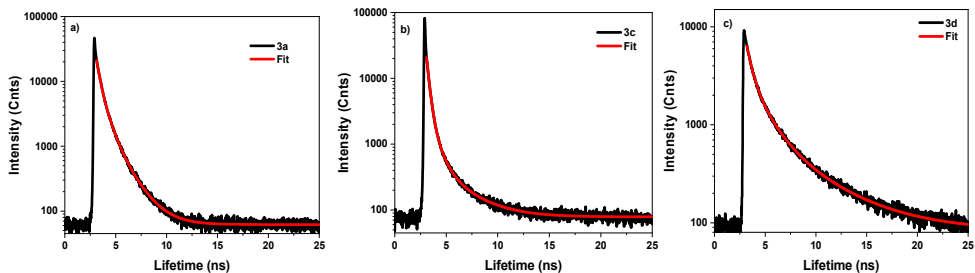
Figure 2. Fluorescent lifetime histograms for metal(II)TNPc **3a** – a), **3c** – b), **3d** – c).

Additionally, when comparing the fluorescence lifetimes determined by time-resolved confocal fluorescence microscopy for **3a**, **3c**, **3d** in solid state, Sr(II)TNPc **3d** exhibited a fluorescence lifetime that is three times longer than its Zn(II)TNPc **3a** and Co(II)TNPc **3c** analogues. The variations in fluorescence lifetimes are most likely due to the modifications in electronic structure, non-radiative decay pathways, and energy transfer processes induced by the metal ions.

The aggregation of **Pc** chromophore system may impede its efficacy in various applications by influencing its photophysical properties (such as fluorescence quenching) or photochemical properties (such as singlet oxygen generation or loss of catalytic activity). A first attempt to detect the aggregation tendency of metal(II)TNPc **3a-d** is presented below.
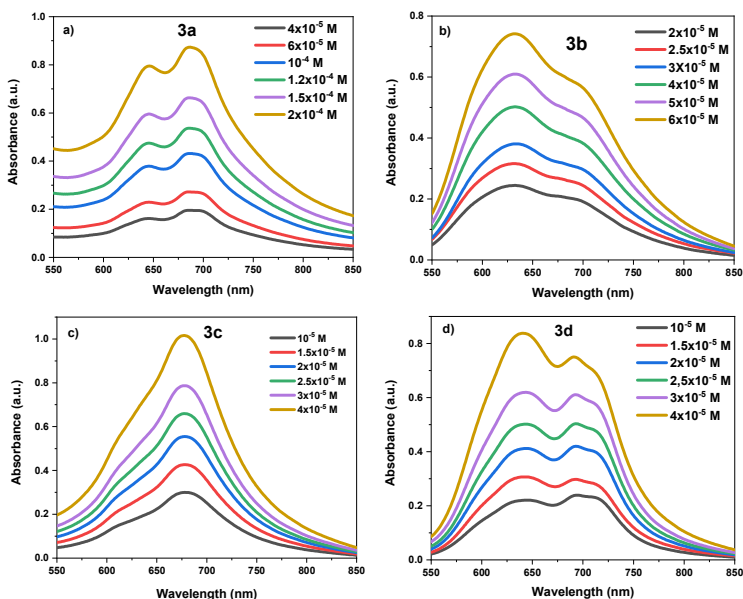
Figure 3. UV-vis spectra of metal(II)TNPc **3a-d** in DMSO at different concentration ranges.

Absorption spectra of metal(II)TNPc **3a-d** were recorded in DMSO solution at various concentrations ranging between 10^{-4} and 10^{-6}M. As it may be seen from the overlaid absorption spectra presented in Figure 3 for each metal(II)TNPc **3a-d** the Lambert-Beer law is followed, with absorbance increasing in proportion to the concentration of the compound in solution, suggesting that the aggregation does not occur in the aprotic dipolar DMSO solvent at concentrations ranging between 10^{-4} and 10^{-5}M.

CONCLUSIONS

This work described two convenient approaches for the synthesis of metal(II)TNPc validated in the synthesis of Zn(II)TNPc **3a**, Cu(II)TNPc **3b** and Co(II)TNPc **3c** and the novel Sr(II)TNPc **3d**. The thermal activation required for the tetramerization of the phthalic acid derivatives used as substrate (4-nitro-phthalimide / 4-nitrophthalodinitrile) was provided by convective heating in solvent-free / in solution conditions. Although the solvent-free strategy may provide issues in temperature distribution, the study highlights its advantages in terms of increased yield, reduced costs and the possibility of avoiding the hazards induced by the use of volatile organic compounds (VOC).

In terms of optical properties, the novel Sr(II)TNPc **3d** displayed the strong visible absorption maxima and fluorescence emission maxima in both solution and solid state, with fluorescence lifetime of 3.04 ns, having the potential to become a valuable candidate as fluorophore in tissue bioimaging using fluorescence microscopy, as well as photosensitizer in photodynamic therapy.

EXPERIMENTAL SECTION

Unless otherwise specified, all experimental materials, reagents, and solvents were procured from commercial suppliers and utilized without additional purification. Mass spectra were recorded using Bruker Rapiflex MALDI-TOF apparatus from Bruker Daltonics (Bremen, Germany), equipped with a Smartbeam 3D laser. The UV-Vis absorption and fluorescence emission spectra were recorded using the Perkin Elmer Lambda 35 and Perkin Elmer LS55 spectrophotometers.

The synthesis of the starting 4-nitrophthalimide **1** was achieved according to literature data by subjecting phthalimide to nitration using a concentrated solution of sulfuric acid and nitric acid at room temperature [13].

The synthesis of the starting 4-nitrophthalodinitrile **2** was performed according to literature data by ammonolysis of 4-nitrophthalimide to 4-nitrophthalamide using ammonium hydroxide solution, followed by dehydration using thionyl chloride at low temperature [13].

Fluorescence emission life time was recorded from solid-state samples deposited on glass slides with a time-resolved confocal fluorescence microscopy system (MicroTime 200, PicoQuant, Germany) equipped with an Olympus IX71 microscope. Samples were excited with a pulsed laser diode at 640 nm (LDH-D 640 nm, 40 MHz). The signal was collected using a UPLSAPO 60×/NA=1.2 water immersion objective, and a BLP01-647R emission filter (Semrock) was used to filter the signal. The mean values of the fluorescence lifetimes of the samples were obtained by fitting operations on the experimental curves with exponential equations.

Experimental procedures for the synthesis of zinc(II), copper(II), cobalt(II) and strontium(II) 2,9,16,23–tetranitro-phthalocyanines

a) Solvent-free procedure

A mixture containing 4 mmol of metal chloride (copper(II) chloride, zinc(II) chloride, cobalt(II) chloride and respectively strontium(II) chloride), 12.5 g (0.208 mol) of urea, 2.33 g (12 mmol) of 4-nitrophthalimide, and 0.015 g (0.013 mmol) of ammonium molybdate was thoroughly grounded in an agate mortar. The mixture was then transferred into a 100 mL round bottom flask equipped with an air condenser. The mixture was occasionally stirred with a glass rod while being heated on a sand bath at 180°C for 3 hours. After the completion of the reaction, the crude black product was refluxed for 30 minutes in 50 mL of 1M hydrochloric acid solution. Subsequently, the black product was filtered and rinsed with distilled water until reaching a neutral pH. Further, the precipitate was refluxed with a 1M NaOH solution, followed by filtration and thorough washing with ample amounts of distilled water. The acid-base treatment was reiterated thrice. The precipitate was further purified by refluxing in a 1:1 (v/v) mixture of acetone and acetonitrile for one hour. After that, the mixture was filtered and the resulting solid was washed with distilled water. The product was subjected to a final purification step by refluxing it in a mixture of tetrahydrofuran and chloroform 1:6 (v/v) for one hour. After hot filtration, it resulted the formation of a blue or green-metallic precipitate (1.36g, 60% yield for $C_{32}H_{12}N_{12}O_8Zn$ (**3a**), 1.09g, 48% yield for $C_{32}H_{12}N_{12}O_8Cu$ (**3b**), 1.17g, 52% yield for $C_{32}H_{12}N_{12}O_8Co$ (**3c**), 1.08g, 46% yield for $C_{32}H_{12}N_{12}O_8Sr$ (**3d**)).

b) Procedure in 1-pentanol

In a 100 mL round flask with three necks, fitted with a reflux condenser, a thermometer, and an argon source to maintain the reaction in an inert atmosphere, 0.95 g (5.5 mmol) of 4-nitrophthalodinitrile, 20 mL of 1-pentanol, and 1.4 mmol of metal acetate (copper(II)acetate, zinc(II) acetate, strontium(II)

acetate, cobalt(II) acetate) and 0.5 mL (3.34 mmol) of DBU were added. The reaction mixture was heated at 140°C for 24 hours in an oil bath upon stirring under an inert atmosphere. After the completion of the reaction, the solvent was distilled, and the crude product underwent the identical purification steps outlined above in the solvent-free synthesis (0.54g, 52% yield for $C_{32}H_{12}N_{12}O_8Zn$ (**3a**), 0.40g, 38% yield for $C_{32}H_{12}N_{12}O_8Cu$ (**3b**), 0.22g, 21% yield for $C_{32}H_{12}N_{12}O_8Co$ (**3c**), 0.28g, 26% yield for $C_{32}H_{12}N_{12}O_8Sr$ (**3d**)).

MS (MALDI-TOF/TOF) m/z: 757.900 calcd. for $C_{32}H_{12}N_{12}O_8Zn$, found: 757.918; 756.060 calcd. for $C_{32}H_{12}N_{12}O_8Cu$ found: 755.540; 751.450 calcd. for $C_{32}H_{12}N_{12}O_8Co$ found: 751.421; 779.996 calcd. for $C_{32}H_{12}N_{12}O_8Sr$ found: 778.196.

ACKNOWLEDGMENTS

REFERENCES

1   A. Gök, E. B. Orman, Ü. Salan, A. R. Özkaya and M. Bulut, *Dye. Pigment.*, **2016**, *133*, 311–323.
2   R. A. S. Ali, J. Keshavayya, A. S. Jagadisha, S. D. Umesha, K. N. Gujjar, S. A. Narasimha, D. G. Prasanna and E. Nagaraja, *Mater. Today Proc.*, **2021**, *49*, 644–649.
3   M. Pişkin, *J. Photochem. Photobiol. A Chem.*, **2023**, *435*, 114325.
4   Y. Baygu, N. Kabay, B. Kabay, B. Yıldız, İ. Ömeroğlu, M. Durmuş, E. Rıza Karagür, H. Akça, Ç. Ergin and Y. Gök, *J. Mol. Struct.*, **2023**, *1271*, 134010.
5   H. M. Almuzafar, H. M. Ahmed, N. N. AlDuhaisan, A. M. Elsharif, H. Aldossary, S. Rehman, S. Akhtar and F. A. Khan, *J. Saudi Chem. Soc.*, **2022**, *26*, 101436.
6   R. A. Barmin, E. A. Maksimova, P. G. Rudakovskaya, A. V. Gayer, E. A. Shirshin, K. S. Petrov, D. A. Terentyeva, O. I. Gusliakova, O. A. Sindeeva, O. A. Klimenko, R. N. Chuprov-Netochin, A. A. Solovev, G. Huang, A. V. Ryabova, V. B. Loschenov and D. A. Gorin, *Colloids Surf. B.*, **2022**, *219*, 112856.
7   G. Gümrükçü Köse and G. Keser Karaoğlan, *Chem. Phys.*, **2023**, *565*, 111737.
8   R. Borlan, M. Focsan, M. Perde-Schrepler, O. Soritau, A. Campu, L. Gaina, E. Pall, B. Pop, O. Baldasici, C. Gherman, D. Stoia, D. Maniu and S. Astilean, *Biomater. Sci.*, **2021**, *9*, 6183–6202.
9   R. Borlan, D. Stoia, L. Gaina, A. Campu, G. Marc, M. Perde-Schrepler, M. Silion, D. Maniu, M. Focsan and S. Astilean, *Molecules*, **2021**, *26*, 1–21.
10 V. Rosca, L. Muresan, I. C. Popescu, C. Cristea and I. A. Silberg, *Electrochem. commun.*, **2001**, *3*, 439–445.
11 K. I. Ozoemena and T. Nyokong, *Talanta*, **2005**, *67*, 162–168.

12 J. T. Engle, A. N. Allison, J. M. Standard, I. S. Tamgho and C. J. Ziegler, *J. Porphyr. Phthalocyanines*, **2013**, *17*, 712–721.
13 B. I. Kharisov, U. Ortiz Mendez, J. L. Almaraz Garza and J. R. Almaguer Rodriguez, *New J. Chem.*, **2005**, *29*, 686–692.
14 J. Alzeer, P. J. C. Roth and N. W. Luedtke, *Chem. Commun.*, **2009**, 1970–1971.
15 C. G. Claessens, U. Hahn and T. Torres, *Chem. Rec.*, **2008**, *8*, 75–97.

SYNTHESYS AND CHARACTERIZATION OF SILVER-DOPED HYDROXYAPATITE

**Regina PETKES[a], Noémi-Izabella FARKAS[a],
Laura MARINCAȘ[a], Judith-Hajnal BARTHA-VARI[a],
Réka BARABÁS[a,*]**

ABSTRACT. Different preparation methods of Ag-doped hydroxyapatite were compared and an efficient solid-state reaction-based method was developed for the synthesis of silver doped-hydroxyapatite using $AgNO_3$ as silver source. The obtained nanomaterial was characterized by SEM, EDS and XRD measurements. By this method 10% silver was detected in the structure of the hydroxyapatite**.**

Keywords: hydroxyapatite, silver, silver-doped hydroxyapatite, wet precipitation method, solid state method

INTRODUCTION

The globally increasing antibiotic-resistant infections drove the interest toward developing alternative bactericidal materials [1].

Silver is a highly effective natural antibacterial agent that can interact with a wide range of organisms such as viruses [2], bacteria [3] and fungi [4]. It has excellent biocompatibility, satisfactory stability and low toxicity to mammalian cells [5]. Due to these properties, silver nanoparticles appear in surgical instruments, medical catheters, antimicrobial dressings [6], but it can also be observed in many consumer articles such as cosmetics [7], detergents

a   *Babeş-Bolyai University, Faculty of Chemistry and Chemical Engineering, Department of Chemistry and Chemical Engineering, Hungarian Line of Study 11 Arany Janos str., RO-400028, Cluj-Napoca, Romania*
*   *Corresponding author: reka.barabas@ubbcluj.ro*

[8], air and water filters [9], and various textiles. In the past years during the pandemic silver's antiviral property was intense studied and found to be affective against SARS-CoV-2 [10], [11], [12].

Hydroxyapatite (HAP) is a calcium phosphate similar to human bone and teeth [13]. It has outstanding properties such as bioactivity, biocompatibility, osteoconductivity and affinity to biopolymers [14]. Hydroxyapatite is also nontoxic and has a non-inflammatory [15] non-allergenic, non-mutagenic nature [16]. Due to these unique properties, hydroxyapatite has got a variety of applications as biomedical material. It has been successfully applied in orthopedics, dentistry, ophthalmology, traumatology and maxillofacial surgery [17], but it is also used in medical devices [18] or in drug delivery systems [19]. The synthesis of HAP can be achieved by dry, wet and high temperature methods. The size, morphology and crystalline phase of the calcium phosphate will be different in case of the used synthesis method, which will affect the hydroxyapatite's properties [20]. It is important for hydroxyapatite-based nanomaterials used as implants to possess antibacterial properties; thus, the synthesis of silver doped nanomaterials is gaining more and more interest. The treatment duration can be reduced by the antibacterial effect, the efficacy of the implant can be thus improved. Silver can be incorporated in biomaterials including hydroxyapatite in its many oxidation states [21].

Among the most used processes the simple wet precipitation method is which, facilitates the incorporation of silver into the apatite structure. Although this method has advantages on industrial scale [22] the presence of potential impurities due to various ions manifested in aqueous solution can be a drawback.

Several wet methods were implied for doping hydroxyapatite with silver. Ciobanu et al. [23] used the coprecipitation method for synthesizing silver-doped hydroxyapatite. They studied its antimicrobial and antibacterial activity against fungi and bacteria. The same approach was used by Lim et al. [24] for the synthesis of silver decorated HAP. A low temperature ion-exchange technique was also used for the preparation of nano silver loaded hydroxyapatite [25]. Plasma spraying method was also used for doping hydroxyapatite with silver oxide [26]. Vukomanovic et al. [27] developed a sonochemical method for the growth of silver nanoparticles in combination with hydroxyapatite to form composites. Sol-gel approaches were used for doping hydroxyapatite with silver, Chen et al. evaluated the antibacterial property of Ag containing hydroxyapatite film on titanium surfaces obtained by this method [28].

Ag-doped hydroxyapatite was also prepared using microwave assisted synthesis [29], or ion beam-assisted deposition.

Based on our previous successful incorporation of doxycycline in HAP structure [30] in order to further enhance the antibacterial property of hydroxyapatite, the aim of the present study is the incorporation of silver in the structure of HAP using different methods and to compare the effectiveness of these methods.

RESULTS AND DISCUSSION

The aim of the study was a critical comparison of different methods for the synthesis of silver doped hydroxyapatite and the characterization of the obtained product.

In recent years, a variety of methods have been used for the synthesis of silver doped hydroxyapatite, such as hydrothermal, sol-gel, mechanochemical, ultrasonic and combustion processing. In all our attempts hydroxyapatite was prepared by *wet precipitation* method, a process efficiently controlled. Hydroxyapatite was prepared using $Ca(NO_3)_2$ and $(NH_4)_2HPO_4$. The calcium nitrate to diammonium phosphate ratio (Ca/P) was 1.67. During the preparation process the pH of the solution was maintained at 11 and for doping with Ag, different methods were used. Table 1 contains the obtained products and their naming.

Table 1. Methods used for the synthesis of silver-doped hydroxyapatite and the naming of the obtained products

NR.	METHOD	SILVER SOURCE	LABELING	
			Calcined	Non-calcined
1	Wet precipitation	Colloidal silver	*C-Ag-HAP-cal*	*C-Ag-HAP*
2	Wet precipitation	$AgNo_3$	Ag-HAP-cal	Ag-HAP
3	Wet precipitation	Silver complex	*Co-Ag-HAP-cal600* *Co-Ag-HAP-cal800*	*Co-Ag-HAP-noncal*
4	Solid state	$AgNO_3$	-	*Sp-Ag-HAP*

1. In our *first attempt* colloidal silver was used as silver source, which was obtained from $AgNO_3$ solution and $NaBH_4$. The silver colloid was added to the hydroxyapatite solution and the reaction mixture was stirred continuously for 24 hours at room temperature. The silver doped HAP nanoparticles were dried at 200°C and half of the sample was calcined at 1000°C. The obtained nanoparticles were characterized by different physical-chemical methods. The morphology, particle size and chemical elemental composition of silver-doped HAP were observed by scanning electron microscopy coupled with

energy-dispersive X-ray diffraction (SEM/EDS). XRD measurements were also used for the analysis of the materials.The XRD spectra of the obtained nanomaterial is shown in **Figure 1**. For the non- calcined material (*C-Ag-HAP*) as well for the sintered *(C-Ag-HAP-cal)* the spectra shows the signal for hydroxyapatite and for the $Ca(NO_3)_2$,, but the signal for the silver cannot be observed.
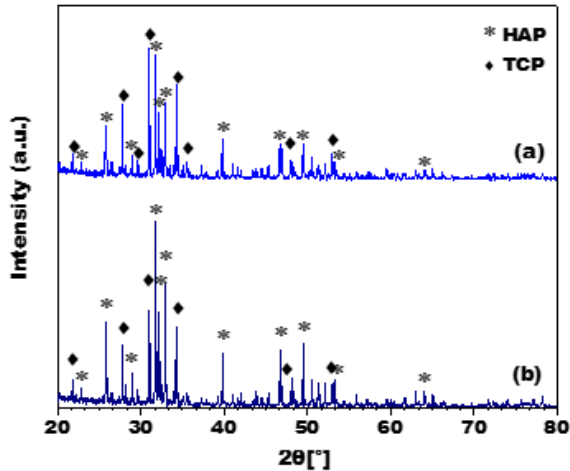
Figure 1. XRD diffractograms of (a) *C-Ag-HAP* and (b) *C-Ag-HAP-cal*

EDS measurements were also performed for both obtained samples (**Figure 2** and **Figure 3**): Large amounts of carbon, phosphorus and oxygen can be seen, but there the silver is not present in the samples.
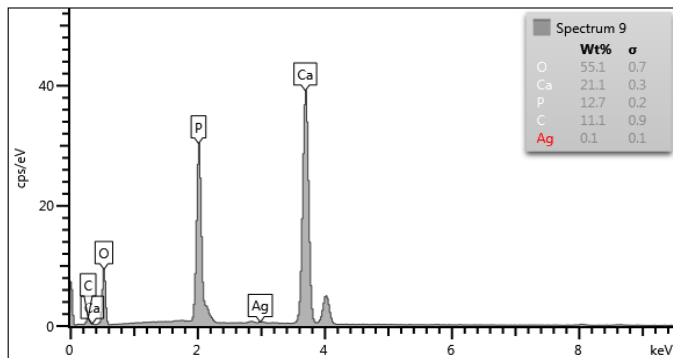
Figure 2. EDS measurements for the *C-Ag-HAP*
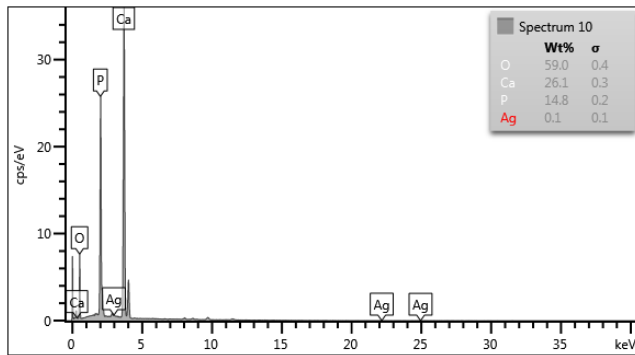
Figure 3. EDS measurements for the *C-Ag-HAP-cal*

2. In our *next attempt* for obtaining silver doped hydroxyapatite AgNo$_3$ was used as silver source. The solution of AgNO$_3$ was added to the solution of calcium nitrate tetrahydrate. To the resulting solution, the diammonium hydrogen phosphate solution was added using a peristaltic pump. The pH of the solution was adjusted to 11 and stirred continuously for 24 hours at room temperature. After the reaction time, the mixture was filtered under vacuum, washed with deionized water, dried at 200°C, and half of the sample was calcined at 1000°C (Ag-HAP and Ag-HAP-sint). These materials were also tested with XRD, but the results only show the signals for the hydroxyapatite both for the non-calcined and calcined materials (**Figure 4**).
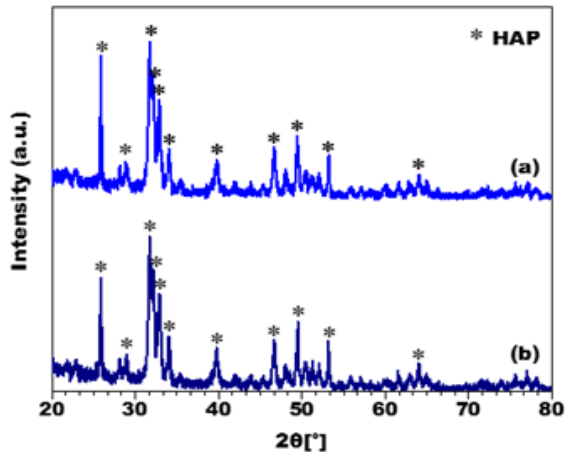
Figure 4. XRD diffractograms of (a) Ag-HAP and (b) Ag-HAP-cal

EDS analysis was also performed, but the silver could not be detected (**Figure 5 and 6**).
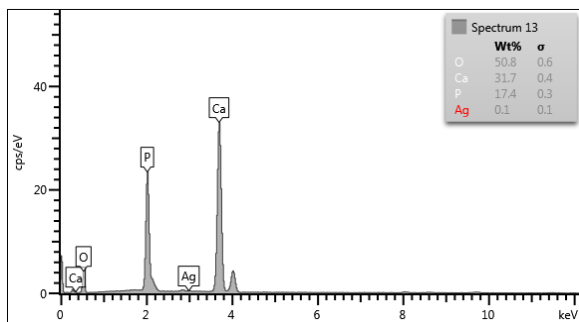
Figure 5. EDS spectra of Ag-HAP
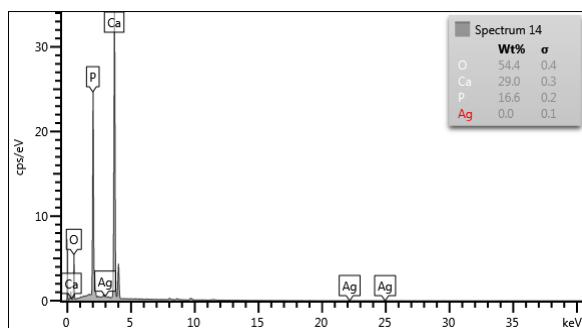
Figure 6. EDS spectra of Ag-HAP-cal

3. Further a diamine-silver hydroxide complex was used as silver source in order to incorporate the silver in the structure of the hydroxyapatite. For the preparation of the complex $AgNO_3$ solution was prepared and then ammonia solution was added until the silver oxide precipitated. The solution was centrifuged, the liquid phase removed, and the silver oxide was redissolved in 25 % ammonia solution (**Scheme 1**).

$$2AgNO_3 + 2NH_3 \cdot H_2O \rightarrow Ag_2O + 2NH_4NO_3$$
$$Ag_2O + 4NH_3 \cdot H_2O \rightarrow 2\left[Ag(NH_3)_2\right]OH$$
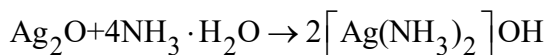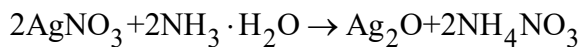
Scheme 1. Preparation of the silver complex

The solution of the formed complex was mixed with the solution of the hydroxyapatite. The pH of the reaction mixture was adjusted to 11 with ammonia solution, stirred continuously for 24 hours at room temperature, filtered, washed, dried and the resulting sample was then divided into three parts. The first sample was not calcined (*Co-Ag-HAP-noncal*), while the second and third samples were calcined at 600°C for 1 hour *(Co-Ag-HAP-*sint600*)*. Afterwards, the third sample was calcined at 800°C for another 1 hour (Co-Ag-HAP-sint800*)*. XRD spectra show no evidence of silver in the samples (**Figure 7**).
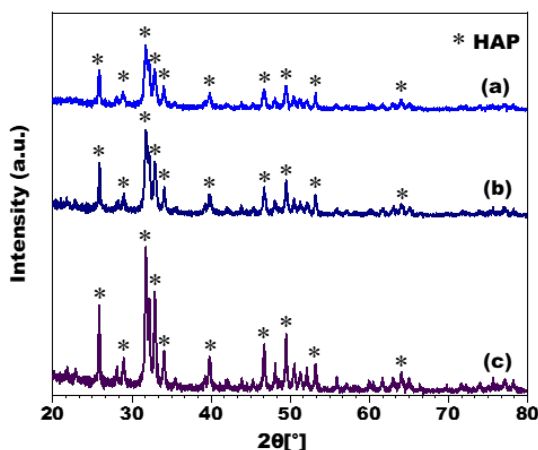
Figure 7. XRD diffractograms of (a) *Co-Ag-HAP-noncal*, (b) *Co-Ag-HAP-cal600*, and (c) *Co-Ag-HAP-cal800*

EDS measurements are in accordance with the XRD spectra, the amount of silver cannot be detected on the synthesized nanomaterials (**Figure 8, 9, 10**).
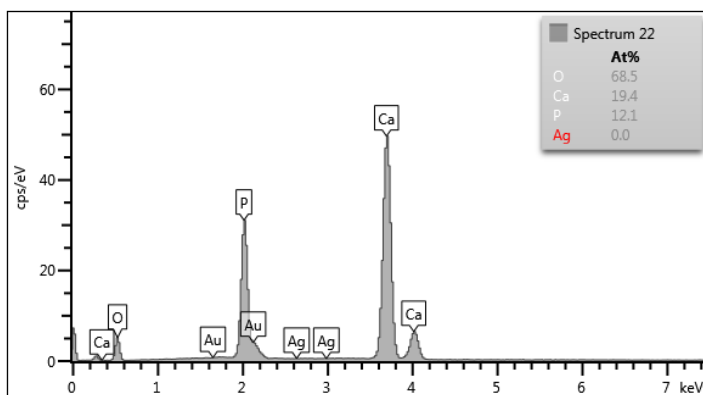
Figure 8. EDS spectra of *Co-Ag-HAP-noncal*
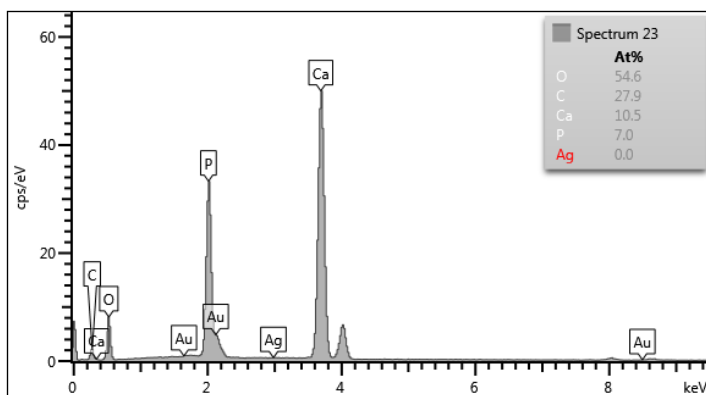
Figure 9. EDS spectra of *Co-Ag-HAP- cal600*
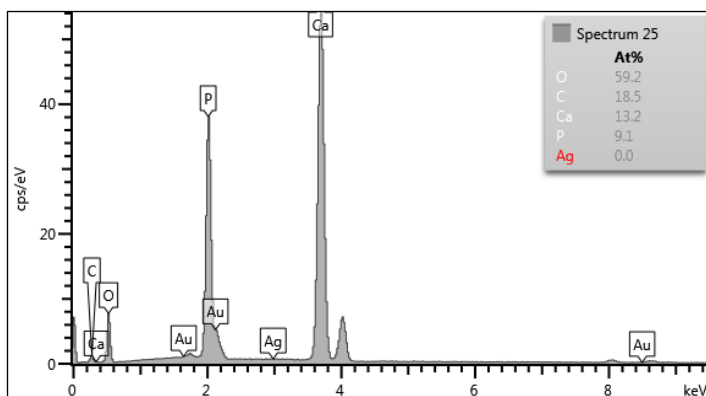
Figure 10. EDS spectra of *Co-Ag-HAP- cal800*

Although there are several examples in the literature which report the successful incorporation of silver into the hydroxyapatite's structure with the above described methods, we could not reproduce their results. According to Rajendran **et al**. silver cannot be incorporated into the hydroxyapatite's structure at pH 11 [31]. The article reports that systematic studies have been carried out to understand the effect of pH on silver precipitation in Ag-HAP nanomaterials. They concluded that silver can only precipitate on HAP if the pH of the mixing solution is 9 or below, but stable and pure HAP can only be synthesized at pH above 9.

4. Therefore, the *solid-state method* was tested for the preparation of silver doped hydroxyapatite.

Pure apatite was synthesized as earlier described. $AgNO_3$ was used as silver source which was added to the hydroxyapatite powder. The resulting mixture was calcined at 500°C for 1 hour and then 800 °C for 1 hour (Sp-Ag-HAP). After calcination, the previously white sample turned brown. Using this method, on the XRD spectra also the silvers' signal is visible (**Figure 11**). The EDS analysis revealed 10% silver in the hydroxyapatite structure (**Figure 12**).
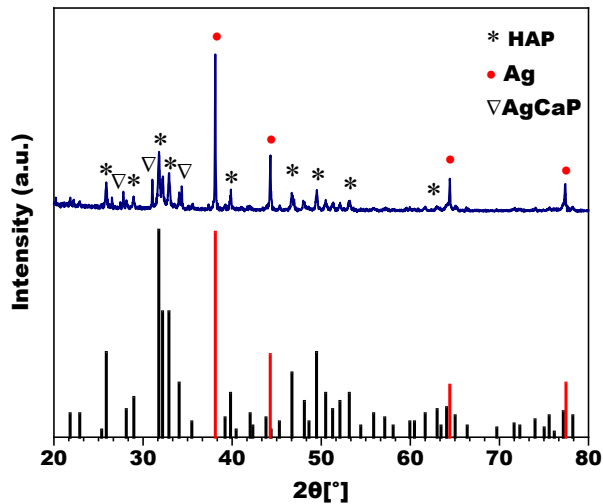
Figure 11. XRD diffractograms of Sp-Ag-HAP
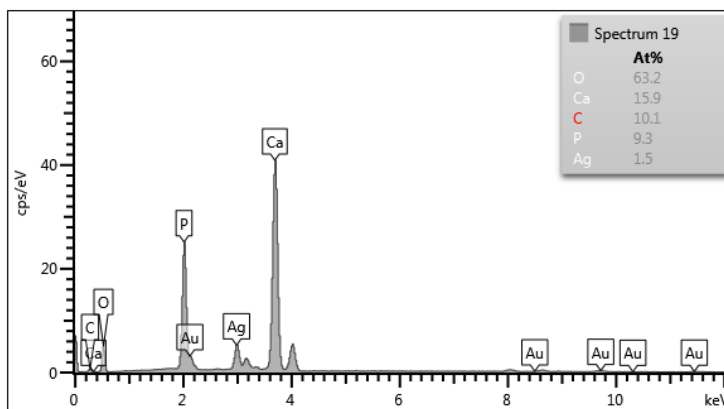
Figure 12. EDS spectra of *Sp-Ag-HAP*

The surface and the morphology of the obtained nanoparticles were also investigated with scanning electron microscopy (**Figure 13**). From the obtained images the Ag-hydroxyapatite granules and their rounded shape can be observed which were obtained by the sintering process.
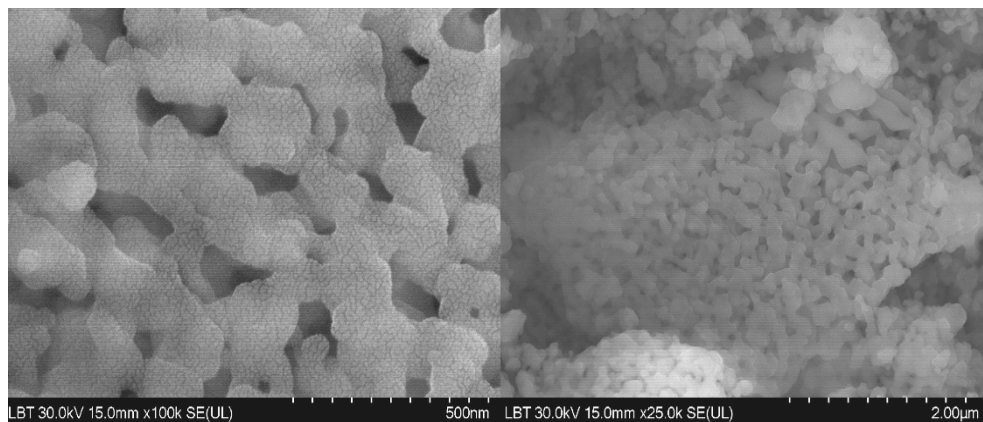
Figure 13. SEM images of the Sp-Ag-HAP nanoparticles

The EDS layered images are in accordance with the previously described observations, on the spectra of C-Ag-HAP (which was chosen as representative for the unsuccessful reactions), no silver can be observed, while the spectra of Sp-Ag-HAP reveal also the presence of silver (**Figure 14**).
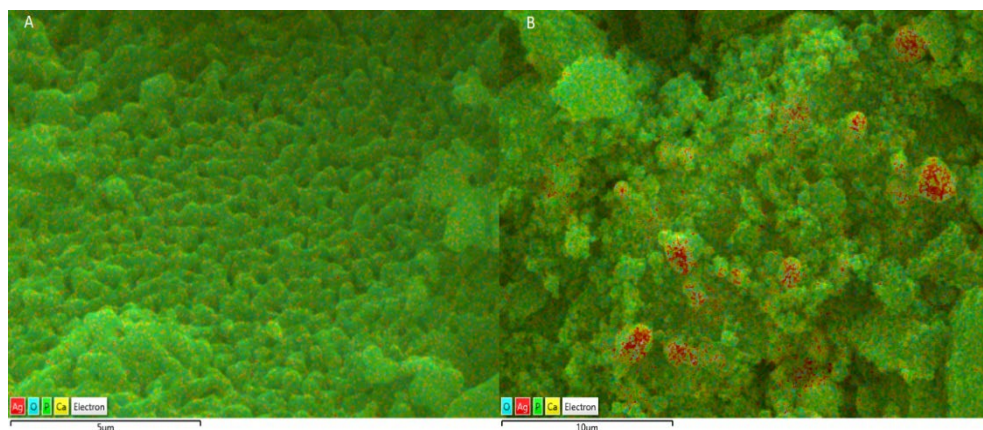
Figure 14. EDS images for (A) C-Ag-HAP and (B) Sp-Ag-HAP

CONCLUSIONS

In the present study our aim was the comparison of the methods used for the preparation of Ag-doped HAP. For this purpose, several methods (some of them can be also found in the literature) were employed using silver from different sources (colloidal silver, silver nitrate or silver complex). The obtained nanoparticles were characterized by SEM, EDS and XRD measurements. The solid-state method using $AgNO_3$ as silver source enabled the highest incorporated silver amount (10%). The obtained nanomaterial (Sp-Ag-HAP) could have potential application as a novel antimicrobial material.

EXPERIMENTAL SECTION

Materials

Chemicals

Calcium nitrate tetrahydrate ($Ca(NO_3)_2 \cdot 4H_2O$, (purity ≥ 99%), diammonium hydrogen phosphate ($(NH_4)_2HPO_4$, (purity ≥ 98.0%), ammonia solution (25%) were purchased from Carl Roth GmbH (Germany). Silver nitrate ($AgNO_3$, purity ≥ 99%) and sodium borohydrate ($NaBH_4$, purity ≥ 98%) are products of Sigma-Aldrich. All other reagents were of analytical grade (Merck, Germany) and used without further purification.

Equipments

The morphology, particle size and chemical elemental composition of silver-doped HAP were observed by scanning electron microscopy coupled with energy-dispersive X-ray diffraction (SEM/EDS). An Apreo SEM (Thermo Fisher, USA) equipped with Octane Elect EDS (AMETEK, USA) was used at 20.0 kV. The crystal structure was identified by X-ray diffraction (Bruker D8 Advance, Germany) with CuKα radiation (λ=1.54060 Å) operated at 40 kV and 40 mA.

The XRD analysis was performed on a Shimadzu XRD 6000 (Japan) using CuKα radiation at 40Kv, 30mA, at λ=1.542 Å. X-Ray images were prepared for each material. The red lines indicate the characteristic signs of the HAP crystals 25,8 32,05 39,84 46,78 49,53 53,13 63,97. The spectrum was identified by the ICPDS 09-0432 code in database.

Methods

Wet precipitation methods

1. Synthesis of colloidal silver-doped hydroxyapatite (C-Ag-HAP, C-Ag-HAP-sint)

For the synthesis of colloidal silver-doped hydroxyapatite the first step consisted of preparation of the silver source. 2 mL of an 1mM $AgNO_3$ solution cooled on ice was added to 30mL solution of $NaBH_4$ (2mM).

Hydroxyapatite was prepared according to our previously reported method [32],[33]. For preparation of HAP nanoparticles a 0.09M $(NH4)_2HPO_4$ (250mL, pH 11) was added to a 0.15M $Ca(NO_3)_2$ (250mL, pH 11) solution using a peristaltic pump with a flow rate of 25mL/min. The colloidal silver solution was added to the hydroxyapatite solution and the reaction mixture was stirred for 24 hours at room temperature. pH 11 was maintained for the whole reaction time. After completion of the reaction, the mixture was filtered under vacuum and washed with deionized water (3x 50mL). The obtained silver doped HAP nanoparticles (*C-Ag-HAP*) were dried at 200℃ for 12 hours. Part of the obtained sample was calcined at 1000℃ (*C-Ag-HAP-sint)*.

2. Synthesis of AgNO₃ doped Hydroxyapatite (Ag-HAP, Ag-HAP-sint)

The solution of 0.015M $AgNO_3$ (25mL) was added to the solution of 0.135 M calcium nitrate tetrahydrate (225mL). The resulted mixture was sonicated for 10 minutes, then a solution of 0.09 M of diammonium hydrogen phosphate solution (250mL) was added using a peristaltic pump (25 ml/min). The pH of the solution was adjusted to 11 and stirred continuously for 24 hours at room temperature. After the reaction time, it was filtered under vacuum, washed with deionized water, dried at 200℃ for 12 hours, and part of the sample was calcined at 1000℃.

3. Preparation of silver complex-doped hydroxyapatite (Co-Ag-HAP-noncal, Co-Ag-HAP-cal600ºC, Co-Ag-HAP-cal800ºC)

For the preparation of the diamine-silver hydroxide complex, into the solution of $AgNO_3$ in ammonia (25%) was added until the precipitation of silver oxide. The mixture was centrifuged and the obtained silver oxide was redissolved in 5mL of ammonia solution (25%).

Hydroxyapatite was prepared as described in section 1. To the solution of calcium nitrate tetrahydrate and diammonium hydrogen phosphate the silver hydroxide solution was added. The pH of the reaction mixture was adjusted to 11 with ammonia solution, stirred continuously for 24 hours at room temperature, filtered, washed, dried and the resulting sample was then divided into three parts. The first sample was not calcined *Co-Ag-HAP-noncal*, while

the second and third samples were calcined at 600℃ *Co-Ag-HAP-sint600ºC* for 1 hour. The third sample was calcined at 800℃ for another 1 hour (*Co-Ag-HAP-cal800ºC)*.

Solid state method

Preparation of the solid phase Ag-Hap (Sp-Ag-HAP)

The preparation of the hydroxyapatite was achieved using the steps described in section 1. For preparation of HAP nanoparticles a 0.09M $(NH4)_2HPO_4$ (pH 11) was added to a 0.15M $Ca(NO_3)$ (pH 11) solution using a peristaltic pump with a flow rate of 25mL/min. The reaction mixture was stirred for 24 hours at room temperature. pH 11 was maintained for the whole reaction time. After completion of the reaction, the mixture was filtered under vacuum and washed with deionized water.

1.1 g of the obtained hydroxyapatite and 0.22g of $AgNO_3$ were crushed to a fine powder in an Agate mortar, and the resulting powder was calcined at 500℃ (1 hour) and then 800℃ (1 hour). After calcination, the previously white sample turned brown.

ACKNOWLEDGMENTS

REFERENCES

1. T. Ivankovic; H. Turk; J. Hrenovic; Z. Schauperl; M. Ivankovic; A. Ressler, *J. Hazard. Mater.*, **2023**, 458, 131867.
2. A. Luceri; R. Francese; D. Lembo; M. Ferraris; C. Balagna, *Microorganisms*, **2023**, *11(3)*, 629.
3. B. Le Ouay; F. Stellacci, *Nano Today*, **2015**, *10(3)*, 339–354.
4. A. Gibała; P. Żeliszewska; T. Gosiewski; A. Krawczyk; D. Duraczyńska; J. Szaleniec; M. Szaleniec; M. Oćwieja, *Biomolecules*, **2021**, *11(10)*, 1–20.
5. S. Durdu; E. Yalçin; A. Altinkök; K. Çavuşoğlu, *Sci. Rep.*, **2023**, *13(1)*, 1–13.
6. M. L. W. Knetsch; L. H. Koole, *Polymers (Basel)*, **2011**, *3(1)*, 340–366.
7. W. T. J. Ong; K. L. Nyam, *Saudi J. Biol. Sci.*, **2022**, *29(4)*, 2085–2094.
8. L. Owen; K. Laird, *J. Appl. Microbiol.*, **2021**, *130(4)*, 1012–1022.
9. S. P. Rivera-Sánchez; I. D. Ocampo-Ibáñez; J. A. Silva-Leal; L. J. Flórez-Elvira; A. V. Castaño-Hincapié; A. Dávila-Estupiñan; J. I. Martínez-Rivera; A. Pérez-Vidal, *Sci. Rep.*, **2020**, *10(1)*, 1–7.

10. S. S. Jeremiah; K. Miyakawa; T. Morita; Y. Yamaoka; A. Ryo, *Biochem. Biophys. Res. Commun.*, **2020**, *533(1)*, 195–200.
11. Q. He; J. Lu; N. Liu; W. Lu; Y. Li; C. Shang; X. Li; L. Hu; G. Jiang, *Nanomaterials*, **2022**, *12(6)*, 1–13.
12. P. N. J. Arjun; B. Sankar; K. V. Shankar; N. V. Kulkarni; S. Sivasankaran; B. Shankar, *Coatings*, **2022**, *12*, 11.
13. G. Wei; P. X. Ma, *Biomaterials*, **2004**, 25(19), 4749–4757.
14. R. Barabás; E. de Souza Ávila; L. O. Ladeira; L. M. Antônio; R. Tötös; D. Simedru; L. Bizo; O. Cadar, *Arab. J. Sci. Eng.*, **2020**, *45(1)*, 219–227.
15. N. Kantharia; S. Naik; S. Apte; M. Kheur; S. Kheur; B. Kale, *J. Dent. Res. Sci. Dev.*, **2014**,1(1), 15.
16. R. Barabás; M. Rigó; M. Eniszné-Bódogh; C. Moisa; O. Cadar, *Studia UBB Chemia*, **2018**, *63(3)*, 137–154.
17. A. Sobczak-Kupiec; A. Drabczyk; W. Florkiewicz; M. Głąb; S. Kudłacik-Kramarczyk; D. Słota; A. Tomala; B. Tyliszczak, *Materials (Basel).*, **2021**,*14*, 9.
18. J. S. Cho; D. S. Yoo; Y. C. Chung; S. H. Rhee, *J. Biomed. Mater. Res. - Part A*, **2014**, *102(2)*, 455–469.
19. P. Yang; Z. Quan; C. Li; X. Kang; H. Lian; J. Lin, *Biomat.*, **2008**, *29(32)*, 4341–4347.
20. N. A. S. Mohd Pu'ad; R. H. Abdul Haq; H. Mohd Noh; H. Z. Abdullah; M. I. Idris; T. C. Lee, *Mater. Today Proc.*, **2019**, *29*, 233–239.
21. Z. Khurshid; M. S. Zafar; S. Hussain; A. Fareed; S. Yousaf; F. Sefat, *Handb. Ion. Substituted Hydroxyapatites*, 237–257, **2019**.
22. S. S. A. Abidi; Q. Murtaza, *UPB Sci. Bull. Ser. B Chem. Mater. Sci.*, **2013**, *75(3)*, 3–12.
23. C. S. Ciobanu; S. L. Iconaru; M. C. Chifiriuc; A. Costescu; P. Le Coustumer; D. Predoi, *Biomed Res. Int.*, **2013**.
24. P. N. Lim; E. Y. Teo; B. Ho; B. Y. Tay; E. S. Thian, *J. Biomed. Mater. Res. - Part A*, **2013**,101 A, 9, 2456–2464.
25. J. Suwanprateeb; F. Thammarakcharoen; K. Wasoontararat; W. Chokevivat; P. Phanphiriya, *J. Mater. Sci. Mater. Med.*, **2012**, *23(9),* 2091–2100.
26. M. Roy; G. A. Fielding; H. Beyenal; A. Bandyopadhyay; S. Bose, *ACS Appl. Mater. Interfaces*, **2012**, 4(3), 1341–1349.
27. M. Vukomanović; I. Braçko; I. Poljanşek; D. Uskoković; S. D. Şkapin; D. Suvorov, *Cryst. Growth Des.*, **2011**, *11(9)*, 3802–3812.
28. M. Li; M. J. Mondrinos; X. Chen; M. R. Gandhi; F. K. Ko; P. I. Lelkes, *J. Biomed. Mater. Res. Part A*, **2006**, *79(4)*, 963–73.
29. N. Iqbal; M. R. Abdul Kadir; N. A. N. Nik Malek; N. Humaimi Mahmood; M. Raman Murali; T. Kamarul, *Mater. Lett.*, **2012**, *89*, 118–122.
30. N.-I. Farkas; L. Marincaş; L. Barbu-Tudoran; R. Barabás; G. L. Turdean, *J. Funct. Biomater.*, **2023**,*14(6)*, 331.
31. P. Narendran; A. Rajendran; M. Garhnayak; L. Garhnayak; J. Nivedhitha; K. C. Devi; D. K. Pattanayak, *Colloids Surf. B Biointerfaces*, **2018**, *169*, 143–150.
32. R. Barabás; N. I. Farkas; C. L. Nagy; O. Cadar; C. Moisa; L. Bizo, *Ceram. Int.*, **2021**, *47(6)*, 8584–8592.
33. V. R. Dejeu; B. Reka; A. M. Cormoş; B. E. Sára; P. Ş. Agachi, *Studia UBB Chemia*, **2010**, *55(2, 1)*, 179–188.

THERMO-CATALYTIC PYROLYSIS OF LIGNOSULFONATE FROM THE SULFITE PROCESS

Gabriel VASILIEVICI[a], Andreea-Luiza MÎRȚ[a,b,*], Simona-Bianca GHIMIȘ[a], Grigore PȘENOVSCHI[a,b], Mihai SÎRBU[c]

ABSTRACT. This paper shows the results of thermal and catalytic pyrolysis of conditioned lignosulfonate from the sulfite process, with a specific focus on the analysis of bio-oil and biochar. The conditioning of lignosulfonate was made by drying and grinding in a planetary ball mill. Thermal and catalytic pyrolysis of conditioned lignosulfonate were carried out under the same temperature and flow conditions. The use of two different catalysts produced via the impregnation method has shown distinctive effects, influencing both bio-oil yield and chemical composition. The resulting biochar exhibits characteristics comparable to non-activated carbonaceous materials, with variations in its specific surface area and pore size depending on the catalyst.

Keywords: catalytic pyrolysis, lignosulfonate, sulfite process, bimetallic catalyst

INTRODUCTION

Catalytic biomass pyrolysis is a promising technology for the efficient utilization of biomass, converting it into high-quality liquid fuels and chemicals in a single reactor and through a single step [1-3]. In the absence of oxygen, at high temperatures, organic matter undergoes thermochemical decomposition

---

[a] *National Institute for Research & Development in Chemistry and Petrochemistry–ICECHIM, 202 Spl. Independentei, 060021 Bucharest, Romania*
[b] *Faculty of Chemical Engineering and Biotechnologies, University Politehnica of Bucharest, 1-7 Polizu Street, 011061 Bucharest, Romania*
[c] *CCH – The Cellulose and Paper Plant, 2 Nicolae Iorga Bvd., Drobeta-Turnu Severin 220236, Mehedinti, Romania*
[*] *Corresponding author: luiza.mirt@icechim.ro*

known as pyrolysis or destructive distillation, resulting biochar, liquid part bio-oil and gases [4]. The term "pyrolysis" has its roots in the Greek language, where "pyro" means "fire," and "lysis" translates as "separation" [5].

In the pursuit of valorizing secondary streams from industrial processes, pulp and paper mills are striving to optimize their biomass utilization. Spent sulfite liquor, also known as red liquor, constitutes a waste byproduct of the sulfite process employed in cellulose production from lignocellulosic biomass [6]. This biomass, a fundamental resource for paper and regenerated cellulose fiber manufacturing, undergoes a sulfite-based treatment to yield high-quality cellulose through lignin and hemicellulose removal [7-8].

The resultant red liquor is notably rich in monomeric sugars and lignosulfonates, historically exploited as a substrate for industrial-grade ethanol production [9].

Pyrolysis involves the rapid and simultaneous depolymerization and fragmentation of biomass components such as cellulose, hemicellulose, and lignin, bio-oil is generated [10]. The resulting pyrolysis oil, also known as bio-oil, can be obtained with impressive yields of up to 70-80% by weight, contingent upon the proportions of cellulose and lignin present in the wood material [11]. Bio-oil, a microemulsion, consists of two phases: one is an aqueous solution containing decomposition products of cellulose, hemicellulose and smaller molecules from lignin decomposition, while the other primarily comprises pyrolytic lignin macromolecules [12].

Due to the significant content of oxygenated compounds, particularly lignin derivatives, bio-oils possess relatively low heating values, exhibit inherent instability, high viscosity, low volatility, and corrosive properties. As certain lignin oligomers resist vaporization during pyrolysis, comprehensive identification of all compounds using GC-MS analysis, poses challenges [13-15]. Consequently, the upgrading of bio-oil is necessary to improve its properties prior to utilization [16-17].

The solid residue produced during pyrolysis, known as biochar, primarily comprises carbon (approximately 85%), along with oxygen and hydrogen. It retains a significant portion of the inorganic components found in the original biomass [11]. Biochar holds considerable value as a by-product and can serve various purposes, including as a solid fuel for boilers, utilized in processes such as steam reforming or thermal cracking to generate hydrogen or syngas [18-19] and as a medium for filtering and adsorbing both organic and inorganic pollutants [3, 20-22].

Catalytic pyrolysis of lignosulfonate from the sulfite process for the production of aromatic compounds such as BTX (benzene, toluene, xylene) has been conducted using modified H-ZSM-5 zeolite catalysts with Ga, Mo, and Zn in microreactors under inert gas atmosphere, as reported in literature [23-24].

However, the catalysts' lifespan is limited due to carbonaceous material formation. The irreversible deactivation of the acidic sites by inorganic cations (Na^+, K^+, Ca^{2+}) present in high concentrations in the feedstock poses a significant challenge, leading to decreased acidity and subsequently lower conversion to aromatic compounds [25].

In co-processing studies of lignosulfonate and plastic waste (polyolefins and polystyrene) in fluidized bed reactors, catalysts for olefin cracking, catalytic cracking catalysts (such as ZSM-5), and gamma-alumina have been employed [26-27].

Catalytic pyrolysis of lignin in the presence of catalysts such as NiO, MoO_2, and Co_3O_4 has the potential to inhibit bio-char formation and enhance the properties of bio-oil by reducing the concentration of oxygenated compounds hours [28-29]. The addition of catalysts leads to increased bio-oil yield, particularly in the presence of 10% added hydrogen in the inert atmosphere. The bio-oil yield increased by 26.38% through catalytic pyrolysis using Co_3O_4 catalyst in an H_2/N_2 atmosphere [30].

This paper presents innovative processes for lignosulfonate process by pyrolysis. Catalytic pyrolysis was carried out in the presence of new catalysts obtained by the impregnating method of Mo and Ni precursors on alumina support. The study explores the potential of catalytic pyrolysis as a conversion method for transforming lignosulfonate from sulfite process into valuable products.

RESULTS AND DISCUSSION

Lignosulfonate characterization

The lignosulphonate used in the experimental programme was derived from waste liquor generated during the production of wood pulp through the sulphite process. The raw lignosulfonate sample was analyzed by determining the dry matter content after water removal, ash content (calcination residue) and thermal analysis (thermogravimetric analysis TGA).

Table 1. Characterization of lignosulfonate samples

Sample	Dry substance content, %	Calcination residue, %	pH
Lignosulfonate	52.56	37.54%	8.20 (25ºC)

The thermogravimetric analysis shows the thermal behavior of the sample, revealing distinct mass loss patterns at various temperature ranges. Initially, a mass loss of 6.05% is observed up to 140ºC, which can be attributed to the presence of water and volatile components in the sample. Subsequently, within the temperature range of 180-550ºC, the mass loss curve exhibits three distinct peaks at 218.3ºC, 270.4ºC, and 395.0ºC. These peaks correspond to the decomposition of hemicellulose and lignin [31]. The cumulative mass loss associated with these peaks yields an organic matter content of 37.48% within the solid portion of the sample lignosulfonate. Furthermore, the residue obtained at 750ºC under ambient air conditions is recorded as 47.61%.
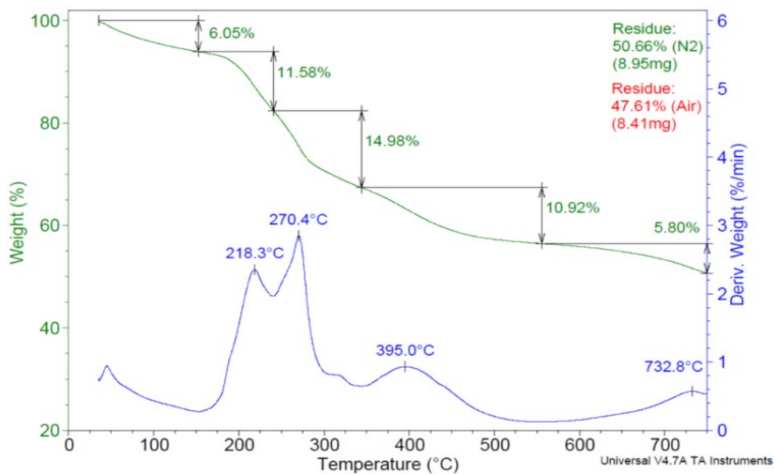
Figure 1. Thermogravimetric analysis of lignosulfonate

Conditioning lignosulfonate samples

The lignosulfonate samples were conditioned before pyrolysiss by drying in a circulating air oven and then grinding in a planetary ball mill.

The resulting lignosulfonate powder was analyzed by DLS method (dynamic light scattering) to evaluate the particle size of lignosulfonate and size distribution. The lignosulfonate particles are polydisperse, forming large aggregates, the results being presented in table 2 and figure 2.

Table 2. Characteristics of lignosulfonate particles

Sample	Dm (nm)	PdI	Observations
Lignosulfonate	1337	0.820	Polydisperse, contains numerous large aggregates, with dimensions > 6µm
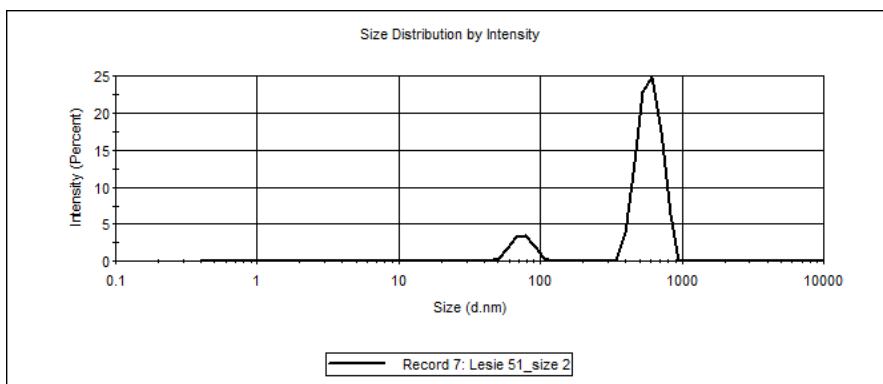
Figure 2. Particle size distribution as a function of intensity

Catalyst characterization

The structural characteristics of the catalysts were examined using nitrogen porosimetry and are presented in Table 3. Prior to analysis, the catalyst samples were subjected to a vacuum degassing process for 4 hours at 160ºC. The resulting catalysts are mesoporous materials with pore diameters ranging from 4 nm to 10 nm.

Table 3. Characteristics of catalysts

No.	Catalyst name	Specific surface, m^2/g	Total pore volume, cm^3/g	Average pore diameter, nm
2	Mo/Al$_2$O$_3$	157.3	0.244	6.207
3	NiMo/Al$_2$O$_3$	236.8	0.2839	4.795

Thermal pyrolysis of lignosulfonate

The analysis of the bio-oil obtained by thermal pyrolysis of conditioned lignosulfonate is presented in Table 4 and Figure 3. The GC-MS chromatogram shows a multitude of peaks. The liquid phase's composition show the presence of oxygenated compounds with an aromatic structure - phenols and substituted phenols, linear and cyclic oxygenated aliphatic compounds, including carbonyl compounds, acids, and alcohols.

GABRIEL VASILIEVICI, ANDREEA-LUIZA MÎRŢ, SIMONA-BIANCA GHIMIŞ,
GRIGORE PŞENOVSCHI, MIHAI SÎRBU

Table 4. GC-MS analysis of bio-oil pyrolysis of lignosulfonate without catalyst

Peak Number	Retention Time	Compounds name
1	5.335	2-Butanone, 3-hydroxy-
2	5.551	Acetic anhydride
3	6.460	2-Hepten-1-ol, (E)-
4	7.322	Acetic acid
5	7.561	2-Propanone, 1-(acetyloxy)-
6	9.484	Butanoic acid
7	9.907	Furfuryl alcohol
8	11.415	1,3-Cyclopentanedione, 2,4-dimethyl-
9	11.495	Cyclohexanone, 2-acetyl-
10	11.822	2-Cyclopenten-1-one, 2-hydroxy-3-methyl-
11	12.029	Cyclohexanone, 2-acetyl-
12	12.173	Phenol, 2-methoxy-
13	13.649	Phenol
14	16.146	Phenol, 2,6-dimethoxy-
15	19.473	2-Propanone, 1-(4-hydroxy-3-methoxyphenyl)-
16	23.646	Desaspidinol
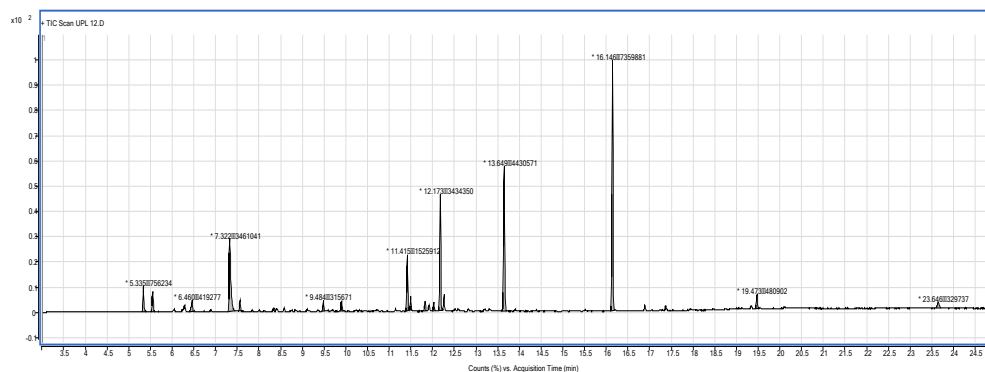
Figure 3. Chromatogram of bio-oil pyrolysis of lignosulfonate without catalyst

The porosimetry data of biochar was obtained by nitrogen adsorption measurements with NOVA 2200e-Quantachrome apparatus. The obtained results showed that pyrolyzing the residues yields carbonaceous materials characterized by a reduced specific surface area and pore volume, yet retaining

adsorption capabilities for chemical compounds. Conversely, biochar possessing an increased surface area is considered more porous, which makes it appropriate for applications like water treatment and environmental remediation [32-33].

Table 5. Porosimetry characteristics of biochar

No.	Sample name	Specific surface, m^2/g	Total pore volume, cm^3/g	Average pore diameter, nm
1	Biochar	1.982	0.0045	9.101

Catalytic pyrolysis of lignosulfonate

The GC-MS analysis of the bio-oil produced using Mo/Al_2O_3 are shown in Table 6 and Figure 5. The homogenization of the catalyst and conditioned lignosulfonate particles was done by grinding them together in the planetary ball mill.

Table 6. GC-MS analysis of bio-oil pyrolysis in the presence of Mo/Al_2O_3

Peak Number	Retention Time	Compounds name
1	4.745	2-Butanone, 3-hydroxy-
2	4.929	2-Propanone, 1-hydroxy-
3	5.567	Furan, 3-methyl-
4	6.253	Acetic acid
5	6.684	1,2-Ethanediol, diacetate
6	7.474	Propanoic acid
7	7.681	2-Cyclopenten-1-one, 2,3-dimethyl-
8	8.511	Butanoic acid
9	10.434	1,3-Cyclopentanedione, 2,4-dimethyl-
10	11.192	Phenol, 2-methoxy-
11	12.644	Phenol
12	12.915	Phenol, 4-ethyl-2-methoxy-
13	15.174	Phenol, 2,6-dimethoxy-
14	15.892	Phenol, 4-methoxy-3-(methoxymethyl)-
15	16.370	Benzene, 1,2,3-trimethoxy-5-methyl-
16	18.477	2-Propanone, 1-(4-hydroxy-3-methoxyphenyl)-
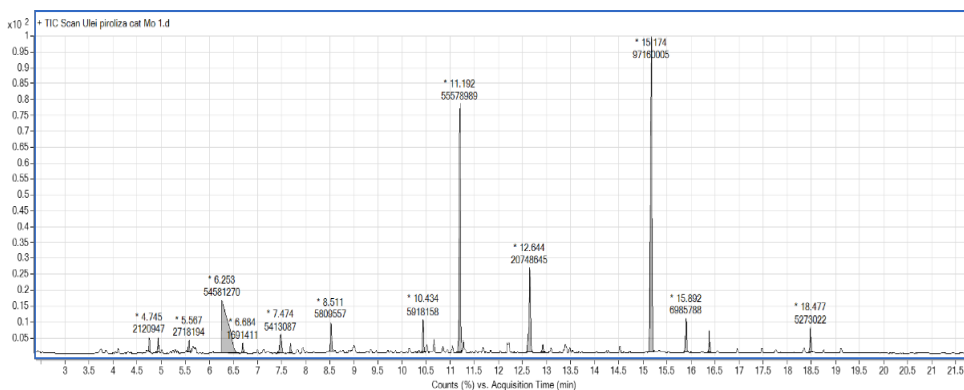
Figure 4. Chromatogram of bio-oil pyrolysis in the presence of Mo/Al₂O₃
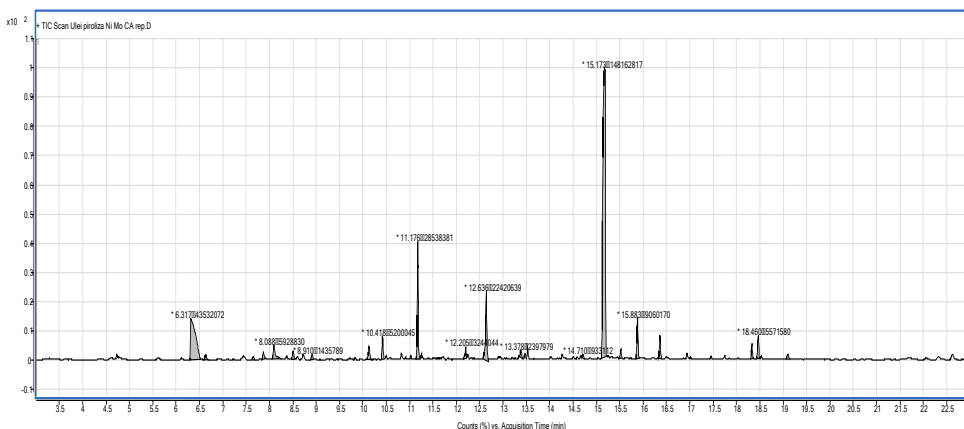
Figure 5. Chromatogram of bio-oil pyrolysis in the presence of Ni-Mo/Al₂O₃

A catalytic pyrolysis was performed using a nickel and molybdenum based bimetallic catalyst. The results acquired through GC-MS analysis of the bio-oil are shown in Table 7 and Figure 6. This bio-oil analysis resulting from catalytic pyrolysis shows the presence of numerous aromatic compounds, compared to conventional pyrolysis. This enhancement can be attributed to the catalytic active sites that facilitate the deoxygenation of compounds within the lignosulfonate [34-35].

Table 7. GC-MS analysis f bio-oil pyrolysis in the presence of Ni-Mo/Al$_2$O$_3$

Peak Number	Retention Time	Compounds name
1	6.317	Acetic acid
2	6.628	2-Propanone, 1-(acetyloxy)-
3	7.649	2-Cyclopenten-1-one, 2,3-dimethyl-
4	7.872	2-Propanone, 1-hydroxy-
5	8.088	Propylene Glycol
6	8.503	Butanoic acid
7	8.910	2-Furanmethanol
8	10.130	Acetamide
9	10.418	1,3-Cyclopentanedione, 2,4-dimethyl-
10	11.176	Phenol, 2-methoxy-
11	12.205	1,2,3 Trimethoxybenzene
12	12.636	Phenol
13	13.378	Phenol, 2,4-dimethyl-
14	14.710	Phenol, 2-ethyl-4-methyl-
15	15.173	Phenol, 2,6-dimethoxy-
16	15.524	Phenol, 2,6-dimethoxy-, acetate
17	15.883	1,2,4-Trimethoxybenzene
18	16.362	Benzene, 1,2,3-trimethoxy-5-methyl-
19	18.333	Ethanone, 1-(4-hydroxy-3-methoxyphenyl)-
20	18.460	2-Propanone, 1-(4-hydroxy-3-methoxyphenyl)-
21	19.099	Phenol, 2,6 - dimethoxy -4-(2-propenyl)

Utilizing GC-MS analysis, it was found that the liquid phase includes oxygenated compounds characterized by aromatic structures, phenolic compounds, furans, substituted benzene and linear/cyclic aliphatic oxygenated compounds - carbonyl compounds and organic acids. It was observed that the presence of a Mo-based catalyst during pyrolysis resulted in a higher concentration of organic acids and a higher concentration of furanic compounds compared to a Ni-Mo based catalyst. The obtained results supports the findings reported in the literature [36]. Molybdenum-based catalysts exhibit C-C bond cleavage in the side chains, leading to significant production of carboxylic compounds [37-38]. Adding nickel, in contrast, suppresses the reaction between aromatics and other oxygenated substances, yielding a variety of alkylated aromatic compounds [39-40].

Table 8. Overview of the results from pyrolysis experiments

Identified compounds	Without catalyst	Mo catalyst, %	Ni-Mo catalyst, %
Furanic compounds	1.15	0.99	0.48
Aliphatic ketones	15.77	6.47	7.77
Organic acids	15.42	24.03	17.29
Phenolic compounds	62.17	66.46	68.76
Other compounds	5.49	2.06	5.70

Table 9 below shows the characteristics of biochar, which has similar attributes of non-activated carbons. Moreover, the presence of molybdenum-based catalysts during pyrolysis reactions partially contributes to the destruction of the biochar's micropores. Bimetallic catalysts often display a synergistic effect, significantly increasing the pyrolysis reaction, especially when compared to monometallic catalysts [41]. The pyrolysis with bimetallic catalysts resulted in materials with higher specific surface area and pore volume compared to the use of monometallic catalysts (approximately 7 times larger), accompanied by a 50% reduction in average pore size.

Table 9. Porosimetry analysis of biochar

No.	Catalyst	Specific surface, m^2/g	Total pore volume, cm^3/g	Average pore diameter, nm
1	Biochar with Mo/Al$_2$O$_3$ catalyst	0.40	0.0020	20.19
2	Biochar with Ni-Mo/Al$_2$O$_3$ catalyst	15.59	0.0269	6.90

CONCLUSION

This study presents the conditioning of lignosulfonate from the sulfite method used in the production of cellulose from lignocellulosic biomass and thermal and catalytic pyrolysis of conditioned lignosulfonate, focusing on the production and analysis of bio-oil and biochar. The obtained results provide valuable insights into the impact of catalytic pyrolysis of lignosulfonate and its potential applications. The utilization of molybdenum and nickel-molybdenum catalysts showcased distinctive effects on the bio-oil yield, chemical composition and product distribution. The GC-MS analysis revealed various compounds, including oxygenated species like phenols, furans, aliphatic compounds, and carbonyl compounds within the liquid phase of the bio-oil. Porosimetric analysis of the biochar resulting from pyrolysis shows the catalyst's role in determining biochar porosity. The presence of molybdenum catalyst leads to biochar with

reduced specific surface area, whereas the utilization of a nickel-molybdenum-based catalyst substantially enhances it. The effects of using catalytic pyrolysis compared to non- catalytic pyrolysis to recycle the lignosulfonate residue and to characterise the materials obtained from this process are presented.

EXPERIMENTAL PART

Lignosulfonate characterization

The gravimetric method was used to determine the dry substance content of lignosulfonate samples. Water was removed from the samples by subjecting them to heat in an air circulation oven at 85ºC for 8 hours, followed by further heating at 105ºC for 16 hours. Subsequently, the samples were heated to 100ºC under a vacuum of 4 mmHg pressure until a constant mass was achieved. To assess the pH of lignosulfonate, a portable pH-meter model 1140 (Mettler Toledo Gmbh-Switzerland) was utilized, with measurements at room temperature (25ºC).

For the evaluation of the ash content (calcination residue), the solid fraction of the red liquor, obtained through calcination in a furnace, was employed. The temperature of the furnace was gradually increased from room temperature to 850ºC, with a heating rate of 5ºC/min. Intermediate steps at 250ºC and 500ºC were incorporated, each lasting 2 hours. The resulting residue was then correlated with the dry substance content of the lignosulfonate samples.

Thermogravimetric analysis (TGA) was performed with a TA Q5000 (TA Instruments, New Castle, DE, USA). The sample, approx. 17.6 mg - the solid part of the red liquor sample, was heated from room temperature to 750ºC at a heating rate of 10ºC/min in an inert gas (nitrogen) atmosphere at a flow rate of 50 mL/min recording mass changes; and switching the inert gas with synthetic air at 750ºC to record the residue resulted in air.

Conditioning of lignosulfonate

The lignosulfonate samples were conditioned in two steps before pyrolysiss. First step involve drying in an circulating air oven at 85ºC for 8 hours, followed by heating at 105ºC for 16 hours.

Second step was grinding of lignosulfonate in a planetary ball mill, Retsch PM100 from Retsch GmbH, Haan, Germany, with Φ10mm stainless steel balls in a 125 ml stainless steel grinding jar.

The measurement of lignosulfonate particles was conducted using a particle size measurement system comprising a Zetasizer Nano ZS instrument (Red badge) from Malvern Instruments Ltd.,UK, and a computer with Zetasizer

software for sample measurement control. The Zetasizer Nano instruments perform particle size measurements using the technique Dynamic Light Scattering (DLS) [42]. This measures fluctuations in the intensity of scattered light and uses these fluctuations to calculate the size of the particles in the sample. DLS measures Brownian motion and correlates it with particle size.

Particles suspended in a liquid undergo continuous movement due to Brownian motion, so smaller particles move faster and larger particles move slowly. When larger particles, which move more slowly, are measured, the intensity of scattered light will vary gradually. Similarly, for smaller particles, since they move very quickly, the intensity of scattered light will also fluctuate rapidly [42-44]. For the DLS analysis the samples were prepared as follows: 0.2 mL sample was diluted to the mark with distilled water in a 25 mL volumetric flask. For each sample a minimum of 5 measurements were performed and the measurement with the values closest to the mean value was selected.

Catalyst preparation and characterization

Catalysts for pyrolysis were prepared in the laboratory through the impregnation method.The catalysts were synthesized employing the wet impregnation method on the alumina powder support, using aqueous solutions of $MoO \cdot 3H_2O$ and $Ni(NO_3)_2 \cdot 6H_2O$. The metallic precursors, dissolved in the aqueous ammonia solution, were incorporated into the solutions of $MoO_3 \cdot H_2O$ and $Ni(NO_3)_2 \cdot 6H_2O$ under continuous stirring. Subsequently, the resultant mixture was used for the support impregnation at room temperature. The impregnated sample was air-dried overnight at room temperature, followed by additional drying in a 120°C air circulation oven for 12 hours. The last step was calcination in a furnace at 450°C for 5 hours. The prepared catalysts were named Mo/Al_2O_3, and $Ni-Mo/Al_2O_3$.

The textural characteristics of catalysts and biochars were analysed by nitrogen adsorption measurements with NOVA 2200e-Quantachrome apparatus from Quantachrome Instruments, USA. Analysis of data was conducted using NovaWin software ver. 11.03. All the samples were vacuum degassed before analysis at 300°C for 4 h.The specific surface area was determined through the B.E.T. (Brunauer-Emmett-Teller) method by analyzing the linear plot of the adsorption isotherm. Total pore volume and pore size distribution were estimated based on the adsorbed N_2 quantity. The total pore volume was calculated from single-point adsorption at a relative pressure near unity, while the average pore diameter was derived from the adsorption average pore diameter using the surface area determined through the B.E.T. method.

Pyrolysis

The pyrolysis reactor used in processing the lignosulfonate has a horizontal, batch-operated configuration, composed of stainless steel, with an inner diameter of Ø 25.4mm and a length of 250mm. The reactor integrates a thermocouple for internal temperature measurement. For heating, a digitally controlled electric oven at external wall thermocouple is employed.

Before each experiment, inert gas (nitrogen) is purged into the reactor to remove oxygen. The pyrolysis reactor was fed with a homogenized mixture of lignosulfonate with 1% catalyst, prepared by grinding in a planetary ball mill. Figure 7 shows a schematic representation of the pyrolysis reactor, where inert gas flow is regulated using a mechanical valve and a flow meter. The resulting pyrolysis products undergo cooling in a heat exchanger and subsequently enter a gas-liquid separator. The liquid fraction is collected, prepared, and subjected to analysis by gas chromatography (GC-MS).
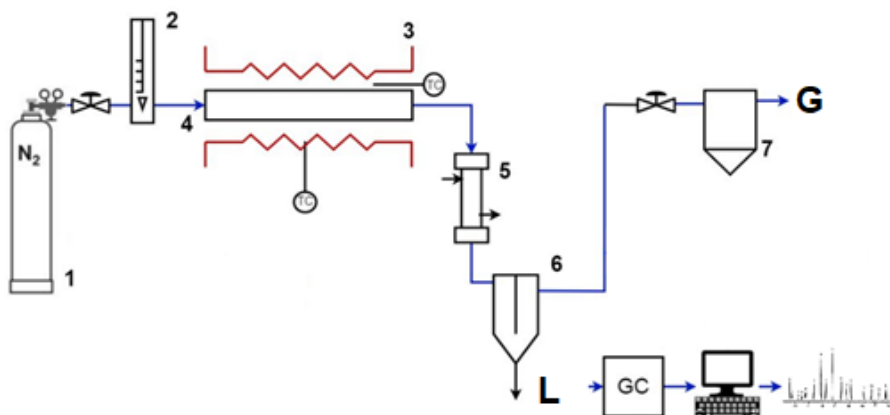
Figure 6. Schematic representation of pyrolysis reactor. 1-inert gas cylinder, 2-flow meter, 3- electric heating oven, 4- pyrolysis reactor, 5-heat exchanger (cooler), 6- gas-liquid separator, 7-gas container, TC- thermocouple and heat display system, GC- gas chromatograph

The pyrolysis reactions were conducted at 500°C for 4 hours, with the reactor ramped up to the operational temperature at a rate of 20°C/min. The mixture of conditioned lignosulfonate and catalyst was grinded and subsequently introduced into the reactor within ceramic nacelles. The catalyst concentration was maintained at 2% (mass) relative to the lignosulfonate mass.

Bio-oil characterization

The liquid fraction's characterization was performed using GC-MS analysis with Agilent 7890 A GC-MS/MS TRIPLE QUAD system. A DB-WAX capillary column from Agilent (30 m length, 0.25 mm internal diameter, 0.25 µm film thickness) was utilized, with helium as the carrier gas flowing at 1 mL/min. The initial oven temperature was 70°C, gradually increased to 230°C at a rate of 4°C/min, holding for 5 minutes. The GC injector temperature was 250°C, while the MS detector was set to 150°C. The transfer line temperature was maintained at 280°C. MS detection occurred in the electron ionization (EI) mode at 70 eV, with a mass scanning range of m/z 50-450. The NIST MS database facilitated peak identification within the analyzed samples.

ACKNOWLEDGMENTS

REFERENCES

1. T. Y. A. Fahmy, Y. Fahmy, F. Mobarak, M. El-Sakhawy, R. E. Abou-Zeid; *Environ. Dev. Sustain.*, **2018**, *22 (1)*, 17-32.
2. H. Zhang, R. Xiao, J. Nie, B. Jin, S. Shao, G. Xiao; *Bioresour. Technol.*, **2015**, *192*, 68-74.
3. V. Goia, C.-C. Cormoş, P. Ş. Agachi; *Studia UBB Chemia*, **2011**, *56 (2)*, 49-56.
4. J. König, L. Walleij; Inst. Trätekn. Forskn., Stockholm, **1999**.
5. B. Östman; *Wood Mater. Sci. Eng.,* **2021**, *17 (1)*, 2-5.
6. R. Janzon, J. Puls, B. Saake; *Holzforschung*, **2006**, *60 (4)*, 347-354.
7. R. Hoheneder, E. Fitz, R. H. Bischof, H. Russmayer, P. Ferrero, S. Peacock, M. Sauer; *Bioresour. Technol.*, **2021**, *333*, 125215.
8. J. A. Sirvio, M. Mikola, J. Ahola, J. P. Heiskanen, S. Filonenko, A. Ammala; *Carbohydr. Polym.*, **2023**, *312*, 120815.
9. Z. Guo, L. Olsson; *Process Biochem.*, **2014**, *49 (8)*, 1231-1237.
10. G. Lyu, S. Wu, H. Zhang; *Front. Energy Res.*, **2015**, 3.
11. P. Basu; in Biomass Gasification, Pyrolysis, Torrefaction, **2013**; pp 147-176.
12. D. S. Scott, J. Piskorqt, M. A. Bergougnou, R. Graham, R. P. Overend; *Ind. Eng. Chem. Res.*, **1988**, *27*, 8-15.

13. C. Gerdes, C. M. Simon, T. Ollesch, D. Meier, W. Kaminsky; *Eng. Life Sci*., **2002**, *2 (6)*, 167-174.
14. Z. Zhang, D. J. Macquarrie, M. De bruyn, V. L. Budarin, A. J. Hunt, M. J. Gronnow, J. Fan, P. S. Shuttleworth, J. H. Clark, A. S. Matharu; *Green Chem*., **2015**, *17 (1)*, 260-270.
15. Q. Lu, Z.-b. Zhang, X.-c. Yang, C.-q. Dong, X.-f. Zhu; *J. Anal. Appl. Pyrolysis*, **2013**, *104*, 139-145.
16. T. Stoikos; in Biomass Pyrolysis Liquids Upgrading Utilization, A. V. Bridgwater, Ed., Elsevier Appl. Sci., **1991**.
17. Pattiya; in Direct Thermochem. Liquefaction Energy Appl., **2018**; pp 3-28.
18. H. B. Goyal, D. Seal, R. C. Saxena; *Renew Sust Energ Rev*., **2008**, *12 (2)*, 504-517.
19. G. W. Huber, S. Iborra, A. Corma; *Chem. Rev*., **2006**, *106*, 4044−4098.
20. L. Delgado-Moreno, S. Bazhari, G. Gasco, A. Mendez, M. El Azzouzi, E. Romero; *Sci. Total Environ*., **2021**, *752*, 141838.
21. D. Mohan, A. Sarswat, Y. S. Ok, C. U. Pittman Jr.; *Bioresour. Technol*., **2014**, *160*, 191-202.
22. M. Ahmad, A. U. Rajapaksha, J. E. Lim, M. Zhang, N. Bolan, D. Mohan, M. Vithanage, S. S. Lee, Y. S. Ok; *Chemosphere*, **2014**, *99*, 19-33.
23. D. J. Mihalcik, C. A. Mullen, A. A. Boateng; *J. Anal. Appl. Pyrolysis*, **2011**, *92 (1)*, 224-232.
24. A. Heeres, N. Schenk, I. Muizebelt, R. Blees, B. De Waele, A. J. Zeeuw, N. Meyer, R. Carr, E. Wilbers, H. J. Heeres; *ACS Sustainable Chem. Eng*., **2018**, *6 (3)*, 3472-3480.
25. A. Palčić, V. Valtchev; *Appl. Catal*., **2020**, *606*, 117-795.
26. A. Nechita Rotta, C. Bota, B. Brém, D. I. Porumb, E. Gál; *Studia UBB Chemia*, **2022**, *67 (4)*, 169-185.
27. M. Sajdak, R. Muzyka; *J. Anal. Appl. Pyrolysis*, **2014**, *107*, 267-275.
28. F. Liu, S. Xu, L. Cao, Y. Chi, T. Zhang, D. Xue; *J. Phys. Chem. C*, **2007**, *111*, 7396-7402.
29. Q. Wei, P. Zhang, X. Liu, W. Huang, X. Fan, Y. Yan, R. Zhang, L. Wang, Y. Zhou; *Front. Chem*., **2020**, *8*, 586445.
30. J. Chen, C. Liu, S. Wu, J. Liang, M. Lei; *RSC Adv*., **2016**, *6 (109)*, 107970-107976.
31. R. Sun, J. Tomkinson, G. L. Jones; *Polym. Degrad. Stabil*., **2000**, *68*, 111-118.
32. S. Roy, U. Kumar, P. Bhattacharyya; *Environ Sci Pollut Res Int*, **2019***, 26 (7)*, 7272-7276.
33. Z. Chen, T. Liu, J. Tang, Z. Zheng, H. Wang, Q. Shao, G. Chen, Z. Li, Y. Chen, J. Zhu, T. Feng; *Environ Sci Pollut Res Int*, **2018**, *25 (12)*, 11854-11866.
34. M. d. C. Rangel, F. M. Mayer, M. d. S. Carvalho, G. Saboia, A. M. de Andrade; *Biomass*, **2023**, *3 (1)*, 31-63.
35. X. Lu, X. Gu; *Biotechnol Biofuels Bioprod*, **2022**, *15 (1)*, 106.
36. P. Straka, O. Bičáková, T. Hlinčík; *Catalysts*, **2021**, *11* (12).
37. J. Yu, B. Luo, Y. Wang, S. Wang, K. Wu, C. Liu, S. Chu, H. Zhang; *Bioresour. Technol*., **2022**, *346*, 126640.
38. H. Yang, W. Yin, X. Zhu, P. J. Deuss, H. J. Heeres; *ChemCatChem*, **2022**, *14*, 20220097.

39. Y. Zheng, J. Wang, D. Li, C. Liu, Y. Lu, X. Lin, Z. Zheng; *J. Energy Inst*., **2021**, *97*, 58-72.
40. Y. L. Ding, H. Q. Wang, M. Xiang, P. Yu, R. Q. Li, Q. P. Ke; *Front Chem*, **2020**, *8*, 790.
41. M. Koehle, A. Mhadeshwar; *New Future Dev. Catal*., **2013**; 63-93.
42. J. Stetefeld, S. A. McKenna, T. R. Patel; *Biophys Rev*, **2016**, *8 (4)*, 409-427.
43. M. Kaszuba, D. McKnight, M. T. Connah, F. K. McNeil-Watson, U. Nobbmann; *J. Nanoparticle Res*., **2007**, *10 (5)*, 823-829.
44. J. Lim, S. P. Yeap, H. X. Che, S. C. Low; *Nanoscale Res. Lett*., **2013**, *8,* 381.

INVESTIGATION OF FERROUS CONGLOMERATE PARTICLES FOUND IN CARWASH SLURRY AND THEIR ENVIRONMENTAL IMPLICATIONS

**Simona Elena AVRAM[a], Miuta Rafila FILIP[b,*],
Lucian BARBU TUDORAN[c,d], Gheorghe BORODI[d],
Ioan PETEAN[e,*]**

ABSTRACT. Ferrous particles are usually found in atmospheric particulate matters due to the cars chassis oxidation. These particles are able forming conglomerates with the other mineral particles. Thus, the investigated carwash slurry (CS) reveals a high mineralized composition dominated by Quartz, Calcite and clay minerals with significant amount of iron hydroxides. We found some unusual bigger particles of ferrous conglomerate (FC) into the CS sample. XRD and mineralogical microscopy (MOM) reveal that FC sample is formed by a nanostructured mixture of 56 wt.% Calcite and 44 wt.% Goethite. SEM images and EDS spectra reveal submicron particles within the FC structure with a dense mixture of Ca and Fe. FTIR investigation reveal strong absorption bands for goethite and very weak ones for Lepidocrocite within the FC sample. The results indicates that the conglomerate weas formed on the car chassis rust by wet partial dissolution of calcite that locally forms $Ca(OH)_2$ which further is re-crystallized as calcite due to the CO_2 from the combustion gases. Fine crystallites of iron hydroxides are embedded into the re-crystallized

---

[a] *Faculty of Materials and Environmental Engineering, Technical University of Cluj-Napoca, 103-105 Muncii Bd., RO-400641, Cluj-Napoca, Romania.*

[b] *Raluca Ripan Institute for Research in Chemistry ", Babes-Bolyai University, 30 Fantanele Street, 400294 Cluj-Napoca, Romania.*

[c] *Faculty of Biology and Geology, Babes-Bolyai University, 44 Gheorghe Bilaşcu Street, 400015 Cluj-Napoca, Romania.*

[d] *National Institute for Research and Development of Isotopic and Molecular Technologies, 65-103 Donath Street, 400293 Cluj-Napoca, Romania.*

[e] *Faculty of Chemistry and Chemical Engineering, Babes-Bolyai University, 11 Arany Janos Street, 400028 Cluj-Napoca, Romania.*

[*] *Correspondent authors: miuta.filip@ubbcluj.ro; ioan.petean@ubbcluj.ro*

SIMONA ELENA AVRAM, MIUTA RAFILA FILIP, LUCIAN BARBU TUDORAN,
GHEORGHE BORODI, IOAN PETEAN

calcite. In conclusion, the magnetic selection is recommended for the ferrous conglomerate particles removal from CS to be used as natural coverage for of urban dump sites rehabilitation.

INTRODUCTION

Particulate matter (PM) represents a major environmental concern due to their ability to penetrate into the respiratory system and therefore to affect living beings' health [1, 2]. Particles size is one of the most important parameter regarding particulate matters. Particles with aerodynamic diameter of 10 μm are standardized as PM10; those having 2.5 μm are PM2.5 [3, 4]. New environmental trends try to bring on the standards PM1 class with an aerodynamic diameter of 1 μm and below. Fact is really difficult because the lack on precise quantitative measuring of such finest particles amount [5, 6]. Some of the newest research in the field reveals nanostructural fractions within particulate matter samples [7 - 9].

Carwash slurry collects all kind of PM related to the streets traffic and reflects the particles movements during suspension – sedimentation – re suspension cycles [10, 11]. Thus, a lot of atmospheric suspended particles sediments on the cars surface containing significant amounts of PMs' from PM1 to PM10. These particles have various sources such as: soil erosion [12, 13] generating mostly mineral components and generally associated with street dust [10, 14]; some local anthropogenic industrial activities [15, 16] and finally one of the most important is the circulating vehicles wear implying chassis rust [17, 18] and tires intensive usage [19, 20]. Some research relates ferrous conglomerates presence into the street dust due to the mineral particle's interactions with iron hydroxides on the car chassis rust scale evidencing embedding mainly small micro sized quartz slivers and traces of clays [9, 21].

Present research is focused on some unusual bigger particles of ferrous conglomerate found in carwash slurry resulted from a large facility deserving all kind of road vehicles such as: cars, buses and heavy lorry which circulates on average and long cruises covering the Euro – Region 6 NV in Romania. It implicates mainly sedimentary soils specific to the Transylvanian Basin based on minerals like: Quartz, Calcite, and clays (e.g. Muscovite and Kaolinite) [22, 23]. Large areas within the coverage area are dominated by evaporitic formations such as sodium chloride crystallized as Halite [24 – 25].

We aim to investigate the physicochemical composition and microstructure of these ferrous conglomerate particles and their relation with the carwash slurry and their further environmental implications.

RESULTS AND DISCUSSION

The mineral composition of the samples was investigated by X – ray diffraction (XRD) correlated with mineralogical optical microscopy (MOM) assuring a complete view of the mineral distribution within the samples. The XRD pattern resulted for carwash slurry sample (CS) is presented in Figure 1a. It has a profound crystalline nature dominated by very well-developed peaks with significant intensities and narrow allure. There are also observed some small broadened peaks which may belong to small particles or to some nano-crystalline formations. The dominant mineral is Quartz followed closely by Calcite, Kaolinite and Muscovite. We notice that cumulative clay amount is situated just after Quartz overtaking Calcite position. Some of the clay diffraction peaks are intense and narrow indicating presence of large particles but also some of them are slightly broadened indicating the presence of fine submicron clay particles as well. There were identified relevant peaks for Goethite (e.g. α Iron Hydroxide) and some traces of Lepidocrocite (e.g. γ Iron Hydroxide). Each mineral amount in CS sample was established by Reference Intensity Ratio RIR method measuring relative intensities and minerals corundum factor [26, 27]. The obtained values are centralized in Table 1.
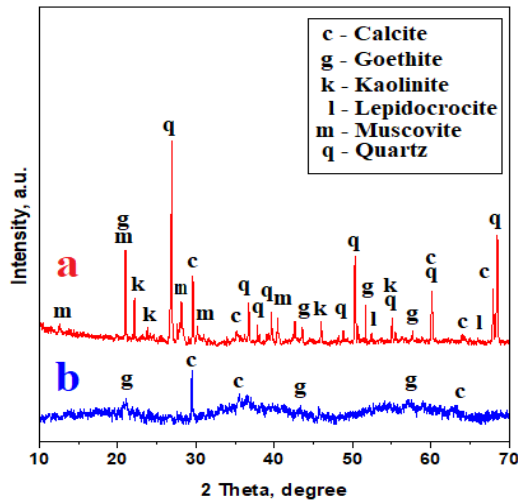
Figure 1. The XRD patterns for: a) carwash slurry and b) ferrous conglomerate.

The ferrous conglomerate sample (FC) presents a XRD pattern with less intense peaks and very broadened due to the presence of nano-crystalline structure, Figure 1b. The dominant mineral is Calcite followed by Goethite indicating a very strange composition. The usual iron conglomerates found in urban street dust related to the cars chassis corrosion are dominated by iron hydroxides mixture (e.g. Goethite and Lepidocrocite) which embeds mainly quartz fine fresh broken particles and clays traces up to 30 wt. % [9, 21]. Now, FC sample has 56 wt.% Calcite and 44 wt.% Goethite according to RIR determination, Table 1. It means that Calcite embeds the Goethite crystals. Therefore, we calculate the crystallite size using Scherrer Formula [7, 10] resulting a mean diameter of 40 nm for Calcite and 60 nm for Goethite. The fact is very strange since the usual ferrous conglomerates related to the street dust are micro-aggregates instead of nanostructured composition.
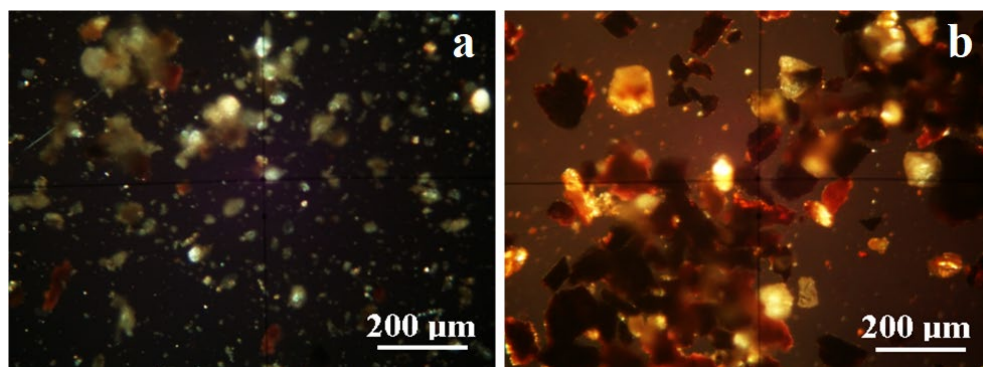
Figure 2. Mineralogical optical microscopy for: a) carwash slurry and b) ferrous conglomerate.

Mineral particles distribution within CS sample is observed in the MOM image in Figure 2a. Each mineral has its own color nuance allowing proper identification and particle size measurement, the obtained data being centralized in Table 1.

Table 1. Samples mineral characteristics

Component	Quartz	Kaolinite	Muscovite	Calcite	Goethite	Lepidocrocite
Formula	SiO_2	$Al_2Si_2O_5(OH)_4$	$Al_2K_2O_6Si$	$CaCO_3$	$\alpha FeO(OH)$	$\gamma FeO(OH)$
Carwash slurry						
Amount, wt.%	29	19	17	25	7	3
Particle size range, µm	5 - 50	5 - 65	1 - 30	1 - 25	5 - 30	5 - 30
Conglomerate						
Amount, wt.%	-	-	-	56	44	-
Particle size range, µm	-	-	-	3 - 100	5 - 100	-
Crystallite size, nm	-	-	-	40	60	-
Color in cross polarized light	Green - gray	White-blue	Pink	Yellow-brown	Reddish - brown	Reddish - brown
Particle shape	round	tabular	tabular	round	elongated	elongated

It results that all identified minerals have bigger particles which are classified as suspended particles (diameters from 10 up to 65 µm). They are accompanied by PM10 fractions which contain mainly Quartz and Calcite as well as few ferrous conglomerate particles (mixture of Goethite and Lepidocrocite traces). The PM2.5 fraction contains mainly clay particles such as Kaolinite and Lepidocrocite. The mineral composition and particle distribution of CS sample reveals that PM originates in the soil erosion in good agreement with literature [12, 13] excepting ferrous particles which rather originate in the cars rust in good agreement with [17, 18]. All observed particles within CS sample have dark spots which belong to the amorphous organic phase that requires FTIR investigation.

On the other side, FC sample, Figure 2b, reveals uneven broken fractions of ferrous conglomerate. The light-yellow particles belong to Calcite that embeds different amount of Goethite (reddish brown). In consequence, come of the particles present red color and the ones with densest embedding of iron hydroxide appear dark brown.

SEM image of CS sample, Figure 3a, reveal a particle distribution similar to the one observed by MOM. Bigger particles (Quartz and Calcite) are surrounded by fine clay particles, fact sustained by the elemental map.
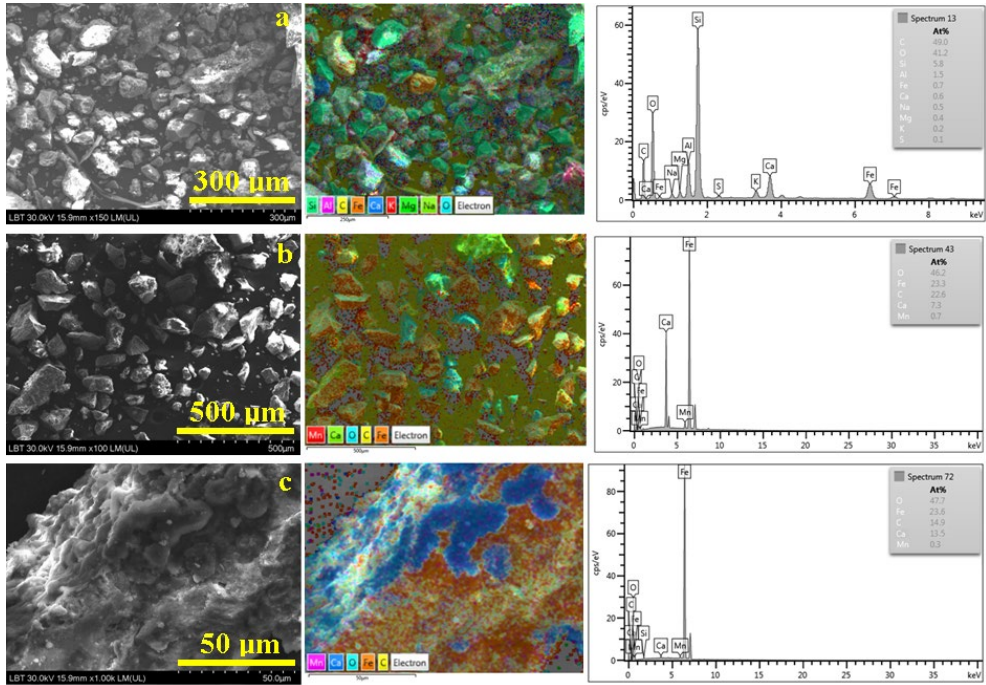
Figure 3. SEM images with elemental maps and EDS spectra for a) carwash slurry, b) ferrous conglomerate and c) details on a single ferrous conglomerate particle.

The elemental map sustains the mineral assignment to the observed particles: Quartz particles appear bright green due to the Si labeled green and O labeled cyan; Calcite particles appear in dark blue nuance because Ca is labeled in dark blue. Fine clay particles are colored in dark red due to the presence of Al, K with small traces of Mg and Na. Particles colored in orange nuance belongs to the ferrous conglomerate because of orange labeling of Fe. The complete elemental composition of the CS sample is given in Table 2. Several yellow stains are observed on the particle surface indicating high concentration of non mineralized carbon that might be related with organic dirt spots identified by MOM. The presence of organic matter is sustained by very high amount of carbon resulted on the elemental composition

of CS sample. Oxygen amount is also high in CS and it is divided between organic matter and mineral oxides and silicates evidenced. The amount of 0.7 at. % Fe is in good agreement with the presence of the rusty particle of about 50 μm diameter in Figure 3a.

Table 2. Samples elemental composition

Samples	Elemental composition, At. %										
	C	O	Si	Al	Fe	Ca	Na	Mg	K	S	Mn
CS	49	41	5.8	1.5	0.7	0.6	0.5	0.4	0.2	0.1	-
FC	22.6	46.2	-	-	23.3	7.3	-	-	-	-	0.7
Single FC particle	14.9	47.7	-	-	23.6	13.5	-	-	-	-	0.3

Figure 3b reveals the SEM aspect of broken particles within FC sample that are in good convergence with MOM observations in Figure 2b. The elemental map labels indicate: orange – Fe; cyan – O; light green Ca and red – Mn. The color combination reveals the yellow-greenish particles of calcite with different embedded amount of Goethite represented by orange spots. Manganese presence as low trace into the elemental composition of FC sample might be related with the lower side of the car corrosion. The overall elemental composition of FC sample is given in Table 2. It is dominated by oxygen carbon and iron, fact in good agreement with the XRD and MOM results. However, it is necessary a closer look at a single FC particle detail for a more precise determination.

High magnification detail of a single FC particle is presented in Figure 3c. Ferrous conglomerate particle evidence growth layers on the left side of the observation field. Corresponding elemental map shows that these layers have blue nuance for Calcite and orange nuance for the embedded Goethite. Oblique position of the FP particle side allows us establish an average thickness of the growth layer of 6.8 μm. The outer most layer aspect is better observed on the central and left side of the observation field in Figure 3c. There are observed rounded clusters of Goethite about 5 – 10 μm in diameter embedded into the nanostructured Calcite mass. Fact is sustained by the small brown-orange dots observed in the elemental map on these specific areas. The elemental composition of the single FC particle reveals large amount of O and Fe corresponding to the Goethite clusters embedded into the calcite. The amount of C and Ca respects the Calcite stoichiometric proportion, fact in very good agreement with XRD observations. Also, low traces of manganese occur, perhaps due to the corrosion of some alloyed steel part.

FC particles growth layer by layer indicates a long-term process that involves Calcite and Goethite. Missing Lepidocrocite is also a strange aspect related to the investigated ferrous conglomerate. A closer look to the chemical bonds within the samples is required. Therefore, FTIR analysis was effectuated for both samples CS and FC, Figure 4.
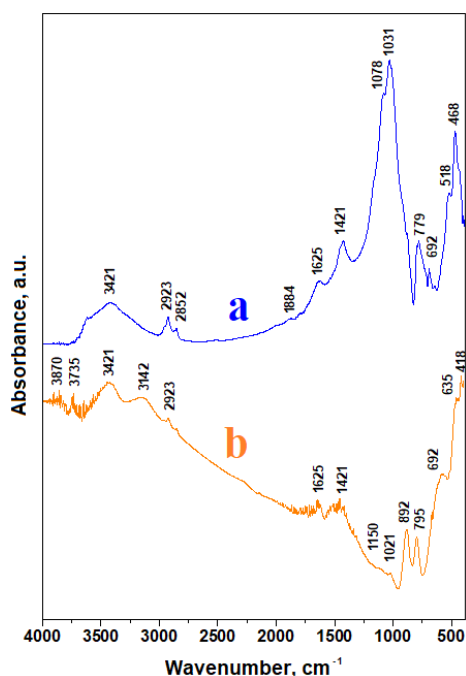
Figure 4. FTIR spectra for a) carwash slurry and b) ferrous conglomerate.

The first absorption bands resulted for CS sample, Figure 4a, belong to the mineral components: 468 cm^{-1} is assigned to Si-O-Si deformation within silicates and clay, 518 cm^{-1} corresponds to Fe-O chemical bond within iron oxides; 692 cm^{-1} belongs to symmetrical deformation of CO_3^{2-} within Calcite, 779 cm^{-1} is assigned to Si-O stretching from Quartz, 1031 cm^{-1} indicates the planar stretching of Si-O within silicates, 1421 cm^{-1} reveals the asymmetric stretch of CO_3^{2-} within Calcite [28, 29]. Water presence is related both to adsorbed water and chemically bonded molecules having absorption bands at: 1625 cm^{-1} for H-O-H rotation and 3421 cm^{-1} for H-O-H stretching [30].

The other group of absorption bands within CS sample is related to the organic matter observed as dark amorphous spots in MOM images and rich carbon dots in SEM elemental maps. We found following bands at: 1078 cm^{-1}

belonging to C-H deformation within CH_3 groups [31]; 1884 cm^{-1} corresponding to symmetric stretch of the saturate C=O bond; 2852 cm^{-1} assigned to symmetric stretch of CH_2 and 2923 cm^{-1} belonging to asymmetric stretch of CH_2 [32, 33]. On the other side these absorption bands are related to the organic nanoparticles resulted from used tires [34, 35] and confirms the initial supposition that amorphous organic matter found in CS samples is mainly formed by tires nanostructural residues. Fact requires further detailed investigation with GC-Ms techniques.

FTIR spectrum resulted for FC sample, Figure 4b, has a totally different allure that CS and evidenced different absorption bands. Some intense absorption bands are observed at 635; 795 and 892 cm^{-1} characteristic for Goethite [36] followed by very weak absorption bands at 1021 and 1150 cm^{-1} are reported for Lepidocrocite [36]. This particularly disposal of the absorption bands confirms the XRD observation that the Calcite prefer embedding of Goethite during the ferrous conglomerate growth due to its more stable structure [37, 38]. Calcite presence is evidenced by the following absorption bands: 692 cm^{-1} related to the symmetric deformation of CO_3^{2-} and 1421 cm^{-1} related to asymmetric stretch of CO_3^{2-} [29].

Water is also present in FC sample through the absorption bands at 1625 cm^{-1} for H-O-H rotation and 3421 cm^{-1} for H-O-H stretching [30] and some organic traces represented by the absorption bands: 2923 cm^{-1} belonging to asymmetric stretch of CH_2 and OH stretching at 3735 cm^{-1} [34, 35]. The presence of significant organic matter traces (induced by the cars used tires) in FC sample suggests that the conglomerate was formed by the street dust back scattered by the used tires in wet conditions that collides the rust scale.

Calcite might be partially dissolute under wet milling conditions induced by the tires and its aqueous solubility might be enhanced by the increased temperatures on the lower side of the cars chassis while Quartz particles are completely insoluble in water and tends to fell away due to impact forces. Furthermore, Calcite has a water solubility of 47 mg/L in the normal environmental condition. It might induce a partial dissolution of street dust calcite particles generating small amount of calcium hydroxide according to the reaction (1)

$$CaCO_3 + H_2O \rightarrow Ca(OH)_2 + CO_2 \qquad (1)$$
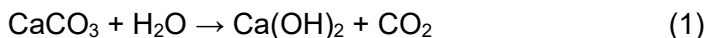
The calcium hydroxide embeds fine particles from rust scale containing iron hydroxides which are mainly Goethite and some traces of Lepidocrocite. The oxygen and hydroxyl anions are assembled in hexagonal crystallographic planes within Goethite assuring a better stability while in Lepidocrocite are arranged in cubic patterns within its orthorhombic lattice making

65

it less stabile. Schwertmann and Taylor in 1972 described the transformation of Lepidocrocite into the Goethite in two steps: first is aqueous dissolution of Lepidocrocite followed by the re-crystallization of iron hydroxide into its more stabile form as Goethite [38]. Lepidocrocite dissolution is described by relation (2),

$$\gamma FeOOH_{(S)} + H_2O \rightarrow \gamma FeOOH_{(l)} \tag{2}$$

$$\gamma FeOOH_{(l)} \rightarrow \alpha FeOOH_{(s)} + H_2O\uparrow \tag{3}$$
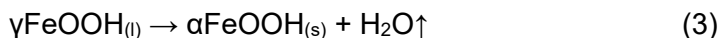
while the Goethite crystallization from solution is described by relation (3). These processes are developed in rich CO_2 atmosphere that facilitates reversing calcium hydroxide into calcite via equation (4):

$$Ca(OH)_2 + CO_2 \rightarrow CaCO_3 + H_2O \tag{4}$$
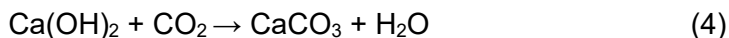
re-crystallization process often found in the caves formations during sedimentary geological formations [39, 40]. When transformation from relations (3) and (4) occurs simultaneously the crystallized Goethite is embedded into the Calcite matrix forming a dense nanostructural pseudo-composite as observed in Figure 3c.

The obtained results are convergent and sustain the unusual composition and microstructure of the identified ferrous conglomerate figuring out some important environmental aspects. Physicochemical conditions required for the conglomerate formation needs large Calcite amounts which is provided by sedimentary soils erosion associated with advanced deforestations of high angle slope hills situated under research coverage area of Romanian Euro Region 6 NV. Auto-vehicles advanced rust of chassis bottom provide enough iron hydroxides for a consistent scale development that progressively interacts with calcite deposits facilitating multi-layered conglomerate development under high temperature that involved at average and long cruise. Tires also facilitate conglomerate deposits by the particularly grooves shape that spread the PM particles over the rusted chassis parts. Advanced wear of the tires also facilitates the emission of pollutant organic nanoparticles [41, 42] that affects both ferrous conglomerate and carwash slurry.

The environmental management regarding such carwash slurries implies two actions ways: the first is related to their proper dumping with care to avoid pollutant emissions and the second way is related to the particulate sources' mitigation strategies. Thus, the slurry dumping requires specialized dumps with consolidated deposited layers to avoid their sliding and with a strict humidity control of the top layers to avoid dust formation.

Hence, most of the minerals identified into the CS sample originate in the eroded soils the slurry might be converted to a stabile soil useful for urban dumps coverage during the conservation process. Some preliminary preparation actions are required: the ferrous conglomerate particles might negatively affect the further soil stability and could be separated by magnetic methods. Such methods were tested in laboratory for ferrous conglomerate removal from urban anti –skid material [43]. The carwash slurry sample free of ferrous rusted particles might be enhanced with humic components to link the finest clay particles into a stabilization network which might be effective at low humidity grades. Such pseudo-soil mixture might sustain some bushes vegetation like Sea Buckthorn (*Hippophae rhamnoides*) and Wild Rose (*Rosa Canina)* or even some trees like Pine (*Pinus Silvestris*) that were successfully used for coal sterile dumps stabilization [44, 45].

The carwash slurry PM mineral sources mitigation would imply major environmental actions such as eroded soils rehabilitation by re-forestation with young trees. Ferrous conglomerate mitigation could be achieved by removing from circulation old and rusted vehicles and by development of a proper anti – corrosive protection for the circulating vehicles to be applied on the lower side of the chassis. The organic particles emissions related to the tires might be mitigated by a proper choosing of the high thermal stability tires perfectly adapted to the geological conditions of the cruise area.

CONCLUSIONS

Carwash slurry has a complex mineralogical composition resulted mostly due to the soil erosion. It is dominated by Quartz followed closely by Calcite and clay minerals (Kaolinite and Muscovite). There are also occur significant amounts of iron hydroxides: mainly Goethite and low traces of Lepidocrocite. The unusual ferrous conglomerate is formed by 56 wt.% Calcite in a nanostructured form having crystallites of about 40 nm that embeds an amount of 44 wt. % Goethite as nano-crystallites with mean diameter of 60 nm.

Carwash slurry might be reutilized as raw material for urban dumps rehabilitation if the ferrous conglomerate particles would be removed via magnetic selection. Also, its amount might be mitigated by proper environmental management including: eroded soil rehabilitation by re-forestation, anticorrosive protection of the lower side of vehicles chassis combined with withdrawing from circulation of old and depreciated cars. Organic matter related to the tire wear emission might be mitigated by a proper choosing of high thermal stability tires adapted on the geological conditions of the cruising areas.

EXPERIMENTAL SECTION

A large carwash slurry sample (CS) was collected from a large washing facility for: cars, buses and heavy lorry deserving a wide coverage area within Romanian Euro Region 6 NV. The facility name and operator is anonymized for economical reasons.

The ferrous conglomerate (FC) sample was separated by sewing form the CS using a 4 mm mesh sieve and mechanical vibration device, followed by a manual selection according to their general brown – rusty aspect. The FC particles were further grinded manually into an agate mortar to obtain the powder necessary for specific analysis.

The X – ray diffraction analysis was effectuated with a Bruker D8 Advance diffractometer (Bruker Company, Germany) using CuK$_{\alpha 1}$ radiation (λ = 1.54056 Å) coupled with a monochromatic filter of Fe 40 µm. The XRD patterns were registered in 2 Theta ranges of 10 – 70 degrees with a speed of 1 degree/minute. The minerals were identified using Match 1.0 software equipped with PDF 3.0 Powder Diffraction Files (Crystal Impact Company, Bonn, Germany).

Mineralogical Optical Microscopy (MOM) was effectuated with a Laboval 2 microscope (Carl Zeiss Jena, Oberocken, Germany) equipped with digital capture Kodak 10 Mpx camera. Quantitative analysis on the optical microphotographs was done using the Image J professional soft as freeware resource from National Institutes of Health USA.

Scanning Electron Microscopy was effectuated with a Hitachi SU8230 SEM (Tokyo, Japan), equipped with an EDX elemental analysis module X-Max 1160 EDS Energy-Dispersive Spectroscopy (Oxford Instruments, U.K.). The investigation was effectuated in high vacuum mode at an electron beam acceleration voltage of 30 kV.

Fourier Transformed Infrared spectroscopy FTIR was effectuated using a JASCO 610 FTIR (Jasco Corporation, Tokyo, Japan) under ambient conditions using the KBr pellet method in the range of 4000 – 400 cm^{-1} at a resolution of 4 cm^{-1} and 100 scans for each spectrum.

REFERENCES

1. S.H. Pradhan, M. Gibb, A.T. Kramer, C.M. Sayes, *Environ. Res.*, **2023,** *231*, 116267.
2. J. Qin, J. Wang, *Environ. Res.*, **2023**, *233*, 116162.
3. V. Iyer, P.C. Ghosh, S. Ganapathy, K.C. Premarajan, *Saf. Health Work*, **2022**, *13*, S204.
4. M. T. Udristioiu, Y. EL Mghouchi, H. Yildizhan, *J Clean. Prod.*, **2023**, *421*, 138496.

5. S. Wu, J. Tao, N. Ma, Y. Kuang, Y. Zhang, Y. He, Y. Sun, W. Xu, J. Hong, L. Xie, Q. Wang, H. Su, Y. Cheng, *Atmos. Environ.*, **2022**, *277*, 119086.
6. H. Cigánková, P. Mikuška, J. Hegrová, J. Krajčovič, Sci. Total Environ., **2021**, *800*, 149502.
7. G. A. Pǎltinean, I. Petean, G. Arghir, D. F. Muntean, L.-D. Boboş, M. Tomoaia-Cotişel, *Part. Sci. Technol.*, **2016**, *34,* 580-585.
8. G. A. Pǎltinean, I. Petean, G. Arghir, D. F. Muntean, M. Tomoaia-Cotişel, *Rev. Chim.*, **2016**, *67 (6)*, 1118-1123.
9. D. F. Muntean, D. Ristoiu, G. Arghir, R. F. Campean, I. Petean, *Carpathian J. Earth Environ. Sci.*, **2012**, *7*, 175-182.
10. M. Rusca, T. Rusu, S. E. Avram, D. Prodan, G.A. Paltinean, M. R. Filip, I. Ciotlaus, P. Pascuta, T.A. Rusu, I. Petean, *Atmosphere*, **2023**, *14*, 862.
11. V. M. Kolesnikova, O. A. Salimgareeva, D. V. Ladonin, V. Y. Vertyankina, A.S. Shelegina, *Atmosphere*, **2023**, *14*, 403.
12. M. Tian, J. Gao, L. Zhang, H. Zhang, C. Feng, X. Jia, *Atmos. Pollut. Res.*, **2021**, *12*, 101108.
13. A. A. Keri, T. Rusu, S. Avram, *Studia UBB. Ambientum*, **2010**, *55*, 43-53.
14. A. Ghosh, P. K. Nagar, B. Singh, M. Sharma, D. Singh, *Sci. Total Environ.*, **2023**, *904*, 167363.
15. S. Nicoara, L. Tonidandel, P. Traldi, S. Avram, O. Popa, N. Palibroda, *Studia UBB. Ambientum*, **2008**, *2,* 186-192.
16. A. A. Keri, S. Avram, T. Rusu, *ProEnvironment*, **2010**, *3*, 318-321.
17. M. Kadowaki, H. Katayama, *Corrosion Science*, **2023**, 222, 111379.
18. M. S. Sulaiman, D.A. Wahab, Z. Harun, H. Hishamuddin, N. K. Khamis, M. R. Abu Mansor, *Energy Rep.*, **2023**, *9*, 235-246.
19. R. S. Cheong, E. Roubeau Dumont, P. E. Thomson, D. C. Castañeda-Cortés, L. M. Hernandez, X. Gao, J. Zheng, A. Baesu, J. R. Macairan, A. J. Smith, H. N. N. Bui, H.C.E. Larsson, S. Ghoshal, S. Bayen, V. S. Langlois, S.A. Robinson, N. Tufenkji, *J. Hazard. Mat. Adv.*, **2023**, *12*, 100357.
20. I. Gehrke, S. Schläfle, R. Bertling, M. Öz, K. Gregory, *Sci. Total Environ.*, **2023**, *904*, 166537.
21. D.F. Muntean, I. Ivan, L. Muresan, *Studia UBB Chemia*, **2015**, *60*, 207-218.
22. C. Krézsek, A.W. Bally, *Mar. Pet. Geol.*, **2006**, *23*, 405-442.
23. R. S. Huismans, G. Bertotti, D. Ciulavu, C. A. E. Sanders, S. Cloetingh, C. Dinu, *Tectonophysics*, **1997**, *272*, 249-268.
24. L. Rus, S. E. Avram, V. Micle, *Studia UBB Chemia*, **2020**, *65*, 257-268.
25. S. E. Avram, L. Rus, V. Micle, S. S. Hola, *Water*, **2022**, *14*, 2366.
26. I. Petean, G. A. Paltinean, E. Pripon, G. Borodi, L. Barbu Tudoran, *Materials*, **2022**, *15*, 7514.
27. I. Petean, G. A. Paltinean, A. C. Taut, S. E. Avram, E. Pripon, L. Barbu Tudoran, G. Borodi, *Materials*, **2023**,*16*, 5809.
28. M. Lettieri, *Vib. Spectros.*, **2015**, *76*, 48-54.
29. K. Koupadi, S.C. Boyatzis, M. Roumpou, N. Kalogeropoulos, D. Kotzamani, *Heritage*, **2021**, *4,* 3611.
30. J. Bora, P. Deka, P. Bhuyan, K. P. Sarma, R. R. Hoque, *SN Appl. Sci.*, **2021**, *3,*137.

31. A. M. Udrea, A. Dinache, J. M. Pagès, R.A. Pirvulescu, *Molecules*, **2021**, 26, 2374.

32. X. Liu, S. M. Colman, E. T. Brown, E.C., Minor, H. Li*, J. Paleolimnol*, **2013**, *50*, 387-398.

33. F. Usman, B. Zeb, K. Alam, Z. Huang, A. Shah, I. Ahmad, S. Ullah, *Atmosphere*, **2022**, *13*, 124.

34. G. Sarkissian, J. Keegan, E. Du Pasquier, J. P. Depriester, P. Rousselot, *J. Can. Soc. Forensic Sci.*, **2004**, *37*, 19-37.

35. Z. Wang, M. Wu, G. Chen, M. Zhang, T. Sun, K. G. Burra, S. Guo, Y. Chen, S. Yang, Z. Li, T. Lei, A. K. Gupta, *Fuel*, **2023**, *337*, 127206.

36. H. Ciu, W. Ren, P. Lin, Y. Liu, *J. Experim. Nanosci.*, **2013**, *8*, 869-875.

37. Y. Cudennec, A. Lecerf*, Solid State Sci.*, **2005**, 7, 520.

38. U. Schwertmann, R. M. Taylor, *Clays Clay Miner.*, **1972**, *20*, 151-164.

39. O. T. Moldovan, S. Bercea, R. Năstase-Bucur, S. Constantin, M. Kenesz, I. C. Mirea, A. Petculescu, M. Robu, R. A. Arghir, *Tour. Manag.*, **2020**, *78*, 104037.

40. C. Spötl, G. Koltai, Y. Dublyansky, *Chem. Geol.*, **2023**, *638*, 121712.

41. S. H. Woo, H. Jang, S. H. Mun, Y. Lim, S. Lee, *Sci. Total Environ.*, **2022**, *838*, 156548.

42. E. Roubeau Dumont, X. Gao, J. Zheng, J. Macairan, L. M. Hernandez, A. Baesu, S. Bayen, S. A. Robinson, S. Ghoshal, N. Tufenkji, *J. Hazard. Mat.*, **2023**, *453*, 131402.

43. G. Arghir, I. Petean, D. F. Muntean, L. Muresan, C. Suciu, *Powder Metall. Prog.*, **2011**, *11,* 340-346.

44. A. Braşovan, V. Codrea, G. Arghir, R. F. Câmpean, I. Petean, *Carpathian J. Earth Environ. Sci.*, **2011**, *6*, 221-228.

45. A. Braşovan, R. F. Burtescu, N. K Olah, I. Petean, V. Codrea, A. Burtescu, *Studia UBB Chemia*, **2017**, *62(2)*, 81-93.

COMPREHENSIVE ANALYSIS ON *COTINUS COGGYGRIA* SCOP. LEAVES: PHYTOCHEMICAL CHARACTERIZATION, BIOLOGICAL PROFILE AND DOCKING STUDIES

Gökçe ŞEKER KARATOPRAK[a,*], Gökçen KILIÇ[a], İsmail ÇELIK[b], Selen İLGÜN[c], Esra KÖNGÜL ŞAFAK[a], Müberra KOŞAR[d]

ABSTRACT. The present work aims to evaluate the antioxidant, cytotoxic, enzyme inhibitory, and anti-inflammatory properties of *Cotinus coggygria* Scop. The leaf extract was analyzed using LC-MS/MS and antioxidant activity was also investigated via several *in vitro* models (DPPH•, ABTS•+, FRAP, metal chelating, inhibition of *β*-carotene bleaching, and lipid peroxidation). Enzyme inhibition activity was evaluated on *alpha*-amylase and *alpha*-glucosidase. Molecular docking studies were performed to assess the binding efficiency of the identified compounds with *alpha*-glucosidase. The toxicity of the extract was studied using two breast cancer cell lines as well as healthy fibroblast cell lines (L929). Using LPS induced macrophage cell line model, the anti-inflammatory activity was examined by determining NO, IL-1β, IL-6, IL-10, and TNF-*α* levels. The methanol extract significantly affected the *alpha*-glucosidase enzyme, which also exhibited antioxidant activity. Galloyl hexose and methyl trigallate were found to have the highest binding contact energies for the *alpha*-glucosidase enzyme, according to docking analyses. Even at a 31.25 μg/mL concentration, the extract caused 43.46% inhibition in MDA-MB 231, and 48.09% in MCF-7 cell lines. Significant effects on TNF-*α* and IL-6 cytokine levels also proved anti-inflammatory activity. These findings suggest that *C. coggygria* may serve as an efficient *alpha*-glucosidase inhibitor and anti-inflammatory agent.

Keywords: *Cotinus coggygria, enzyme inhibition, docking, anti-inflammatory, antioxidant, cytotoxicity*

a   *Department of Pharmacognosy, Faculty of Pharmacy, Erciyes University, 38039 Kayseri, Turkiye*
b   *Department of Pharmaceutical Chemistry, Faculty of Pharmacy, Erciyes University, 38039 Kayseri, Turkiye*
c   *Department of Pharmaceutical Botany, Faculty of Pharmacy, Erciyes University, 38039 Kayseri, Turkiye*
d   *Faculty of Pharmacy, Eastern Mediterranean University, 99628, Famagusta, North Cyprus, via Mersin-10, Turkiye*
*   *Corresponding author: gskaratoprak@erciyes.edu.tr*

INTRODUCTION

Recently, there has been intense interest in the treatment with herbal medicines in the world in general. Scientists' desire to find drugs with lower side effects due to the possible risks of synthetic drugs has accelerated the studies [1]. In addition, to benefit from the synergistic effects of the chemical structures in its content and to increase the effect, they focus on many herbs and herbal mixtures used in the treatment of diseases among people rather than a single molecule [2]. Many remedies, both written and verbally passed down from generation to generation, have served as crucial guides for scientists conducting such research. In light of this information, studies to determine the preparation and application methods of many plants as medicines, scientifically prove their effects, and identify the components responsible for the effect have gained significant traction [3].

The number of plant species in Turkiye; is around 12.000, including 3000 of them endemic species [4]. Because of Turkiye's strategic location as the union of Eastern and Western cultures, there has been a significant advancement in knowledge of folk remedies [5]. *Cotinus coggygria* Scop., a member of the Anacardiaceae family known as the "Smoke tree", grown in Turkiye, is known to be widely used in oral wound healing among the public [6]. In the literature studies conducted on the *C. coggygria* plant, it has been observed that it has a wound-healing effect on the skin [7,8]. It is known that the plant's leaves and flowers are ground into a paste and used as a blood purifier for skin diseases in Pakistan and as an antiseptic, anti-inflammatory, and anti-hemorrhagic in Serbian traditional medicine [9,10]. In Turkish folk remedies, a decoction of *C. coggygria* leaves is used to treat diabetes [11]. Various studies have been conducted on *C. coggygria* and these usage patterns have been scientifically proven. The plant's antioxidant, antibacterial, antifungal, antiviral, cytotoxic, antigenotoxic, hepatoprotective, and anti-inflammatory effects have been observed [6, 12]. The presence of tannins and various flavonoids was determined by the chemical composition analysis of the plant [13]. It has been reported that the essential oil obtained from the hydrodistillation of leaves collected from young shoots of *C. coggygria* is rich in monoterpenic hydrocarbons [14].

The purpose of this work was to assess the phytochemical and biological capabilities of *C. coggygria* methanol extract. The phytochemical profile of the plant was established through High-performance liquid chromatography-mass spectrometry (LC-MS/MS) profiling and total bioactive ingredients. Compared with previous studies, the antioxidant capacity of the extract was determined using various in vitro bioassays (DPPH•, ABTS•+, FRAP, *β*-carotene-linoleic acid co-oxidation assay, iron-(II) chelate formation and preventing peroxidation

of the phospholipids) and inhibitory properties against enzymes involved in diabetes pathology, including *alpha*-amylase and *alpha*-glucosidase. Its effects on the *alpha*-glucosidase enzyme were detailed by molecular docking analysis. Its toxicity was investigated using breast cancer cell lines (MDA-MB 231 and MCF-7) as well as healthy fibroblast cell lines (L929). Furthermore, the extract's anti-inflammatory efficacy was assessed by measuring nitric oxide (NO), interleukin-1 *beta* (IL-1β), interleukin-6 (IL-6), interleukin-10 (IL-10), and tumor necrosis factor-*alpha* (TNF-*α*) levels in the lipopolysaccharide (LPS)-induced RAW 264.7 cell line. This study was the first to explore in-depth biological activity evaluation using *C. coggygria* in light of its traditional uses.

RESULTS AND DISCUSSION

Composition Analysis

Total phenol, flavonoid, and flavonol levels were measured spectrophotometrically to identify the secondary metabolite composition of the extract in phenolic structure using the methods presented in the experimental section (Table 1). When the TPC of the plant gathered in Turkiye is compared to the TPC of the species collected in Kosovo and Bulgaria, it is discovered that the TPC of the species collected in Kosovo and Bulgaria is lower, 62.50 ± 2.55 mg/g$_{extract}$ and 114.73 ± 1.14 mg/g$_{extract}$, respectively [15]. The total flavonoid and flavonol content of the plant also contributes to the richness of its chemical composition.

Table 1. Extract yield, total phenolic content, flavonoid,
and flavonols of *C. coggygria*

Extract	Yield [%]	Total Phenol [mg$_{GAE}$/g$_{extract}$]	Total Flavonoid [mg$_{CA}$/g$_{extract}$]	Total Flavonol [mg$_{RE}$/g$_{extract}$]
C. coggygria	19.42	208.07 ± 0.98	85.73± 2.15	49.82 ± 3.01

Values are the mean ± SD (n = 3).

Based on the formation of molecular ion peaks and base peaks, secondary metabolites present in 70% methanol extract were evaluated using the LC-MS/MS system. Table 2 lists the compounds found in the extract. Gallic acid, methyl gallate, quinic acid, galloyl hexose, methyl digallate, quercetin rhamnoside, myricetin rhamnoside, methyl trigallate, and pentagalloyl hexoside were all detected in the LC/MS/MS studies. In the literature, it has been

determined that *C. coggygria* is rich in tannins, as well as essential oil and various flavonoid content [13]. In an analysis of the plant's chemical composition; gallic acid and its derivatives such as methylgallate, methyl ester of gallic acid, and pentagalloyl glucose (pentahydroxy gallic acid and pentagalloyl glucose, which is the glucose ester) were found [8]. In the analysis made by HPLC; compounds such as sulfuretin, fisetin, and fustin have been identified [13]. Other flavonoid compounds are: disulfuretin, sulfurein, taxifolin, 4'7-dihydroxyflavanonol, liquiritigenin, biauron, myricetin, kaempferol, quercetin, 4',5,7-trihydroxy flavanone, and isoliquiritigenin [16].

Table 2. LC-MS/MS analysis of compounds in the *C. coggygria* leaf extract

MA	[M-H] m/z	Compounds	% amount*	Ref.
170	169, 125	Gallic acid	< 1	[17]
184	183, 124	Methyl gallate	29.51	[17]
192	191, 173	Quinic acid	9.27	[17]
332	331, 191, 169	Galloyl hexose	1.63	[18]
336	335, 183	Methyl digallate	24.80	[18]
448	447, 301	Quercetin rhamnoside	< 1	[17]
464	463, 316	Myrcetin rhamnoside	3.51	[17]
470	469, 183	Methyl trigallate	4.69	[18]
940	939, 787, 617, 469	Pentagalloyl hexoside	2.13	[17]

* Percentages are relative values in the total ion spectrum obtained by LC-MS/MS;
 MA: molecular weight.

Antioxidant Activity

FRAP assay

The extract's ability to reduce iron (III) was not as efficient as the positive controls, which included AA, BHT, BHA, RA, and GA. The reduction power of the extract was found to be significantly lower ($p<0.001$) compared to other standards (Table 3). The extract's ability to convert iron(III) to iron(II) is considered hydrogen donor capacity and is very crucial in the initial phase of radical chain reactions [19]. As stated in Simić et al. (2008), the ethyl acetate fraction of acetone extract displayed significant ferric-reducing ability with a 5.0 mmol Fe^{2+}/g extract value [20]. Similarly, in another study, the reducing ability of the acetone extract's ethyl acetate fraction was reported as 10.7 mmol Fe^{2+} /g extract [12]. The reason for not making a direct comparison with the data obtained from the study is calculating the results as equivalent to ascorbic acid (AscAE).

DPPH$^\bullet$ (1,1-diphenyl-2-picrylhydrazyl) scavenging effect

In the experimental environment studied at physiological pH, the extract was studied at different concentrations and the percentage of inhibition against DPPH radical increased as the concentration increased. However, it was shown that the extract's scavenging ability was inferior to that of the positive controls used, which included AA, BHT, BHA, GA, and RA, it was significantly lower ($p<0.001$). Methanol extracts of *C. coggygria* prepared from leaves and flowers have high antioxidant activity when tested with DPPH$^\bullet$ according to Savikin et al. (2009) [21]. According to the results, the IC_{50} value of the flower extract is 2.6 µg/mL and the leaves extract IC_{50} value is 3.8 µg/mL. In another study, DPPH$^\bullet$ scavenging properties were identified for acetone extract and its fractions including chloroform, ethyl acetate, and water. Acetone extract had a more noticeable impact than AA and a comparable result to GA. In comparison to AA and GA, the ethyl acetate fraction had higher DPPH$^\bullet$ quenching capacity [12].

ABTS$^{\bullet+}$ (2,2'-azino-bis (3-ethylbenzathiazoline-6- sulfonic acid) scavenging effect

It was observed that AA, BHT, BHA, and GA were more potent than the extract in scavenging the radical and even the extract had a statistically less ($p<0.001$) effect than them (Table 3). It was found to be slightly higher than rosmarinic acid at a low concentration (0.1 mg/mL). Sukhikh et al.(2021) determined the TEAC value of *C. coggygria* ethanol extract against ABTS$^{\bullet+}$ and it was reported as 0.46 ± 0.02 mM Trolox equivalent/g fresh mass [22]. The scavenging ability of 0.5 mL essential oil of the *C. coggygria* was also found to be 55.43 ± 0.4 in the research of Shagun et al. (2016) [23]. The plant's capacity to scavenge radicals was proven by the data gathered from several studies.

β-carotene / linoleic acid co-oxidation inhibitory effect

One of the most popular techniques for assessing the level of oxidation of unsaturated fatty acids in food and cell walls is the *β*-carotene/ linoleic acid bleaching test. Results were given as Antioxidant activity coefficient (AAC) in Table 3. The plant's 70% methanol extract showed higher activity than gallic acid and lower activity than synthetic oxidants such as BHA and BHT ($p<0.001$). The *β-*carotene bleaching potential of the plant extract has not been measured before but in the study conducted with its essential oil, it was stated that the oil has the capacity to inhibit bleaching by $56.4 \pm 1.88\%$ [24].

Ascorbate-Fe (III) -catalyzed phospholipid peroxidation inhibition

Biologically significant molecules called phospholipids that are high in polyunsaturated fatty acids are vulnerable to hydroxyl radical ($\cdot$OH) destruction. The principle of the experiment is based on measuring the $\cdot$OH sweeping effect by inhibiting the formation of TBA-reactive compounds after the catalysis of phospholipid liposomes prepared from the bovine brain with ascorbate-Fe(III) at physiological pH [25]. A study examining the effects of methanol extracts made from the plant's flowers and leaves on lipid peroxidation expressed the IC_{50} values as 31.9 ± 5.1 µg/mL and 35.8±3.9 µg/mL, respectively [19]. Our result was found to be compatible with the literature with a value of 0.09 ± 0.01 mg/mL (Table 3).

Table 3. Antioxidant activity results of *C. coggygria* and standards

Samples	GA	AA	BHA	BHT	RA	*C. coggygria*	p
Reduction Power (FRAP)							
AscAE(mmol/g)	4.08±0.13*	5.72±0.10*	1.93±0.06*	2.26±0.05*	3.10±0.03*	0.85±0.01	<0.001
DPPH Radical Scavenging							
IC_{50} (mg/mL)	0.02±0.01*	0.13±0.01*	0.12±0.01*	0.07±0.01*	0.02±0.01*	0.19±0.01	<0.001
ABTS Radical Scavenging							
0.1 mg/mL	2.09±0.02*	1.18±0.01*	0.86±0.01*	0.55±0.01*	0.37±0.01*	0.50±0.03	<0.001
0.2 mg/mL	2.49±0.01*	1.91±0.01*	1.87±0.01*	1.45±0.01*	1.32±0.01*	1.04±0.01	<0.001
***β*-carotene Bleaching**							
AAC	639.13±0.88*	--	987.55±1.33*	933.23±1.25*	661.42±1.10*	813.59±4.06	<0.001
Ascorbate-Fe (III) -catalyzed Phospholipid Peroxidation Inhibition							
IC_{50} (mg/mL)	0.16±0.06	0.90±1.29*	0.02±0.01	0.09±0.01	0.19±0.23	0.09±0.01	<0.001

*Indicates the difference with *C. coggygria* extract for the respective row. Values are the mean ± SD (n = 3), data is given as mean values with ± 95% confidence interval.

The ferrous ion chelating activity

Iron chelating action is dependent on the quantitative production of complexes of Ferrozine with Fe^{+2}. The ferrozine reagent, a potent chelator, competes with metal-binding chemicals in the environment to bind Fe^{+2} ions. The development of the Fe^{+2}/ferrozine complex is avoided by strong chelating power. Divalent transition metal ions play a crucial part in hydroperoxide decomposition reactions for instance catalyzing the oxidative process, formation

of hydroxyl radicals, and Fenton chemistry. These reactions can be terminated by chelation and deactivation of iron [26]. The extract had an activity of greater than 10 mg/mL, according to research on the extract's effect on the chelation of iron (II). Nićiforović et al. (2010), discovered that the *C. coggygria* methanol extract has a metal chelating capability of more than 10 mg/mL, which is consistent with our findings [27]. The low metal chelating capacity may be associated with the low flavonol content of the plant.

Cytotoxic activity

The extract was evaluated for its toxic effects against various breast cancer lines including MDA- MB 231 and MCF-7, as well as healthy mouse fibroblast cells (L929), and the results are given in Figure 1. Significant cytotoxicity ($p < 0.001$) of the extract was observed against all three cell lines at the highest concentration applied, 2000 μg/mL. Given the vast distribution in the human body, it is naturally very difficult to obtain this concentration, where the highest effect is observed. While there was no significant decrease in L929 cell viability at 31.25 μg/mL concentration, MDA-MB 231 and MCF-7 cell viability were found to be 56.53% and 51.9%, respectively ($p < 0.05$).
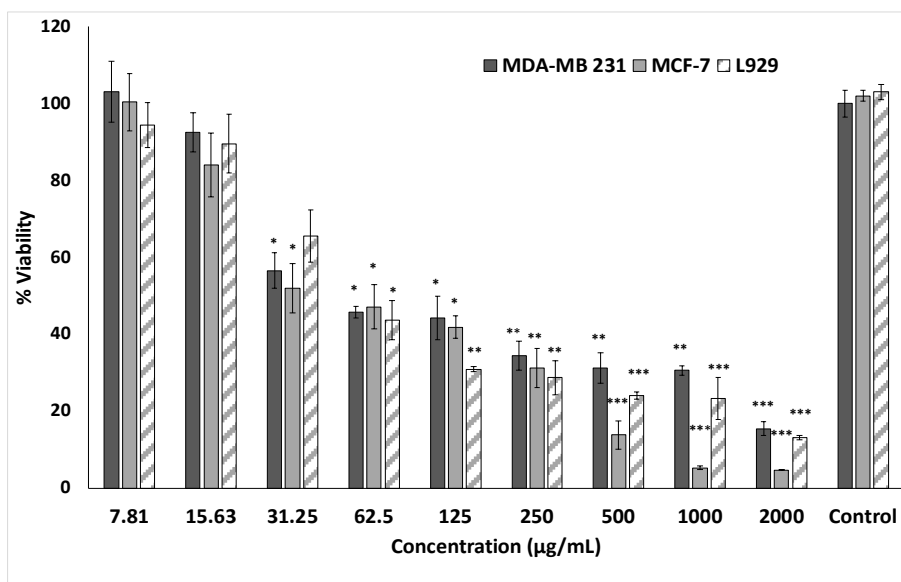
Figure 1. Cytotoxic activity on MDA-MB231, MCF-, and L929 cell lines.
Each value presented as mean ± SD (n = 3), * indicate $p < 0.05$;
** indicate $p < 0.01$; *** indicate $p < 0.001$ (Dunnet test).

However, at lower doses, the extract had no discernible effects on viability (Figure 1). In a recent study, it has been proven that *C. coggygria* ethanol extract causes apoptosis and S-phase cell cycle arrest in MCF-7 cells, inhibits colony formation, causes DNA damage, and changes cellular thermodynamic parameters [28]. Another investigation found that the *C. coggygria* ethyl acetate extract had an IC_{50} value of 67.63±3.67 µg/mL in the triple-negative breast cancer line (MDA-MB 231), and these data were found to be congruent with our findings [29].

Enzyme inhibitory-docking analysis

At 1 mg/mL concentration, *C. coggygria* methanol extract had no impact on the *α*-amylase enzyme. The extract demonstrated a noticeable inhibitory impact on the *α*-glucosidase enzyme (Figure 2). In the concentration range of 7.81-1000 µg/mL, inhibition was found to be the same as acarbose (p>0.05). At 1.95 and 3.91 µg/mL concentrations, the percentage of inhibition was found to be 13.92% and 63.55%, respectively. According to a study by Özbek et al. (2019), it was stated that the ethyl acetate fraction, in which *C. coggygria* did not show any effect against *α*-amylase, exhibited an IC_{50} value of 8.2 µg/mL in inhibition of the α-glucosidase enzyme [11]. The fact that *C. coggygria* is used in the treatment of diabetes among the public has been confirmed by the results of the experiments. Therefore, to understand which compounds exert this effect, docking analysis was put forward for the first time with this study.
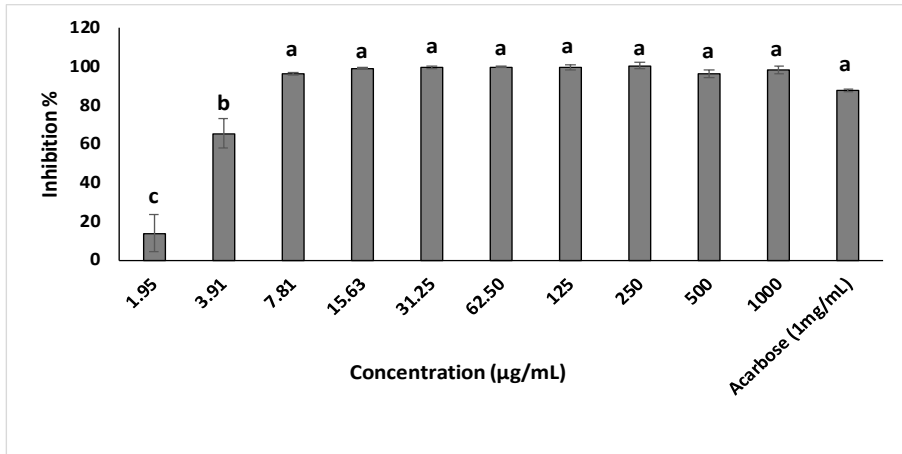
Figure 2. Inhibition effect of *C. coggygria* on α-glucosidase enzyme. Results were expressed as the mean of triplicates ± SD (n = 3).[a-c] identical lowercase letters indicate statistical differences (p > 0.05).

Utilizing molecular docking studies to predict the activity state of natural compounds on macromolecules such as enzymes, proteins, and RNA is a rational approach for drug research [30]. Molecular docking analyzes were undertaken to assess the interactions of the compounds obtained from *C. coggygria* by LC-MS/MS analysis on the *alpha*-glucosidase enzyme. Compounds and standard substance acarbose were docked with Glide SP. As given in Table 4, the docking interaction energy of the compounds was between -8.238 and -4.154, while acarbose formed -4.508 kcal/mol interaction energy. *Alpha*-glucosidase and protein-ligand interactions of all compounds were analyzed for H bond, hydrophobic, π-π stacked, polar, negatively charged, and positively charged interaction patterns. The binding poses and schematic protein-ligand interaction diagrams of galloyl hexose and methyl trigallate compounds with the highest docking interaction energy are given in Figure 3. Galloyl hexose formed nine H bonds with active site residues Asp68 (1.90 Å), His111 (Å), Gln181 (2.75 Å), Asn241 (1.66 and 1.95 Å) Glu276 (1.87 Å), Asp349 (1.78 and 2.13 Å) and Arg439 (2.03 Å). Methyl trigallate, on the other hand, formed four H bonds with residuals Asn241 (1.62Å), Ser308 (2.20 Å), and Asp349 (1.49 and 1.65 Å), and π-π stacking interactions with Phe157 (4.25 Å). The standard compound acarbose formed two H bonds with Glu304 (1.92 Å) and Ser308 (2.26 Å). The number and length of the H bond can provide information about the interaction of a compound with the target enzyme. Galloyl hexose followed by methyl trigallate formed highly potent interactions. Detailed protein-ligand interaction types and energies of other compounds gallic acid, quinic acid, quercetin 3-*O*-rhamnoside, methyl gallate, digallic acid methyl, and myricetin 3-rhamnoside are given in Table 4.
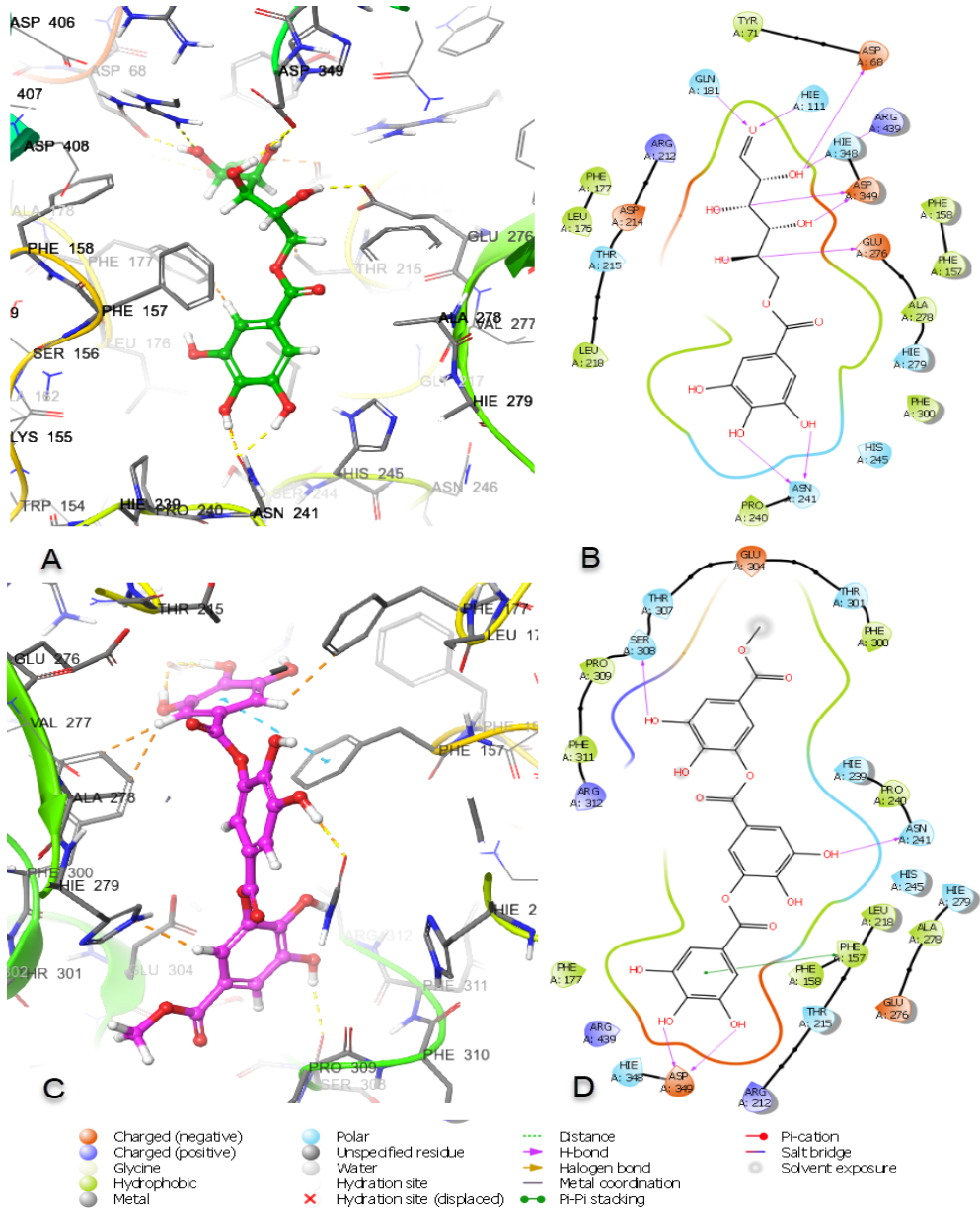
Figure 3. Glide SP molecular docking results of compounds galloyl hexose and methyl trigallate with alpha-glucosidase. (A) Binding pose and, (B) schematic interaction diagram of galloyl hexose (C) 3D interaction, and (D) 2D protein-ligand interaction of methyl trigallate in the *alpha*-glucosidase active site.

Table 4. Protein-ligand interaction energies (kcal/mol) and interaction types obtained from molecular docking study against *alpha*-glucosidase enzyme of compounds identified by LC-MS/MS analysis from *C. coggygria*

Compounds (PubChem ID)	Docking Scores		Protein-ligand interaction types					
	glide gscore	glide emodel	H bond	Hydrophobic	π-π stacked	Polar	Negative Charged	Positive Charged
Galloyl hexose (128839)	-8.2	-81.9	Asp68 (1.90 Å), His111 (Å), Gln181 (2.75 Å), Asn241 (1.66 and 1.95 Å) Glu276 (1.87 Å), Asp349 (1.78 and 2.13 Å), Arg439 (2.03 Å)	Tyr71, Phe157, Phe158, Leu176, Phe177, Leu218, Pro240, Ala278, Phe300	NI	His111, Gln181, Thr215, Asn241, His245, His348	Asp68, Asp214, Glu276, Asp349	Arg212, Arg439
Methyl trigallate (156096784)	-7.1	-67.7	Asn241 (1.62Å), Ser308 (2.20 Å), Asp349 (1.49 and 1.65 Å)	Phe157, Phe158, Leu176, Phe177, Leu218, Pro240, Ala278, Phe300, Pro309, Phe311	Phe157 (4.25 Å)	Thr215, His239, Asn241, His245, His279, Thr301, Thr307, Ser308, His348,	Glu276, Glu304, Asp349,	Arg212, Arg312, Arg439
Gallic acid (370)	-5.1	-39.3	Lys155 (2.01 and 2.32 Å), Phe157 (2.01 Å), His239 (2.14 Å), Glu304 (1.73 Å)	Phe157, Pro240, phe300	Phe157 (4.09 Å)	His239, asn241, his279, asn412	Glu304	Lys155, arg312
Quinic acid (6508)	-5.1	-43.2	Asp214 (1.65 and 1.87 Å), Asp349 (1.93 Å),	Tyr71, Val108, Phe157, Phe158, Leu176, Phe177, Phe300	NI	His111, Gln181, Thr215, His348	Asp68, Asp214, Glu276, Asp349	Arg212, Arg312, Arg439
Quercetin 3-O-rhamnoside (5353915)	-4.5	-43.2	Ser308 (2.60 Å), Pro309 (1.86 Å)	Phe157, Phe177, Leu218, Ala278, Phe300, Pro309, Phe310	His279 (1.93 Å)	Thr215, His239, Asn241, His245, His279, Thr307, Ser308	Glu304	NI
Methyl gallate (7428)	-4.4	-30.5	Asp68 (1.69 Å), Asp214 (1.78 Å)	Tyr71, Val108, Phe157, Phe158, Phe177, Phe300	NI	His111, Gln181, Thr215, His348, Gln350	Asp68, Asp214, Glu276, Asp349	Arg439, Arg443
Digallic acid methyl 10131824	-4.3	-40.1	Asn241 (2.31 Å), Glu276 (2.53 Å)	Phe157, Phe158, Phe177, Ala278, Phe300, Tyr313	NI	Thr215, Asn241, His245, His279, Gln350		Arg312, Arg439
Myricetin 3-rhamnoside (5352000)	-4.2	-46.9	Glu304 (1.98 Å), Pro309 (2.78 Å)	Phe157, Leu218, Ala278, Phe300, Pro309, Phe300	Hie279 (4.91 Å)	Asn241, His245, Hie279, Thr301	Glu304	NI
Acarbose (41774)	-4.5	-26.5	Glu304 (1.92 Å), Ser308 (2.26 Å)	Phe157, Phe158, Phe177, Leu218, Pro240, Ala278, Phe300, Pro309, Phe311	NI	Thr215, Hie239, Asn241, His245, Hie279, Thr307, Ser308, Hie348, Gln350	Asp214, Glu276, Glu304, Asp349	Arg212, Arg312, Arg439

Anti-inflammatory activity

To determine the non-toxic dose before the anti-inflammatory activity study, toxicity tests were performed on the macrophage cell line by the MTT method. Concentrations that did not reduce viability were determined as 31.25 and 62.5 µg/mL (Figure 4 A).

Inflammation is increased and maintained by pro-inflammatory cytokines, which are primarily produced by activated macrophages in the regulation of inflammatory responses. These are IL-1β, IL-6, and TNF-α common proinflammatory cytokines [31]. Human cytokine synthesis inhibitory factor (IL-10) is a cytokine that reduces inflammation [32]. NO is a temporary free radical formed by the reaction of the nitrogen atom in the guanido group of the arginine amino acid with molecular oxygen [33]. The results of the extract's anti-inflammatory effect are shown in Figure 4.

There was an increase in nitric oxide levels in the LPS-treated control well in comparison to the untreated control. The NO amount considerably ($p<0.001$) elevated in the LPS group. In the co-treatment and pre-treatment groups to which the extract was applied, both concentrations caused a significant reduction ($p<0.05$). 62.5 µg/mL concentrated extract decreased the NO amount from 70.36 µM to 25.56 µM in the pre-treatment group (Figure 4B).

In the study, IL-1β, one of the pro-inflammatory cytokines, showed a noticeable boost in the LPS group as opposed to the untreated control group ($p<0.05$). In the pre-treatment group, 62.5 µg/mL concentration of the extract exhibited a substantial decrease in the quantity of IL-1β compared to the LPS group, and the amount of IL-1β was found to be 143.03 pg/mL (Figure 4C). There was no discernible distinction in the amounts of IL-1β in either concentration in the co-treatment group as compared to the values in the LPS group.

It is worth mentioning that IL-6 is another pro-inflammatory cytokine and is associated with the regulation of immune responses. Therefore, the reduction of its levels could be an indication of the extract's potential for inflammation. There was an increase in the amount of IL-6 in LPS-inflamed wells compared to non-inflamed control wells. The results showed that the co-treated group's IL-6 level dropped to 113.30 pg/mL at a dose of 62.5 µg/mL and was statistically equivalent to the untreated control group ($p>0.05$). No discernible effect on inflammation was noticed in the pretreatment group at 31.25 µg/mL concentration (Figure 4D).
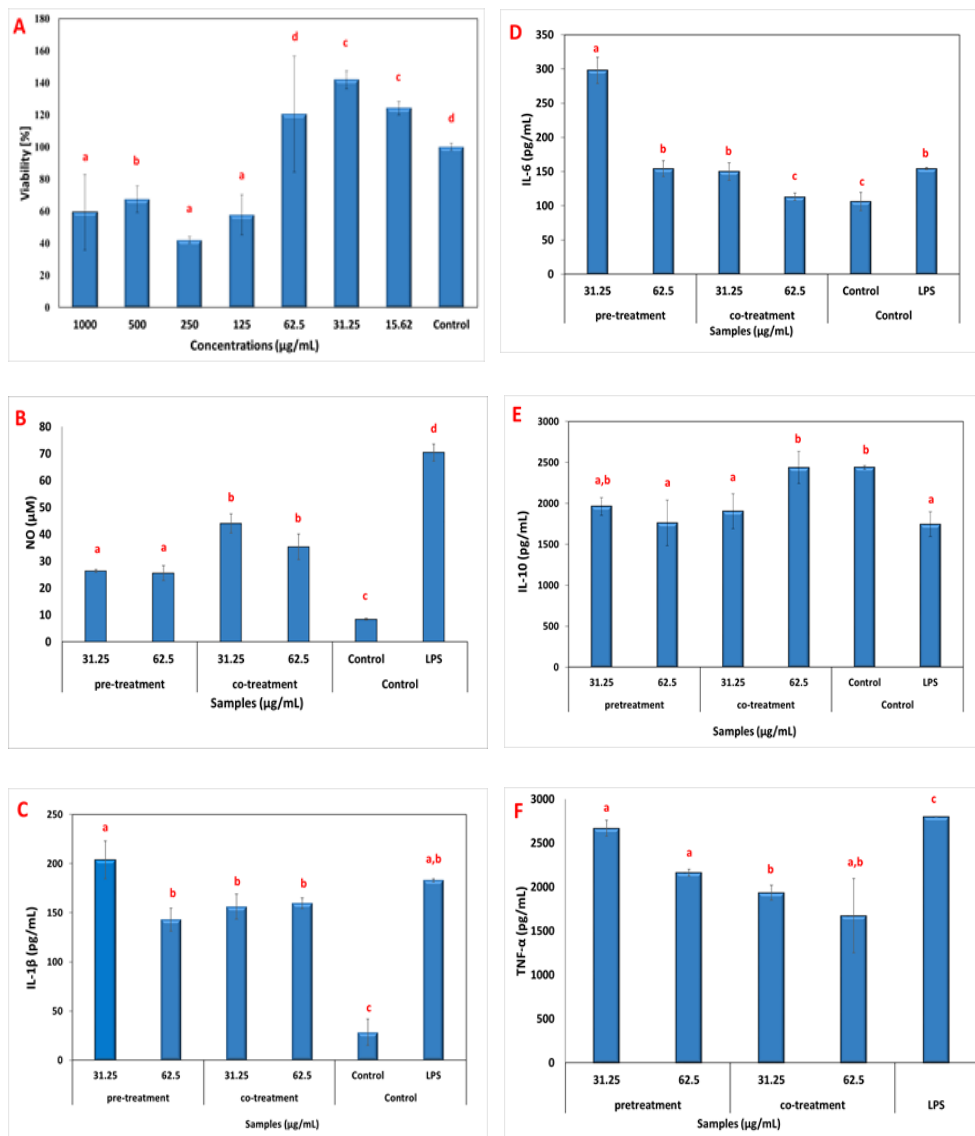
Figure 4. Anti-inflammatory activity of the *C. coggygria*. A: Toxicity profile of the extract; B: Amount of NO; C: Amount of IL-1β; D: Amount of IL-6; E: Amount of IL-10; F: Amount of TNF-*α*. Values are the mean ± SD (n = 3). [a–d] identical lowercase letters indicate statistical differences (p > 0.05).

A significantly decreased amount of IL-10 was detected in the LPS group (p<0.001). Besides, while no major changes were observed in IL-10 levels in the pre-treatment group, it was determined that the values measured in the wells treated with high-dose extract in the co-treatment group approached the control values with a significant (p<0.05) increase (Figure 4E).

The results exhibited that the LPS group had a substantial increase in TNF-α levels. On the other hand, in the co-treatment group, the TNF-α levels decreased significantly to 1675.43 pg/mL at a dose of 62.5 µg/mL, indicating the potential of the extract on inflammation (Figure 4F). In contrast, no considerable difference was observed between the LPS and extract groups in the pre-treatment group, suggesting that the extract had no prophylactic effect on TNF-α production.

There are few research evaluating the *in vivo* anti-inflammatory activity of *C. coggygria*, despite the fact that there is no study in the literature revealing the anti-inflammatory activity of *C. coggygria* extracts on the RAW 264.7 cell line. In the study by Marčetić et al. (2013) it was reported that the ethyl acetate fraction of *C. coggygria* had the potential in minimizing inflammation in a carrageenan-induced rat paw edema model and the group administered 100 mg/kg was evaluated to be more active than indomethacin (p < 0.01) [12]. Additionally, the more recent investigation by Şen et al. (2023) exemplified that *C. coggygria* extract had a positive result in decreasing the amounts of well-known cytokines (TNF-α, IL-1β, IL-6, and TGF-1β levels) in an acetic acid-induced rat colitis model. The findings from these *in vivo* models were supported by current research results on the RAW 264.7 cell line, which revealed the anti-inflammatory potential of *C. coggygria* extracts *in vitro*. These findings suggest that *C. coggygria* extracts may have the potential as a natural anti-inflammatory agent [34].

CONCLUSIONS

This work highlights the chemical composition, antioxidant, cytotoxic, anti-diabetic, and anti-inflammatory activities of *Cotinus coggygria* leaves methanol extract. It has been proven that *C. coggygria* leaves contain a significant amount of biologically active chemicals, particularly phenolic compounds. The methanol extract displayed antioxidant activity and had a strong effect on the alpha-glucosidase enzyme. Docking analyses showed that the compounds with the highest binding interaction energies for the alpha-glucosidase enzyme were galloyl hexose and methyl trigallate, thus consistent with the use of the plant. The fact that the extract exhibited significant inhibition of viability to both breast cancer cell lines even at a concentration

of 31.25 µg/mL indicates that research should continue in this direction. Considering the results, 62.5 µg/mL *C. coggygria* extract had a significant effect on TNF-*α* and IL-6 cytokine levels. A significant effect on IL-1β levels was observed in the pre-treatment group, again at a dose of 62.5 µg/mL. The effect of the extract on IL-10 cytokine level was determined as the highest at 31.25 µg/mL dose. In light of these results, it can be said that the plant has an anti-inflammatory effect. With this research, it is emphasized that this plant has very serious biological activities, but standardized extract preparation studies should be the next goal on the way from the plant to the drug.

EXPERIMENTAL SECTION

Plant material and extraction

C. coggygria Scop. utilized in the experiments were collected from the Muğla-Fethiye (Mediterranean Region, Turkiye), during the flowering season of the plant. Identification of the plant was performed by Professor Müberra Koşar. The herbarium sample of the plant (GNK 1001) is kept in the Erciyes University Faculty of Pharmacy.

150 g of dried herbal material was roughly ground and subjected to three 24-hour macerations using 70% methanol as the solvent in a shaking water bath. After filtering, the obtained extracts were concentrated in a rotavapor (37 °C) under a vacuum. After being lyophilized, the entire extract was kept at -18ºC until analysis.

Composition analysis

Total phenol, flavonoid and flavonol content determination

The total content of phenol (TPC) present in the extract was defined as equivalent to gallic acid by the Folin-Ciocalteu method, the total content of flavonoid (TFC) equivalent to catechin was defined by the method used by Zhishen et al. (1999), and the total content of flavonol equivalent to the rutin was defined by Miliauskas et al. (2004)'s method [35- 37].

High-pressure liquid chromatography-mass spectrometry (LC-MS/MS) analysis

The Shimadzu LC/MS-8040 LC-MS/MS system was used as the detector, and the ESI negative ion acquisition technique was employed for analysis. The mobile phase consisted of a 50:50 mixture of solvent A and

solvent B, with a flow rate of 0.2 mL/min. Solvent A was 1% acetic acid in the water, and solvent B was 1% acetic acid in methanol. The sample was injected at a volume of 1 µL, and elution was performed using aqueous methanol. The fundamental peaks and molecular ion peaks were analyzed.

Antioxidant activity

Determination of ferric reduction power (FRAP)

The extracts and standards were mixed with 0.2 M phosphate buffer (pH 6.6) and 1% potassium hexacyanoferrate solution to determine the activities that will be assessed in the FRAP experiment. This mixture was incubated at 50°C for 30 minutes before 2.5 mL of 10% trichloroacetic acid (TCA) was added. 2.5 mL was then removed from the upper portions of the centrifuged samples. This portion was mixed with 2.5 mL of water and 0.5 mL of 0.1% $FeCl_3$. Standards included Butylated hydroxytoluene (BHT), Butylated hydroxyanisole (BHA), rosmarinic acid (RA), ascorbic acid (AA), and gallic acid (GA). Absorbance measurement was performed at 700 nm. To evaluate the ferric-reducing ability, the results were calculated as equivalent to ascorbic acid [38].

DPPH • scavenging effect

To determine the DPPH radical scavenging activities of the extracts, standards including BHT, BHA, GA, AA, and RA were combined with Tris-HCl buffer (50 nM, pH 7.4) and 0.1 mM methanol. After 30 minutes of incubation in a dark environment at room temperature, the absorbances were measured at 517 nm. The activity of the extracts was compared to the standards to calculate percent inhibition, which was determined using the following equation. Nonlinear regression curves via Sigma Plot 2001 version 7.0 (SPSS Inc., Chicago IL) were used to calculate IC_{50} values, as described by Gyamfi et al. (1999) [39].

$$\% \text{ Inhibition} = [(\text{Abs}_{control} - \text{Abs}_{sample}) / \text{Abs}_{control}] \times 100 \quad \text{Eq.1}$$

ABTS$^{•+}$ scavenging effect

The ABTS$^{•+}$ scavenging effects of the extracts and standards were evaluated using an ethanol solution of ABTS$^{•+}$. The ABTS$^{•+}$ solution was prepared by combining a 7 mM aqueous solution of ABTS with 2.45 mM $K_2S_2O_8$ and incubating it in a dark environment for 16 hours. The absorbance of the ABTS$^{•+}$ solution was adjusted to 0.700 ±0.024 at 734 nm using ethanol. To assess the kinetics of the reaction, 990 µL of the radical solution was mixed with 10 µL of the sample, and the absorbance was measured at

734 nm at 1-minute intervals for 30 minutes. The Trolox equivalent antioxidant capacity (TEAC) value was calculated by determining the percent inhibition and comparing it to the concentration of Trolox. The mean values of three parallel experiments were calculated, as described by Re et al. (1998) [40].

Determination of β-carotene / linoleic acid co-oxidation inhibitory effect

Tween 20 and linoleic acid, each weighing 120 mg, were mixed with 1mg/mL of *β* -carotene in 1.2 mL of chloroform. After the chloroform of the mixture was removed via the rotavapor, distilled water was added in small amounts in a total volume of 300 mL with stirring. This prepared emulsion was combined with the extract and standards at a concentration of 1 mg/mL. To carry out autoxidation, it was kept in a water bath at 50 °C, and samples were taken from the tubes every 15 minutes for 2 hours. Measurements of these samples taken at certain time intervals were made at 470 nm and the degree of fading was determined Antioxidant activity percentages (AA%) were calculated using Equation 2 [41].

$$AA\% = [1 - (Abs^0 \, sample - Abs^{120} sample) / (Abs^0 \, control - Abs^{120} \, control)] \times 100 \qquad Eq \, 2.$$

Ascorbate-Fe (III) -catalyzed phospholipid peroxidation inhibition

Commercially available Bovine brain extract (Folch VII) was sonicated in an ice bath and mixed with 10 mM phosphate buffer (PBS, pH 7.4) to obtain phospholipid liposome (5 mg/mL). 0.2 mL of this prepared liposome was taken and combined with 0.5 mL of PBS buffer, 0.1 mL of 1 mM $FeCl_3$, and 0.1 mL of extract/standards. 0.1 mL of 1 mM ascorbate solution was added to accelerate peroxidation. After this mixture was incubated at 37ºC for 60 minutes, 50 µL of 2% BHT, 1 mL of 2.8% TCA, and 1 mL of 1% TBA (in 0.05 M NaOH) were added. Each sample was extracted with 2 mL of *n*-butanol and the resulting (TBA) 2-MDA chromogens were allowed to switch to the *n*-butanol phase. To measure the degree of peroxidation, absorbances were recorded at 532 nm [42].

The ferrous ion chelating activity

200 µL extract solution, 100 µL 2.0 mM aqueous $FeCl_2$, and 900 µL methanol were mixed. After the reaction mixture was incubated for 5 minutes, the reaction was accelerated with 400 µL 5.0 mM ferrozine solution. After waiting for 10 minutes, the absorbance was measured at 562 nm [43]. The iron chelate activity was calculated according to Eq 1. using the control absorbance (Ac) and sample absorbance (As) and given as equivalent to Na_2EDTA (mgNa_2EDTA/sample).

Cytotoxic activity

Human breast adenocarcinoma cell lines, MCF-7, and MDA-MB-231 cell lines were grown in DMEM containing 10% FBS (fetal bovine serum), and 1% penicillin-streptomycin. The L929 (mouse fibroblast) cell line was grown in an EMEM medium containing 1% penicillin/streptomycin mixture solution and 10% horse serum at 37 °C in 5% CO_2 and 95% air. All cell lines were purchased from the American Type Culture Collection (Manassas, VA, USA).

The 3-[4,5-dimethylthiazol-2-yl]-2,5-diphenyltetrazolium bromide (MTT) colorimetric method, which is often used to assess toxicity, was employed to assess the effectiveness of *C. coggyria* extract on MCF-7, MDA-MB-231, and L929 cell lines. After counting the number of cells grown in culture the cells were dispensed into a 96-well microplate at 1×10^4 cells / well. Following 24 hours, the cells that had adhered to the plate's base were removed from the supernatant, and 100 µL of media with an extract concentration of 7.81–2000 g/mL was added. After a 24-hour incubation period, 100 µL of MTT (5 mg/mL in PBS) solution was dispensed into each emptied well. The wells were drained after 2 hours in the incubator, and 100 µL of dimethyl sulfoxide (DMSO) was dispensed into each well. ELISA (Biotek Synergy HT) was used to measure absorbance at 570 nm [43]. The analyses were performed in triplicate.

Enzyme inhibitory-docking analysis

α-Glucosidase inhibition assay

The procedure described by Liu et al. (2003) was followed for conducting the assay for the inhibitory activity of the -glucosidase enzyme [44]. A mixture of 2 U/mL *α*-glucosidase (50 µL) solution, phosphate buffer (1000 µL), and extract/acarbose (200 µL) was combined. Following a 10-minute incubation period at 37 °C, 50 µL of *p*-nitrophenyl-D-glucopyranoside (5 mM, pNPG) was added, and the mixture was then incubated for an additional 20 minutes at the same temperature Then, the reaction was stopped by adding 2000 µL of sodium carbonate solution prepared at 0.2 M concentration and 4700 µL of distilled water. Absorbances were measured at 405 nm with a spectrophotometer. Eq 1 was used to calculate inhibition %.

α-Amylase inhibition assay

To evaluate the inhibitory effects of the extracts on the α-amylase enzyme, a modified Sigma-Aldrich technique was used. The assay mixture consisted of 40 µL of extract or acarbose samples, 160 µL of phosphate buffer (pH 6.9) with 20 mM sodium chloride, and 200 µL of α-amylase enzyme solution (EC3.2.1.1, tip VI, Sigma; 20 unit/mL), mixed at specific dose intervals. After incubating for 5 minutes, a 0.5% w/v prepared starch

solution was added as a substrate in a volume of 400 µL and incubated for 3 more minutes at 25°C. The reaction was stopped by adding 200 µL of the dinitro salicylic acid reagent (96 mM 3,5-dinitro salicylic acid, 5.31 M sodium potassium tartrate in 2 M NaOH) and placing the tubes in a water bath at 85°C for 15 minutes. After the incubation period, the absorbance at 540 nm was measured using a spectrophotometer after the addition of 4000 µL of distilled water. Inhibition% was calculated using Eq 1.

Molecular docking

Molecular docking work was carried out with Schrödinger Maestro version 2021.2 version with protein preparation, ligand preparation, creation of active site grid box files, and ligand docking steps, respectively [45]. For the three-dimensional structure of α-glucosidase, PDB ID: 5NN8 was selected and retrieved in the 'Protein Preparation Wizard' [46,47]. The water molecule and other heteroatoms were removed, and hydrogens were added. H bond assignment was set to PROPKA:7.0, using the water molecule orientation, and minimized using OPLS4 force fields. Compounds obtained from *C. coggygria* by LC-MS/MS analysis galloyl hexose (PubChem ID: 128839), methyl trigallate (PubChem ID: 156096784), gallic acid (PubChem ID: 370), quinic acid (PubChem ID: 6508), quercetin 3-O-rhamnoside (PubChem ID: 5353915), methyl gallate (PubChem ID: 7428), digallic acid methyl (PubChem ID: 10131824), myricetin 3-rhamnoside (PubChem ID: 5352000) and acarbose (PubChem ID: 41774)) structure was downloaded in 3D SDF file format and prepared with 'LigPrep' module using OPLS4 force fields. Active site coordinates x: -6.658, y: -45.820, z: 84.129, and 25*25*25 Å3 were created with the 'Receptor Grid Generation' module. Ligand docking was performed with the Glide SP docking modüle [48]. Two- and three-dimensional visualization and protein-ligand analyses were performed with the Maestro interface and' Ligand Interaction' module.

Anti-inflammatory activity

Determination of non-toxic dose in RAW 264.7 cells

The non-toxic dose of the extract in the RAW 264.7 cell line was determined by the MTT method. The toxicity of the extract has been studied in the concentration range of 7.81 -1000 µg/mL.

Determination of IL-1β, IL 10, IL6, TNF-α, and NO amounts

Two groups, pre-treatment, and co-treatment, were designed to measure the anti-inflammatory activity. RAW 264.7 cells for both groups were distributed in a 1×10^6 number to a six-well plate. At the end of the 24 hours given for the

cells distributed in the pretreatment group to adhere, the extracts were added to the wells at a concentration of 62.5 µg/mL and 31.25 µg/mL and left for 6 hours. Then inflammation was induced by incubating with LPS at a concentration of 1 µg/mL for 24 hours. In the co-treatment group, extract at concentrations of 31.25 µg/mL and 62.5 µg/mL and LPS (1 µg/mL) were added to the wells at the same time and incubated for 24 hours [49].

The supernatant obtained from the wells was used to investigate IL-1β, IL-6, IL-10, and TNF-$α$ cytokine levels, and NO amount after centrifugation. The amount of NO was measured using Griess reagent, and the amount of cytokines was measured using commercial kits.

Statistical analysis

After performing ANOVA, Tukey, and Dunnett's tests were used to determine the significant differences between means. In this study, a significance level of $p < 0.05$ was defined as statistically significant between groups.

ACKNOWLEDGMENTS

REFERENCES

1. D.J.Newman; G.M. Cragg; *J Nat Prod., 2020*, *83(3)*, 770–803.
2. X. Zhou; S.W. Seto; D. Chang; H. Kiat; V. Razmovski-Naumovski; K. Chan; A. Bensoussan; *Front Pharmacol*., **2016**, 7, 201.
3. H. Yuan; Q. Ma; L. Ye; G. Piao; *Molecules*, **2016**, *21*(5), 559.
4. C. Türe; H. Böcük; *J Nat Conserv., 2010*, *18(4)*, 296-303.
5. S. Uğurlu; *Turkish Stud*., **2011**, *6(4)*, 317-327.
6. S. Matić; S. Stanić; M. Mihailović; D. Bogojević; *Saudi J Biol Sci*., **2016**, *23(4)*,452–461.
7. H. Aksoy; M. Sancar; A. Sen; B. Okuyan; L. Bitis; F. Uras; D. Akakin; O. Cevik; S. Kultur; F.V. İzzettin; *Nat Prod Res*., **2016**, *30(4)*, 452–455.
8. B. Ertas; B. Okuyan; A. Şen; F. Ercan; H. Önel; F. Göğer; G. Şener; *J Res Pharm*., **2022**, *26(3)*, 554-564.
9. O. Tzakou; I. Bazos; A. Yannitsaros; *Flavour Fragr J., 2005*, *20(5)*, 531-533.
10. M.S. Amjad; M. Arshad; R. Qureshi; *Asian Pac J Trop Biomed*., **2015**, *5(3)*, 234-241.

11. H. Özbek; H. Yuca; S. Gözcü; B. Dursunoğlu; N. Özvenver; Z. Güvenalp; C. Kazaz; M. Önal; L.Ö. Demirezer; *Fabad J Pharm Sci.*, **2019**, *44(2)*, 127-132.

12. M. Marčetić; D. Božić; M. Milenković; N. Malešević; S. Radulović; N. Kovačević; *Phytother Res.*, **2013**, *27(11)*, 1658–1663.

13. D.S. Antal; S. Schwaiger; E.P. Ellmerer-Müller; H. Stuppner; *Planta Med.*, **2010**, *76(15)*, 1765-1772.

14. M. Novaković; I. Vučković, P. Janaćković; M. Sokovik; A. Filipovic, V. Tesevic; S. Milosavljevic; *J Serb Chem Soc.*, **2007**, *72(11)*, 1045-1051.

15. S. Matic; S. Stanic; S. Solujic; T. Milosevic; N. Niciforovic; *Period Biol.*, **2011**, *113*, 87–92.

16. H.E. Westenburg; K.J. Lee; S.K. Lee; H.H.S. Fong; R.B.V. Breemen; J.M. Pezzuto, D. Kinghorn; *J. Nat. Prod.,* **2000**, *6*, 1696–1698.

17. K. Rendeková; S. Fialová; L. Jánošová; P. Mučaji; L. Slobodníková; *Molecules*, **2016**, *21(1)*, 50.

18. L. Regazzoni; E. Arlandini; D. Garzon; *J Pharm Biomed Anal.*, **2013**, *72*,202-207.

19. H.D. Dorman; M. Kosar; K. Kahlos; Y. Holm; R. Hiltunen; *J Agric Food Chem.*, **2003**, *51(16)*, 4563-4569.

20. M. Simić; D. Vučićević; M. Milenković; N. Kovačević; *Planta Med.*, **2008**, *74*, PA63.

21. K. Šavikin, G. Zdunić; T. Janković; T. Stanojković; Z. Juranić; N. Menković; *Nat Prod Res.*, **2009**, *23*, 1731–1739.

22. S. Sukhikh; S. Noskova; A. Pungin; S. Ivanova; L. Skrypnik; E. Chupakhin; O. Babich; *Plants.*, **2021**,*10*, 1224.

23. S. Shagun; B. Sujata; S. Manjul; *Int J Pharmacog Phytochem Res.*, **2016**, *8(7)*, 1183-1186.

24. S.C. Joshi; C.S. Mathela; *J Nat Prod Plant* Resour., **2014**, *4(3)*, 39-43.

25. M. Koşar; H.J.D. Dorman; R. Hiltunen; *Food Chem.*, **2005**, *91(3)*, 525-533.

26. B. Halliwell; *Adv Pharmacol.*, **1996**, *38*, 3-20.

27. N. Nićiforović; V. Mihailović; P. Mašković; S. Solujić; A. Stojković; D. Pavlović Muratspahić; *Food Chem Toxicol.*, **2010,** *48(11)*, 3125-3130.

28. Z.I. Gospodinova; I. Zupkó; N. Bózsity; V.I. Manova; M.S. Georgieva; S.J. Todinova; S.G. Taneva; I. Ocsovszki; M.E. Krasteva; *Z Naturforsch C J Biosci.*, **2020**, *76(3-4)*, 129-140.

29. I. Iliev; I. Ivanov; K. Todorova; D. Tasheva; M. Dimitrova; *Acta Morphol.*, **2021**, *28(1-2)*, 13-18.

30. J.A. Junejo; K. Zaman; M. Rudrapal; I. Celik; E.I. Attah; *S Afr J Bot.*, **2021**, *143*, 164-175.

31. C.A. Dinarello; *Chest.*, **2000**, *118(2)*, 503-508.

32. T.R. Mosmann; K.W. Moore; *Immunol Today.*, **1991**, *12(3)*, A49-53.

33. M. Rizk; M.B. Witte; A. Barbul; *World J Surg.*, **2004**, *28(3)*, 301-306.

34. A. Şen; B. Ertaş; Ö. Çevik; A. Yıldırım; D.G. Kayalı; D. Akakın; L. Bitiş; G. Şener; *Appl Biochem Biotechnol.*, **2023**, 10.1007/s12010-023-04474-1.

35. V.L. Singleton; R. Orthofer; R.M. Lamuela-Raventós; *Meth Enzymol.*, **1999**, *299,* 152–178.

36. J. Zhishen; T. Mengcheng; W. Jianming; *Food Chem.*, **1999**, *64(4)*, 555-559.

37. G. Miliauskas; P.R. Venskutonis; T.A. Van Beek; *Food Chem.*, **2004**, *85(2)*, 231-237.

38. G. Şeker Karatoprak; Ç. Yücel Aşık; A. Çakır; E. Köngül Şafak; *Int J Environ Health Res*, 2021, *31(8)*, 991–1000.

39. M.A. Gyamfi; M. Yonamine; Y. Aniya; *Gen Pharmacol -Vasc S.*, **1999**, *32(6)*, 661-667.

40. R. Re; N. Pellegrini; A. Proteggente; A. Pannala; M. Yang; C. Rice-Evans; *Free Radic Biol Med.*, **1999**, *26(9)*, 1231-1237.

41. B.D. Oomah; G. Mazza; *J Agric Food Chem.*, **1996**, *44*, 1746–1750.

42. O.I. Aruoma; J.P. Spencer; D. Warren; *Food Chem.*, **1997**, *60(2)*, 149-156.

43. J.k. Taher Al-Isawi; A.M. Mohammed; D.T.A. Al-Heetimi; *Studia UBB Chemia,* **2023**, *67(2)*, 131-144.

44. S. Liu; D. Li; B. Huang; Y. Chen; X. Lu; Y. Wang; *J Ethnopharmacol.*, **2003**, *149*, 263–269.

45. D.S. Ghallab; E. Shawky; A.M. Metwally; I. Celik; R.S. Ibrahim; MM. Mohyeldin; *RSC Adv.*, **2022**, *12(5)*, 2843-2872.

46. K. Karrouchi; I. Celik; S. Fettach; T. Karthick; K. Bougrin; S. Radi; M. El Abbes Faozi; M. Ansar; R. Renjith; *J Mol Struct.*, **2022**, *1265*, 133363.

47. V. Roig-Zamboni; B. Cobucci-Ponzano; R. Iacono; M.C. Ferrara; S. Germany; Y. Bourne; G. Parenti; M. Moracci; G. Sulzenbacher; *Nat Commun.*, **2017**, *8*, 1111.

48. R.A. Friesner; J.L. Banks; R.B. Murphy; T.A. Halgren; J.J. Klicic; D.T. Mainz; M.P. Repasky; E.H. Knoll; M. Shelley; J.K. Perry; *J Med Chem.*, **2004**, *47(7)*, 1739-1749.

49. G. Şeker Karatoprak; S. İlgün; M. Koşar; *Chem Biodivers.*, **2017**, *14(9)*, e1700150.

COMPARISON OF ANTIOXIDANT ACTIVITY, TOTAL PHENOLIC, FLAVONOID, PROANTHOCYANIDIN, SAPONIN CONTENTS OF EGGPLANT'S (*SOLANUM MELONGENA L.*) PULP AND PEEL – A CHEMOMETRIC APPROACH

Violeta D. MITIĆ[a], Jelena S. NIKOLIĆ[a],
Marija V. DIMITRIJEVIĆ[a], Jelena M. MRMOŠANIN[a,*],
Snežana B. TOŠIĆ[a], Aleksandra N. PAVLOVIĆ[a],
Vesna P. STANKOV JOVANOVIĆ[a]

ABSTRACT. The eggplant is a vegetable that has been used more in recent years thanks to the low calories versus high content of phenolic compounds. This study aimed to determine total phenolic, flavonoid, proanthocyanidin, and saponin content using spectrophotometric assays and antioxidant activity using 2,2-diphenyl-1-picryl-hydrazyl-hydrate (DPPH), 2,2'-azinobis(3-ethylbenzothiazol-6sulpho-nate (ABTS), total reducing power (TRP), ferric reducing antioxidant power (FRAP), and cupric reducing antioxidant capacity (CUPRAC) assassin peel and pulp of eggplant cultivars Robi, Tudela, Vernal, Aragon, and Rosa Bianca. The average total saponin content (TSC) in peel was 116.34 µg DSGE mg^{-1} DW (diosgenin equivalents per mg of extract's dry weight), whereas in pulp was slightly lower (107.86 µg DSGE mg^{-1} DW). A similar trend was observed for total phenolic content (TPC) (24.54 µg GAE mg^{-1} DW (gallic acid equivalents per mg of extract's dry weight) in peel and 15.88 µg GAE mg^{-1} DW in pulp; total proanthocyanidin (TP) (2.74 µg CE mg^{-1} DW (catechin equivalents per mg of extract's dry weight) in peel and 1.24 µg CE mg^{-1} DW in pulp) and total flavonoid content (TFC) (0,05 µg RE mg^{-1} DW (rutin equivalents per mg of extract's dry weight) in peel and 0.02 µg RE mg^{-1} DW in pulp). Principal component analysis (PCA) and cluster analysis (CA) methods were applied on the antioxidant activity (ABTS, DPPH, TRP, FRAP, and CUPRAC) and total bioactive compounds

---

[a] *University of Niš, Faculty of Sciences and Mathematics, Department of Chemistry, Višegradska 33, P.O. Box 224, 18000 Niš, Serbia*
[*] *Corresponding author: jelena.mrmosanin@pmf.edu.rs*

VIOLETA D. MITIĆ, JELENA S. NIKOLIĆ, MARIJA V. DIMITRIJEVIĆ, JELENA M. MRMOŠANIN, SNEŽANA B. TOŠIĆ, ALEKSANDRA N. PAVLOVIĆ, VESNA P. STANKOV JOVANOVIĆ

content (TSC, TPC, TP and TFC) parameters in order to reveal the relationships between analyzed samples. As a result of these approaches, analyzed samples were grouped into two groups.

Keywords: *Eggplant, Solanum Melongena, Antioxidants, Chemometric analysis*

INTRODUCTION

Eggplant (*Solanum melongena L.*), also known as aubergine, comes in wide varieties with various shapes (oval, ovoid shape, long club-shaped) and colours (white, yellow, green, and purple) [1, 2]. It is grown worldwide and is used in a diet because of the high concentration of bio-friendly metals (K, Mg, Ca, and Fe), low-calorie content, and affordable price [3].

Due to its high phenolic, alkaloid, and vitamin contents, the eggplant-rich diet positively affected hypercholesterolemia, asthma, diabetes, bronchitis, and digestive difficulty [4]. It has anti-inflammatory, hepatoprotective, hypolipidemic, antiallergic, and anticancer activity [5]. Many studies have shown that phenol compounds are responsible for the antioxidant activity of eggplant [6]. Kaushik et al. [7] found that eggplant has the most outstanding total phenolic acid content among 21 different vegetables, and the major soluble phenolic acid in eggplant is chlorogenic acid and its isomers. Caffeic acid and *p*-coumaric acid were also present in eggplant samples. The polyphenol oxidase catalyzes the enzymatic oxidation of phenol compounds to the quinones, which polymerize into water-soluble brown melanin [8]. The main anthocyanin present in eggplant peel was nasunin [9].

Previous studies have dealt with the identification and quantification of polyphenolic compounds using high-performance liquid chromatography (HPLC) [9,10], total phenolic content (TPC), and total flavonoid content (TFC) [5, 9-12]. Antioxidant activity was also estimated using ABTS [10, 12], DPPH [5], and FRAP assays [13]. Depending on the thermodynamic conditions and reactivity of the phenols' hydroxyl groups, it has been found that different oxidants transform the substrate into different products. Therefore, using multiple antioxidant assays is recommended to get a comprehensive picture of one's antioxidant characteristics.

The present study aimed to determine and compare the antioxidant activity of five eggplant cultivars peel and pulp, dominantly present in the Serbian markets, using five spectrophotometric assays (DPPH, ABTS, FRAP, TRP, and CUPRAC) and total flavonoid content (TFC), total phenolic (TPC) content, total proanthocyanidin (TP), and total saponin (TS) content. To the

best author's knowledge, total proanthocyanidin and saponin content in eggplant samples is evaluated for the first time. The obtained data were subjected to chemometric analysis to estimate the relations between peel and pulp of different eggplant varieties and used assays.

RESULTS AND DISCUSSION

Total phenolic, flavonoid, proanthocyanidin, saponin contents, and antioxidant activities of eggplant extracts

Phenolic compounds are secondary metabolites often combined with mono and polysaccharides via phenolic groups [14]. The main dietary phenolics are phenolic acids, flavonoids, and polyphenols [15]. Many studies have shown [16, 17] a positive and high correlation between phenolic compounds and the antioxidant potential of vegetables and fruits. The hydroxyl groups' hydrogen atoms in the o-position in rings A, B, and C, double bonds in aromatic rings, and C=O bonds are responsible for their high antioxidant activity [18].

DPPH, ABTS, CUPRAC, FRAP, and TRP are widespread since they apply to various samples, are reproducible, low-cost, and, above all, reliable. The antioxidant potentials of eggplant peel and pulp extracts were determined using five different spectrophotometric assays, and the results are presented in Table 1.

Table 1. Antioxidant activity of eggplant samples using five different assays
(DPPH, ABTS, TRP, FRAP, and CUPRAC)

Name	Part of the eggplant	DPPH[1] (μg TE mg^{-1} DW) [2]	ABTS (μg TE mg^{-1} DW) [2]	TRP (μg AAE mg^{-1} DW) [2]	FRAP (μg FE mg^{-1} DW) [2]	CUPRAC (μg TE mg^{-1} DW) [2]
Robi	Pulp	1.15 ± 0.04	59.0 ± 0.4	18.30 ± 0.07	16.02 ± 0.03	84.72 ± 0.07
	Peel	11.0 ± 0.1	3.16 ± 0.06	24.7 ± 0.2	52.52 ± 0.04	80.48 ± 0.06
Tudela	Pulp	3.2 ± 0.1	8.6 ± 0.3	26.13 ± 0.04	21.72 ± 0.02	62.31 ± 0.08
	Peel	9.5 ± 0.3	3.18 ± 0.08	29.15 ± 0.07	47.32 ± 0.03	88.67 ± 0.09
Vernal	Pulp	4.6 ± 0.1	6.14 ± 0.009	22.7 ± 0.1	22.63 ± 0.03	63.68 ± 0.7
	Peel	11.1 ± 0.1	2.60 ± 0.03	29.8 ± 0.2	47.82 ± 0.07	90.3 ± 0.1
Aragon	Pulp	1.79 ± 0.02	11.44 ± 0.03	17.03 ± 0.04	14.22 ± 0.03	52.74 ± 0.05
	Peel	8.4 ± 0.3	7.2 ± 0.1	22.1 ± 0.1	43.32 ± 0.02	68.32 ± 0.03
Rosa Bianca	Pulp	2.19 ± 0.09	9.52 ± 0.07	17.80 ± 0.07	20.52 ± 0.05	73.24 ± 0.09
	Peel	5.07 ± 0.08	9.16 ± 0.01	16.61 ± 0.01	19.82 ± 0.04	56.70 ± 0.04

[1] mean ± SD,
[2] TE - Trolox equivalent, AAE - ascorbic acid equivalent, FE - Fe(II) equivalent, DW – dry weight.

VIOLETA D. MITIĆ, JELENA S. NIKOLIĆ, MARIJA V. DIMITRIJEVIĆ, JELENA M. MRMOŠANIN, SNEŽANA B. TOŠIĆ, ALEKSANDRA N. PAVLOVIĆ, VESNA P. STANKOV JOVANOVIĆ

Pulp extracts showed lower antioxidant activity, ranging from 52.74 to 84.72 µg TE mg^{-1} DW, than peel extracts (56.7 to 88.64µg TE mg^{-1} DW) according to the CUPRAC method. Antioxidant activity for eggplant in the study of Pasli et al. [19] was 72.59 µg TE mg^{-1} DW, which agrees with the results we obtained. Antioxidant activity determined using ABTS and DPPH was lower than those obtained by the CUPRAC assay. These results are most likely a consequence of the reaction mechanism on which the assays are based. In DPPH and ABTS assays, antioxidants react with organic radicals, so only smaller molecules can react due to the steric effect [20]. ABTS radical cation is formed in a reaction between ABTS and potassium persulfate. ABTS radical cation solution is then mixed with antioxidants from a sample and reduced to ABTS again. Its reduction depends on antioxidant concentration and reaction time. For peel samples, ABTS assay results ranged from 2.6 µg TE mg^{-1} DW (Vernal) to 9.16 µg TE mg^{-1} DW (Rosa Bianca). Results using the same assay for pulp extracts gave higher results, ranging from 6.14 µg TE mg^{-1} DW (Vernal) to 59 µg TE mg^{-1} DW (Robi). DPPH assay results differ from results obtained using ABTS assay, with slightly higher results for peel extract ranging from 5.07 µg TE mg^{-1} DW (Rosa Bianca) to 11.1 µg TE mg^{-1} DW (Vernal); than pulp samples ranging from 1.15µg TE mg^{-1} DW (Robi) to 4.6 µg TE mg^{-1} DW (Vernal). Pasli et al. [19] also analyzed eggplant extracts and recorded 27.87 µg TE mg^{-1} for ABTS and 23.43 µg TE mg^{-1} for DPPH assay. Colak et al. [20] have determined DPPH activity; the activity ranges 0.66 µg TE mg^{-1} FW (fresh weight) for white eggplant peel, 0.84 µg TE mg^{-1} FW for purple eggplant peel and 2.04 µg TE mg^{-1} FW for black eggplant peel; 0.166 µg TE mg^{-1} FW for white eggplant pulp, 0.364µg TE mg^{-1} FW for purple eggplant pulp and 0.584 µg TE mg^{-1} FW for black eggplant peel. Colak et al. [20] also obtained higher DPPH activities in peel samples than in pulp samples, which is consistent with our results.

FRAP and TRP assays both include the reduction of Fe^{3+} to Fe^{2+} with antioxidants from the sample. Results obtained using TRP and FRAP methods were similar: TRP assay's lowest values were 16.61 µg AAE (ascorbic acid equivalent) mg^{-1} DW for Rosa Bianca peel extract and 29.8 µg AAE mg^{-1} DW for Vernal peel extract. Unlike peel samples, pulp samples have slightly higher values using TRP assay than FRAP assays, except for the pulp sample Rosa Bianca which is lower. TRP activity ranges from 17.03 µg AAE mg^{-1} DW for Aragon pulp extracts to 26.13 µg AAE mg^{-1} DW for Tundela pulp extracts. FRAP values were in the range of 14.22 µg FE mg^{-1} DW for Vernal pulp extracts to 21.72 µg FE mg^{-1} DW for Tundela pulp extracts, and 19,82 µg FE mg^{-1} DW for Rosa bianca peel extracts to 52,52 µg FE mg^{-1} DW to Robi peel extracts. Also, the FRAP assay gave higher results for the peel than the pulp samples, except for the Rosa Bianca sample. Boulekbache-Makhlouf et al. [21] analyzed the byproduct of eggplants and recorded a reducing power of 39 mg QE 100 g^{-1} DW for methanolic extract.

Saponins are a class of compounds characterized by a skeleton derived from the 30-carbon precursor oxide-squalene to which glycosyl residues are attached [22]. Saponins found in eggplant act as pancreatic lipase inhibitors, which can be used in obesity treatment [23]. Total saponin content ranged from 102.3 µg DSGE mg^{-1} DW in Rosa Bianca to 140.4 µg DSGE mg^{-1} DW in Tudela peel (Table 2). Similar total saponin content was found in the pulp samples, from 100.5 µg DSGE mg^{-1} DW in Tudela to 121.8 µg DSGE mg^{-1} DW in Robi. In the review of published papers, only Hoang et al. [24] determined the TSC (total saponin content) by spectrophotometric method. According to these authors, the content is from 18.05 µg mg^{-1} DW for aqueous extracts to 38.34 µg mg^{-1} DW for methanolic extracts.

The bitterness of eggplant can come from a high concentration of saponins [25]. It was reported that some processing techniques (milling, boiling, and steaming) reduced bitterness and saponin content [26]. Also, *Solanum melongena L.* can be used to treat several diseases like bronchitis, arthritis, asthma, and diabetes. The main phenolic compounds are in the pulp and peel, so unpeeled eggplant should be consumed.

Table 2. Total phenolic, saponin, flavonoid,
and proanthocyanidin content of eggplant samples

Name	Part of the eggplant	TPC[1] (µg GAE mg^{-1} DW)[2]	TSC (µg DSGE mg^{-1} DW)[2]	TFC (µg RE mg^{-1} DW)[2]	TP (µg CE mg^{-1} DW)[2]
Robi	Pulp	12.58 ± 0.04	121.8 ± 0.7	0.012 ± 0.001	1.04 ± 0.06
	Peel	26.4 ± 0.1	108.3 ± 0.6	0.064 ± 0.005	1.61 ± 0.06
Tudela	Pulp	21.52 ± 0.08	100.5 ± 0.9	0.014 ± 0.001	1.30 ± 0.03
	Peel	29.49 ± 0.08	140.4 ± 0.4	0.043 ± 0.003	4.7 ± 0.1
Vernal	Pulp	16.49 ± 0.06	104.5 ± 0.2	0.033 ± 0.001	2.05 ± 0.02
	Peel	29.4 ± 0.1	126 ± 1	0.075 ± 0.003	3.71 ± 0.09
Aragon	Pulp	13.09 ± 0.08	106.5 ± 0.2	0.0113 ± 0.0006	0.77 ± 0.01
	Peel	22.74 ± 0.04	104.7 ± 0.6	0.053 ± 0.002	2.5 ± 0.1
Rosa Bianca	Pulp	15.70 ± 0.06	106 ± 1	0.011 ± 0.001	1.02 ± 0.05
	Peel	14.65 ± 0.07	102.3 ± 0.3	0.022 ± 0.002	1.18 ± 0.06

[1] mean ± SD,
[2] GAE - gallic equivalent, DSGE - diosgenin equivalent, RE - rutin equivalent, CE – catechin equivalent, DW – dry weight.

VIOLETA D. MITIĆ, JELENA S. NIKOLIĆ, MARIJA V. DIMITRIJEVIĆ, JELENA M. MRMOŠANIN, SNEŽANA B. TOŠIĆ, ALEKSANDRA N. PAVLOVIĆ, VESNA P. STANKOV JOVANOVIĆ

Phenolic compounds are listed as the primary antioxidants in plant tissue, so determining their content can serve as quick antioxidant activity estimation. Cao et al. [27] characterized eggplant as among the top ten vegetables with high antioxidant activity. The total phenolic content ranged from 14.65 µg GAE mg^{-1} DW for Rosa bianca to 29.49 µg GAE mg^{-1} DW for Tudela peel extracts. Pulp samples had lower TPC, ranging from 12.58 µg GAE mg^{-1} DW for Robi to 21.52 µg GAE mg^{-1} DW for Tudela. According to Djounadi et al. [28], the total phenolic content was 41.3 to 82.31 µg GAE mg^{-1} for peel samples and 15.29 to 23.78 µg GAE mg^{-1} for pulp samples for two types of eggplant. Salerno et al. [5] also investigated total phenolic content in eggplant samples, and their results were lower, ranging from 4.49 to 4.80 µg GAE mg^{-1} DW for pulp samples and 6.12 to 6.78 µg GAE mg^{-1} DW for peel samples. According to Arkoub-Djermoune et al. [29], the total phenolic content in eggplant samples using 70% methanol as solvent was 6.69 µg GAE mg^{-1}. Ferarsa et al. [30] reported that TPC ranged from 0.02 µg GAE mg^{-1} DW to 1.99 µg GAE mg^{-1} DW. Somewhat different values obtained in this study may be due to differences in antioxidant activity assay conditions and/or different antioxidant activities of analyzed eggplants species. The present study results follow the trend established in previous studies - the higher total phenolic content in eggplant peel versus its pulp.

The total flavonoid content ranged from 0.022 µg RE mg^{-1} DW for Rosa Bianca peel extracts to 0.075 µg RE mg^{-1} DW for Vernal peel samples. TFC ranged from 0.011 µg RE mg^{-1} DW for Rosa Bianca pulp extracts to 0.033 µg RE mg^{-1} DW for Vernal pulp samples. Total flavonoid content was higher in all peel extracts than in pulp extracts of the same type of eggplants. According to Nayanathara et al. [31], total flavonoid content ranged from 22.62 µg CE mg^{-1} DW for the Long green eggplant sample to 102.01 µg CE mg^{-1} DW for the Violet uphold eggplant sample. Boulekbache-Makhlouf et al. [21] reported total flavonoid content in methanolic extract eggplant was 0.1626 µg QE mg^{-1} DW. Comparing the results presented in this study with the previous studies is problematic since, in the previous study, experiments were done with different standards (catechin and quercetin), and the results were recalculated to fresh weight while our results refer to dry weight. The big issue for comparison still stands - water percentage, which can vary significantly depending on species, climate and storage sample conditions. Nevertheless, the trend is the same-higher flavonoid content in the peel versus pulp.

Among phenolics in fruits and vegetables, there is a large group of compounds called proanthocyanidins, also known as condensed tannins [32]. The total proanthocyanidin contents in tested samples were higher in the peel than in pulp extracts. Peel extracts' total proanthocyanidin content varied from 1.18 to 4.7 µg CE mg^{-1}, while pulp extracts ranged from 0.77 to 2.05 µg CE mg^{-1}.

Considering the present results, we can conclude that the total proanthocyanidin's content were higher in the peel than in the pulp samples.

Antioxidant Composite Index (ACI)

Because the antioxidant activity of extracts was obtained by five different assays: two assays based on reactions with free radicals (ABTS and DPPH), two assays based on the reducing power of iron (TRP and FRAP), and one assay based on the reducing power of cupric ion (CUPRAC), results are challenging to compare. Therefore, the antioxidant activity index (ABTS, DPPH, TRP, FRAP, and CUPRAC index) and antioxidant composite index - ACI index were calculated and presented in Table 3. The results of the antioxidant index and ACI index were given as relative percentages. The highest ACI index, based on the results of five antioxidant activity assays, was recorded for the Vernal peel sample (78.1), followed by Robi peel (75.3) and Tudela peel (74.4). All peel samples had a higher ACI index than pulp samples of the same type. The sample Vernal peel had the highest $DPPH_{index}$, TRP_{index} and $CUPRAC_{index}$. The lowest ACI index was noticed for sample Aragon pulp.

Table 3. The antioxidant composite index for eggplant samples
calculated from five different antioxidant activity assays

Name	Sample	DPPH$_{index}$	ABTSi$_{index}$	TRP$_{index}$	FRAP$_{index}$	CUPRAC$_{index}$	ACI$_{ndex}$
Robi	Pulp	10.4	100.0	61.4	28.8	93.8	58.9
	Peel	99.1	5.4	82.9	100.0	89.1	75.3
Tudela	Pulp	28.8	14.6	87.7	39.1	69.0	47.7
	Peel	85.6	5.4	97.8	85.2	98.2	74.4
Vernal	Pulp	41.4	10.4	76.2	40.8	70.5	47.9
	Peel	100.0	4.4	100.0	86.1	100.0	78.1
Aragon	Pulp	16.1	19.4	57.1	25.6	58.4	35.3
	Peel	75.7	12.2	74.2	78.0	75.7	63.2
Rosa Bianca	Pulp	19.7	16.1	59.7	37.0	81.1	42.7
	Peel	45.7	15.5	55.7	35.7	62.8	43.1

VIOLETA D. MITIĆ, JELENA S. NIKOLIĆ, MARIJA V. DIMITRIJEVIĆ, JELENA M. MRMOŠANIN, SNEŽANA B. TOŠIĆ, ALEKSANDRA N. PAVLOVIĆ, VESNA P. STANKOV JOVANOVIĆ

Statistical analysis

Statistical analysis was performed to understand further the relations between analyzed samples and methods used. The correlation matrix is given in Table 4. The correlation between the results of spectrophotometric assays - ABTS, DPPH, TRP, FRAP, CUPRAC, TPC, TFC, TSC, and TP was calculated.

Table 4. Correlation coefficient between results obtained using spectrophotometric methods

	DPPH	ABTS	TPR	FRAP	CUPRAC	TPC	TSC	TFC	TP
DPPH	1.00								
ABTS	-0.56	1.00							
TPR	**0.74**	-0.43	1.00						
FRAP	**0.97**	-0.48	**0.75**	1.00					
CUPRAC	0.54	0.17	0.61	**0.64**	1.00				
TPC	**0.90**	-0.55	**0.92**	**0.93**	0.63	1.00			
TSC	0.41	0.14	0.55	0.46	**0.81**	0.53	1.00		
TFC	**0.96**	-0.47	**0.70**	**0.92**	0.56	**0.83**	0.35	1.00	
TP	**0.74**	-0.39	**0.81**	**0.74**	**0.64**	**0.83**	0.77	**0.67**	1.00

The strongest correlation was noticed between DPPH and FRAP assays (0.97, $p < 0.05$), followed by TRP and FRAP (0.75, $p < 0.05$), DPPH, and TRP (0.74, $p < 0.05$). A strong correlation between DPPH and FRAP was reported in the literature [33, 34], which is expected because both assays share a similar mechanism, which includes electron transfer from an antioxidant to reduce an oxidant. Since the TRP assay includes a reduction of Fe^{3+} to Fe^{2+} in the FRAP assay, the correlation between them is also expected. ABTS assay showed a poor and negative correlation with other spectrophotometric assays. Also, the negative and low correlation was between ABTS assay and TPC, TSC, TFC, and TP. ABTS reacts with small molecules and can give real pictures of the antioxidant activity of plant extract [35].

A high positive correlation was recorded between TRP and TPC (0.92, $p < 0.05$), DPPH, and TPC assays (0.90, $p < 0.05$). Also, a high positive correlation was noticed between DPPH/TFC (0.96, $p < 0.05$), TRP/TFC (0.7, $p < 0.05$), and FRAP/TFC (0.7, $p < 0.05$). This positive correlation confirms that

phenolic and flavonoid compounds in eggplant samples contribute to their antioxidant activity. Proanthocyanidin also showed good correlations with TRP, FRAP, DPPH, and CUPRAC, so they also affected the antioxidant activity of eggplant samples.

Of the many chemometric techniques, the most common are used multivariate techniques that allow systematic data extraction, usually in large sets. As this method reduces the dimensionality of the initial data without losing essential information and retaining variability, the components with the most significant variance were used [36]. PCA analysis gave two principal components (PC) with eigenvalues>1, which is acceptable according to the Kaiser criterion [37]. For PC analysis, we used eggplant samples as a case, antioxidant assays (ABTS, DPPH, FRAP, and TRP), and assays for determining total phenolic, flavonoid, proanthocyanidin, and saponin content as a variable. These two principal components explain 87.26% of the total variance. The first principal component (PC1) had the highest eigenvalue (6.22), explaining 69.11% of the total variance. The second component had 1.64 eigenvalues, explaining 18.15% of the total variance. Based on the first principal component, all tested samples were grouped into two groups. The first group is on the positive sides of PC1 and PC2 and consists of eggplant pulp samples Tudela, Vernal, and Aragon and one eggplant peel samples Rosa Bianca. Aragon and Rosa Bianca pulp samples have the lowest $DPPH_{index}$ values (16.1 and 19.7, respectively). Robi pulp sample is also in this group, on the negative side of PC2. This sample stands out as a sample with the highest loading (-3.08) and the highest contribution from ABTS ($ABTS_{index}$ =100), which can also be seen in Figure 1, and Tables 1 and 3. Rosa Bianca peel and Aragon pulp samples are in the upper right quadrant (Figure 2), and CUPRAC is in the lower-left quadrant, indicating they have the lowest value of CUPRAC (CUPRAC index value is 62.8 and 58.4, respectively). The second group is on the negative side of PC1. This group consists of Robi, Tudela, Vernal, and Aragon eggplant peel samples. According to the component PC2, Robi and Aragon peel samples stand out on the positive side of PC2; these are the samples with the highest values of TPC, TFC, and the high values of DPPH (Figure 1 and Tables 1, 2 and 3). The Tudela and Vernal peel samples are on the negative side of PC2, as samples with the highest value of TSC (140.4 and 126 μg DSGE mg^{-1} DW, respectively), TP (4.7 and 3.7 μg CE mg^{-1} DW, respectively) and CUPRAC (88.67 and 90.3 μg TE mg^{-1} DW, respectively). Figure 1 shows that grouping spectrophotometric assays DPPH and FRAP with TPC and TFC; CUPRAC with TSC and TP are consistent with the Pearson correlation (Table 4).
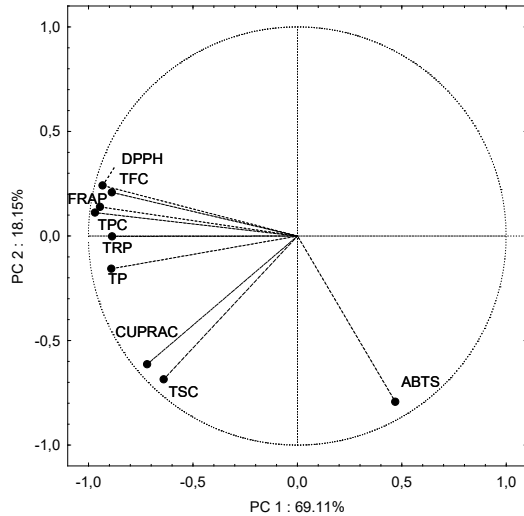
Figure 1. Grouping spectrophotometric assays based on the antioxidant activity in tasted eggplant samples using PCA
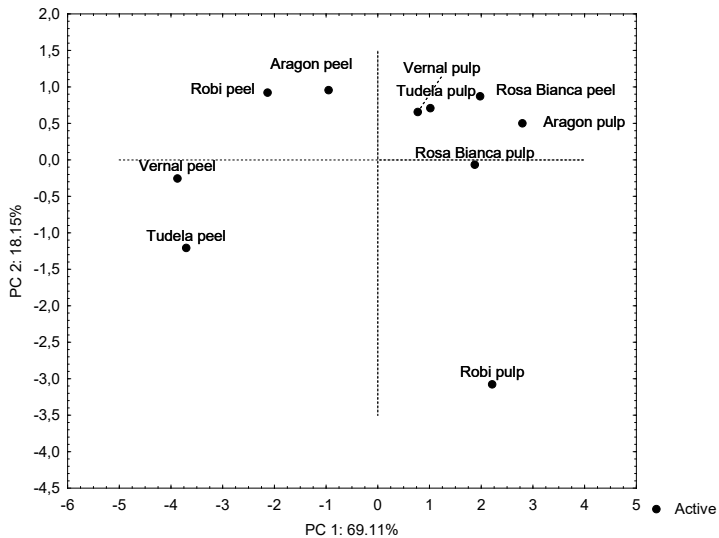
Figure 2. Grouping peel and pulp eggplant samples using PCA

From the results of the factor analysis, we can infer which assays or samples contribute to the differentiation between the peel and pulp. The original correlation matrix of the principal components underwent orthogonal varimax rotation, and Table 5 present the factor loadings of the principal components PC1 and PC2.

Table 5. The Varimax rotated matrix of principal components,
along with factor loading values and communalities

	Component		Communalities			Component		Communalities	
	PC1	PC2	Initial	Extraction		PC1	PC2	Initial	Extraction
DPPH	**0.916**	0.308	1.00	0.933	Robi peel	**0.878**	0.465	1.00	0.987
TPC	**0.872**	0.433	1.00	0.947	Vernal peel	**0.856**	0.514	1.00	0.997
FRAP	**0.871**	0.397	1.00	0.916	Aragon peel	**0.843**	0.532	1.00	0.994
ABTS	**-0.826**	0.413	1.00	0.853	Tudela peel	**0.840**	0.543	1.00	0.999
TFC	**0.815**	0.313	1.00	0.762	Vernal pulp	**0.771**	**0.633**	1.00	0.995
TRP	**0.735**	0.486	1.00	0.777	Tudela pulp	**0.765**	**0.637**	1.00	0.991
Total proanthocyanidins	**0.665**	**0.612**	1.00	0.817	Rosa Bianca pulp	**0.741**	**0.667**	1.00	0.994
Total saponins	0.167	**0.922**	1.00	0.878	Rosa Bianca peel	**0.739**	**0.668**	1.00	0.993
CUPRAC	0.272	**0.906**	1.00	0.895	Robi pulp	0.454	**0.881**	1.00	0.983
Eigen-values	6.158	**1.620**	9.00	7.778	Aragon pulp	0.693	**0.709**	1.00	0.983
Variance (%)	53.202	**33.218**	100	86.42	Eigen-values	9.656	0.26	10.00	9.913
					Variance (%)	58.818	40.341	100	99.159

For instance, DPPH, TPC, FRAP, ABTS assay show high loadings on PC1, whereas total saponins and CUPRAC exhibit hight loading on PC2. This indicates that these assays have a greater influence on the formation of the components.

High communalities for individual samples (e.g. Robi peel, Vernal peel and Aragon peel) suggest that these samples share similar characteristics or variations that are well-explained by the extracted components (PC1 and PC2). Additionally, the communalities for pulp samples (e.g. Vernal pulp, Tudela pulp) also show similar patterns.

VIOLETA D. MITIĆ, JELENA S. NIKOLIĆ, MARIJA V. DIMITRIJEVIĆ, JELENA M. MRMOŠANIN, SNEŽANA B. TOŠIĆ, ALEKSANDRA N. PAVLOVIĆ, VESNA P. STANKOV JOVANOVIĆ

The same data matrix as in principal component analysis was used for cluster analysis. This chemometric technique was used as a supplement to PCA to obtain the most accurate classification of tested samples. The results are shown in Figures 3 and 4. For clustering, Euclidean distance and Ward's method were used.
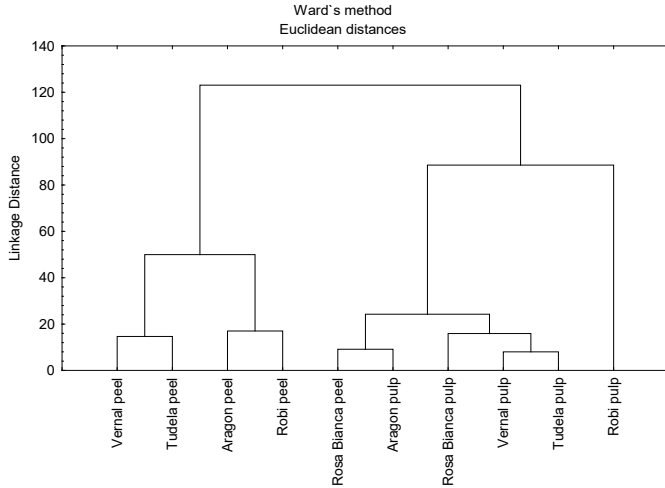
Figure 3. Grouping tested peel and pulp samples based on the antioxidant activity using CA
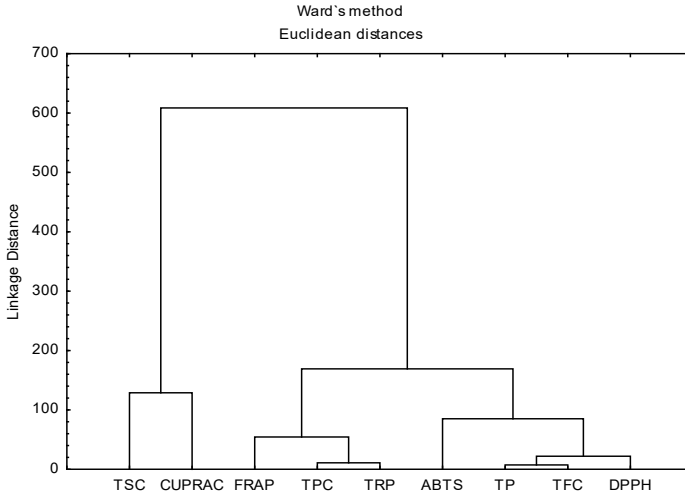
Figure 4. Grouping spectrophotometric assays based on the antioxidant activity in tested eggplant samples using CA

The first cluster consists of three subclusters: the first subcluster includes Tudela, Vernal, and Aragon pulp samples; the second cluster includes Rosa Bianca peel and Aragon pulp samples; and the third includes Robi pulp samples. The second cluster comprises two subclusters: the first subcluster includes Robi and Aragon peel samples, and the second subcluster includes Tudela and Vernal peel samples. The explanation for this grouping of the samples is the same as for PCA.

CONCLUSIONS

Antioxidant activity and bioactive compounds (phenolics, flavonoids, proanthocyanidins and saponins) in five eggplant peel and pulp samples commonly consumed in Serbia were analyzed using spectrophotometric assays. According to the results, analyzed eggplant samples have a high content of phenolic compounds and saponins. Higher total phenolic content was recorded for peel than pulp samples, which is also the case with total proanthocyanidin content. Total saponin and phenolic content strongly correlated with all assays used for antioxidant activity determination, indicating those compounds contribute the most to overall antioxidant activity. Chemometric statistical techniques (PCA and cluster analysis) formed two groups of tested samples according to antioxidant activity and total content of phenol, flavonoid, proanthocyanidin, and saponin. Using the PCA analysis the parameters differentiating the Rosa Bianca peel were revealed. They are low values of TRP, TPC and CUPRAC assay.

EXPERIMENTAL SECTION

Methods and Materials

Sample preparation and extraction procedure

Five eggplant varieties, Robi, Tudela, Vernal, Aragon, and Rosa Bianca, were purchased at the local market in Niš, Serbia. The samples were prepared according to Dranca and Oroian [38], with some modifications. The peel was washed and separated from the pulp; samples were cut into pieces and homogenized. Eggplant peel and pulp were lyophilized and kept in polyethene bags at -20°C until analysis. Lyophilized samples (1 g) were extracted twice for 15 min at 25 °C in an ultrasonic bath, using methanol as a solvent. Samples were left in the solvent overnight, filtered, and evaporated to dryness, using a vacuum rotary evaporator. Dimethyl sulphoxide (DMSO) dissolved extracts to a final concentration of 100 mg mL^{-1}.

VIOLETA D. MITIĆ, JELENA S. NIKOLIĆ, MARIJA V. DIMITRIJEVIĆ, JELENA M. MRMOŠANIN, SNEŽANA B. TOŠIĆ, ALEKSANDRA N. PAVLOVIĆ, VESNA P. STANKOV JOVANOVIĆ

Chemicals and instrumentation

2,2-Diphenyl-1-picrilhydrazyl (DPPH), 2,2'-azinobis(3-ethylbenzothiazoline-6-sulfonic acid) (ABTS), Folin-Ciocalteu reagent, iron(III) chloride hexahydrate, 6-hydroxy-2, 5, 7, 8-tetramethylchroman-2-carboxylic acid (Trolox), gallic acid, ascorbic acid, (+)-catechin hydrate, vanillin, diosgenin, rutin, and methanol were purchased from Sigma (St. Louis, Missouri, USA). Copper(II) chloride dihydrate, 2,9-dimethyl-1, 10-phenanthroline (neocuproine), sodium carbonate, hydrochloric acid, 2, 4, 6-Tris(2-pyridyl)-s-triazine (TPTZ), potassium hexacyanoferrate(III), phosphate buffer (NaH_2PO_4/Na_2HPO_4), ammonium acetate buffer, trichloroacetic acid, potassium peroxodisulfate, $AlCl_3$ x $6H_2O$, DMSO, H_2SO_4, hydrochloric acid, sodium hydroxide, sodium nitrite, and iron(II) sulfate heptahydrate were purchased from Merck (Darmstadt, Germany), all listed chemicals are of analytical grade.

For spectrophotometric analysis, UV/VIS spectrophotometer was used (Perkin Elmer Lambda 15, Massachusetts, USA).

A lyophilizer (Christ, Germany) was used to dry the samples.

DPPH radical scavenging activity

The DPPH radical assay was conducted according to the method described by Brand-Wiliams et al. [39]. The extract aliquot (10 μL) was mixed with DPPH solution and diluted with methanol to a final volume of 4 mL. After the mixture was incubated for 60 minutes in the dark at room temperature, absorbance was recorded at 515 nm. The results were expressed as μg Trolox equivalent (TE) per mg of extract's dry weight (DW).

ABTS radical scavenging activity

The ABTS radical activity assay was conducted according to the method described by Re et al. [40]. Previously prepared ABTS solution was mixed with extract aliquot (10 μL), and the mixture was diluted with methanol to a final volume of 4 mL. After the mixture was incubated (6 min; room temperature), absorbance was recorded at 734 nm. The results were expressed as μg Trolox equivalent (TE) per mg of extract's dry weight (DW).

Total Reducing Power Assay (TRP)

The total reducing power assay was determined as per the method described by Oyaizu [41], based on the ability of antioxidants in samples can reduce Fe(III) to Fe(II). Briefly, 10 μL extracts were mixed with 1 mL of 1% $K_3[Fe(CN)_6]$ and the same volume of phosphate buffer pH 6.6 solution and water. This mixture was incubated for 30 minutes at 50 °C. After incubation, 1 mL of CCl_3COOH and 0.6 mL $FeCl_3$ were added. The absorbance was recorded at 700 nm, and results were expressed as μg ascorbic acid equivalent (AAE) per mg of extract's dry weight (DW).

Ferric Reducing Antioxidant Power Assay (FRAP)

FRAP assay [42] was used method that uses antioxidants as reductants in colorimetric reaction where Fe^{3+}-TPTZ is reduced to blue Fe^{2+}-TPTZ complex. Extract aliquot (10 µL) was mixed with 3 mL of freshly prepared FRAP solution and diluted with water to a final volume of 4 mL. Then the mixture was incubated for 5 min at 37 °C, absorbance was recorded at 595 nm, and results were expressed as µg Fe(II) per mg of extract's dry weight (DW).

Cupric Ion Reducing Antioxidant Capacity Assay (CUPRAC)

CUPRAC assay of antioxidant measurement was used. The Cu(II)-neucuproine complex oxidize to orange-yellow Cu(I)-neocuproine complex [43]. The stable complex of Cu(I) with neocuproine was obtained by mixing 10 µL of extract solution, 1 mL of neocuproine, 1 mL of ammonium acetate solution, 1 mL of $CuCl_2$, and 1.9 mL of ethanol. The absorbance of this complex was measured at 450 nm after incubation for 30 minutes at room temperature. The results were expressed as µg Trolox (TE) per mg of extract's dry weight (DW).

Total Phenolic Content (TPC)

Total phenolic content was determined using modified Folin-Ciocalteu method [44]. The extract's solution volume of 0.1 mL was mixed with Folin-Ciocalteu reagent, 20% sodium carbonate, and deionized water. After incubation for 30 minutes in the dark, absorbance was measured at 750 nm. Results were expressed as µg gallic acid equivalents (GAE) per mg of extract's dry weight (DW).

Total Saponin Content (TSC)

Total saponin content was determined using spectrophotometric method as per the method described by Hiai et al. [45]. The method is based on the reaction of triterpene, oxidized by sulfuric acid with vanillin, which produces a coloured product with maximum absorbance at 544 nm. The extract's solution aliquot was mixed with vanillin and H_2SO_4, and then the mixture was incubated in a water bath for 10 minutes at 60 °C. The results were expressed as µg diosgenin equivalents (DSGE) per mg of extract's dry weight (DW).

Total Flavonoid Content (TFC)

A mixture for total flavonoid content determination was prepared by mixing 0.1 mL of the extract, deionized water, and $NaNO_2$. The obtained mixture was incubated for 5 minutes at room temperature, then $AlCl_3$ solution was added, followed by incubation for 5 minutes, and NaOH was added. The absorbance was recorded at 510 nm, according to Jia et al. [46]. The results were expressed as µg of rutin equivalents (RE) per mg of extract's dry weight (DW).

VIOLETA D. MITIĆ, JELENA S. NIKOLIĆ, MARIJA V. DIMITRIJEVIĆ, JELENA M. MRMOŠANIN,
SNEŽANA B. TOŠIĆ, ALEKSANDRA N. PAVLOVIĆ, VESNA P. STANKOV JOVANOVIĆ

Total Proanthocyanidin Assay (TP)

This assay is a quick method for quantitatively determining proanthocyanidin (condensed tannin) in many plant materials [47]. Total proanthocyanidin was estimated using method previously described by Price et al. [48]. The extract's solution was mixed with 4% vanillin and conc. HCl. After 15 minutes of incubation, absorbance was recorded at 500 nm. The results were given as μg of catechin equivalents (CE) per mg of extract's dry weight (DW).

Antioxidant Composite Index

The antioxidant composite index – ACI and the antioxidant index were calculated using the following equations [49]:

$$ACI_{index} = \frac{(ABTS_{index} + DPPH_{index} + FRAP_{index} + TRP_{index} + CUPRAC_{index})}{5} \qquad (1)$$

Where: $ABTS_{index}$, $DPPH_{index}$, $ABTS_{index}$, $FRAP_{index}$, TRP_{index} and $CUPRAC_{index}$ are calculated by taking the sample score, dividing it by the best score, and then multiplying the result by 100.

Statistical analysis

The results were presented as mean value ± standard deviation (SD) of triple measurements. Two statistical techniques were used for statistical data processing - the principal component analysis (PCA) and cluster analysis (CA) using Statistica 8.1 (StatSoft, Tusla) software. The principal component analysis is a method used to reduce the number of variables, with new variables independent of one another [50]. Cluster analysis is a chemometric technique examining variables' relationships [51]. At the same time, the dendrogram, which is obtained, gives an overview of the sample grouping based on the results of spectrophotometric assays.

ACKNOWLEDGMENTS

REFERENCES

1. M. H. Aminifard; H. Aroiee; H. Fatami; A. Ameri; S. Karimpour; *J. Cent. Eur. Agric.*, **2010**, *11*, 453–458
2. T. K. Koley; S. K. Tiwart; A. Sarkar; J. Nishad; A. Goswami; B. Singh; *Agric. Res.,* **2018**, *8*, 9–20
3. M. Zenia; B. Halina; *J. Elem.* **2008**, *13*, 269–274

4. G. E. Vural; E. Ari; *Sci. Hortic.* **2020**, *272*, 109472
5. L. Salerno; M. N. Modica; V. Pittalá; G. Romeo; M. A. Siracusa; C. Di Giacomo; V. Sorrenti; R. Acquaviva; *Sci. World J.,* **2014**, 1–6
6. M. Dimitrijević; V. Stankov-Jovanović; J. Cvetković; T. Mihajlov-Krstev; G. Stojanović; V. Mitić; *Anal. Methods,* **2015**, *7,* 4181–4191
7. P. Kaushik; L. Andujar; S. Vilanova; M. Plazas; P. Gramazio; F. J. Herraiz; N. S. Brar; J. Prohens; *Molecules*, **2015**, *20 (10),* 18464–18481
8. D. P. Uscanga-Sosa; M. B. Pérez-Gago; F. C. Gómez-Merino; J. A. Herrera-Corredor; A. S. Hernández-Cázares; A. Contreras-Oliva; *Not. Bot. Horti Agrobot. Cluj-Napoca,* **2020**, *48 (1)*, 79–89
9. G. Niño-Medina; V. Urías-Orona; M. D. Muy-Rangel; J. B. Heredia; *S. Afr. J. Bot.,* **2017**, *111*, 161–169
10. P. Šilarová; L. Boulekbache-Makhlouf; F. Pellati; L. Česlová; *Antioxidants,* **2019**, *8 (7),* 234–244
11. A. P. Singh; D. Luthria; T. Wilson; N. Vorsa; V. Singh; G. S. Banuuelos; S. Pasakdee; *Food Chem.,* **2009**, *114,* 955–961
12. B. Okmen; H. O. Sigva; S. Mutlu; S. Doganlar; A. Yemenicioglu; A. Frary; *Int. J. Food Prop.,* **2009**, *12,* 616–624
13. M. Kazemi; F. Khodaiyan; S. S. Hosseini; Z. Najari; *Waste Manag.,* **2019**, *100*, 101-111
14. J. B. Harborne; H. Baxter; G. P. Moss; *Phytochemical Dictionary: Handbook of Bioactive Compounds from Plants,* 2nd ed.; Taylor & Francis, London, **1999**, pp. 976
15. A. King; G. Young; *J. Am. Diet. Assoc.*, **1999**, *99*, 213–218
16. C. V. K. Reddy; D. Sreeramulu; M. Raghunath; *Food Res. Int.*, **2010**, *43*, 285–288
17. C. Sarawong; R. Schoenlechner; K. Sekiguchi; E. Berghofer; P. K. W. Ng; *Food Chem.*, **2014**, *143*, 33–39
18. C. A. Rice-Evans; N. J: Miller; *Free Rad. Biol. Med.*, **1996**, *20*, 933–956
19. A. A. Pasli; M. Yavuz-Düzgün; U. Altuntas; G. Altin; B. Özçelik; E. Firatligil; *Int. Food Res. J.*, **2019**, *26*, 793–800
20. N. Colak; A. Kurt-Celebi; J. Gruz; M. Strnad; S. Hayirlioglu-Ayaz; M. G. Choung; T. Esatbeyoglu; F. A. Ayaz; *Molecules*, **2022**, *27*, 2410
21. L. Boulekbache-Makhlouf; L. Medouni; S. Medouni-Adrar; L. Arkoub; K. Madani; *Ind.l Crops Bioprod.*, **2013**, *49*, 668–674
22. J. P. Vincken; L. Heng; A. de Groot; H. Gruppen; *Phytochem.*, **2007**, *68*, 275–297
23. S. Subandi; L. Zakiyaturrodliyah; T. Brotosudarmo; Saponin from purple eggplant (*Solanum Melongena* L.) and their activity as pancreatic lipase inhibitor. *IOP Conference Series: Materials Science and Engineering 509*, May 3, **2019**
24. T. N. N. Hoang; T. T. Phan; T. K. L. Phan; N. H. V. Nguyen; T. A. D. Dong; T. H. A. Le; *J. Food Process. Preserv.*, **2023**, article ID 2581641, 1–16
25. L. Heng; J. P. Vincken; G. van Koningsveld; A. Legger; *J. Sci. Food Agric.*, **2006**, *86*, 1225–1231
26. K. Sharma; R. Kaur; S. Kumar; R. Kumar Saini; S. Sharma; S. V. Pawde; V. Kumar; *Food Chem. Advanc.*, **2023**, 2, 100191
27. G. Cao; E. Sofic; R. L. Prior; *J. Agric. Food Chem.*, **1996**, *44*, 3426–3431
28. A. Djouadi; T. Lanez; C. Boubekri; *J. Fundam. Appl. Sci.*, **2016**, *8*, 223–231

29. L. Arkoub-Djermoune; F. Benmeziane; K. Madani; L. Boulekbache-Makhlouf; *Adv. Hortic. Sci.*, **2019**, *33*, 567–580
30. S. Ferarsa; W. Zhang; N. Moulai-Mostefa; L. Ding; M. Y. Jaffrin; N. Grimib; *Food Bioprod. Process.*, **2018**, *109*, 19–28
31. A. R. Nayanathara; A. Mathews; K. P. Aalolam; J. K. Reshma; *Emerg. Life Sci. Res.*, **2016**, *2*, 63–65
32. X. Han; T. Shen; H. Lou; *Int. J. Mol. Sci.*, **2007**, *8*, 950–988
33. H. X. Xu; J. W. Chen; *J. Sci. Food Agric.*, **2011**, *91*, 1057–2063
34. A. Szydłowska-Czerniak; I. Bartkowiak-Broda; I. Karlović; G. Karlovits; E. Szłyk; *Food Chem.*, **2011**, *127*, 556–563
35. R. L. Prior; X. Wu; K. Schaich; *J. Agric. Food Chem.*, **2005**, *53*, 4290–4302
36. D. Casoni; C. Sârbu; *Spectrochim. Acta A: Mol. Biomol. Spectrosc.*, **2014**, *118*, 343–348
37. H. F. Kaiser; *Educ. Psychol. Meas.*, **1960**, *0*, 141–151
38. F. Dranca; M. Oroian; LWT *J. Food Process Eng.* **2017**, *40*, e12312
39. W. Brand-Wiliams; M. E. Cuvelier, C. Berset; *Lebensmittel-Wissenschaft und-Technologie,* **1995**, *28*, 25–30
40. R. Re; N. Pellegrini; A. Proteggente; A. Pannala; M. Yang; C. Rice-Evans; *Free Radic. Biol. Med.,* **1999**, *26*, 1231–1237
41. M. Oyaizu; *Jpn. J. Nutr. Diet.,* **1986**, *44,* 307–315
42. I. F. F. Benzie; J. J. Strain; *Meth. Enzymol.,* **1999**, *299*, 15–27
43. R. Apak; K. Güçlü; M. Özyürek; S. E. Çelik; *Microchim. Acta*, **2008**, *160*, 413–419
44. R. L. Prior; X. Wu; K. Schaich; *J. Agric. Food Chem.*, **2005**, *53*, 4290–4302
45. S. Hiai; H. Oura; H. Hamanaka; Y. Odaka; *Planta Med.*, **1975**, *28*, 131–138
46. Z. Jia; M. Tang; J. Wu; *Food Chem.*, **1999**, *64*, 555–559
47. L. G. Butler; M. L. Price; J. E. Brotherton; *J. Agric. Food Chem.*, **1982**, *30*, 1087–1089
48. M. L. Price; S. V. Scoyoc; L. G. Butler; *J. Agric. Food Chem.*, **1978**, *26*, 1214–1218
49. N. P. Seeram; M. Aviram; Y. Zhang; S. M. Henning; L. Feng; M. Dreher; D. Heber; *J. Agric. Food Chem.*, **2008**, *56*, 1415–1422
50. A. C. Rencher; *Methods of Multivariate Analysis,* 2nd ed.; John Willey, New York, **1995**
51. F. Zolfaghari; H. Khosravi; A. Shahriyari; M. Jabbari; A. Abolhasani; *PLOS ONE*, **2019**, *14*, e0226355

SYNTHESIS OF BENZIMIDAZOLE-SUGAR DERIVATIVES: A POTENTIAL TREATMENT FOR ALZHEIMER'S DISEASE

Seda YUKSEKDANACI[a,*], Demet ASTLEY[b], Murat SENTURK[c]

ABSTRACT. In this study, a new series of chiral benzimidazole-glycosyl thiourea derivatives (**5-10**) were synthesized and evaluated for their inhibitory effects against hCA I, hCA II, acetylcholinesterase (AChE) and butyrylcholinesterase (BChE). The structures of the benzimidazole-glycosyl thiourea compounds were determined by FTIR, ^{1}H-NMR, ^{13}C-NMR and elemental analysis. The K_I values for the CA isoenzymes of the synthesized materials ranged from 6.03 to 42.98 nM. K_I values for cholinesterase enzymes were shown to be between 5.32 and 39.14 nM. It was observed that compound **10** is the best hCA I inhibitor (K_I:6.03 nM), compund **9** is the best hCAII inhibitor (K_I:17.29 nM) and compound **8** is the best AChE (K_I:5.32 nM) and the best BChE (K_I:18.73 nM) inhibitor.

Keywords: *Benzimidazole; amino acid; glycosyl thiourea; carbonic anhydrase; cholinesterase*

INTRODUCTION

In recent years, Alzheimer's disease (AD) has started to appear widely in the population, especially in developed countries. This disease is an important public health problem and is stated as a neurodegenerative condition manifested by abnormal behavior and intellectual decline [1,2] one of the most valid hypotheses is the "cholinergic hypothesis". The cholinergic hypothesis; suggests that disfunction of ACh-containing neurons in the brain contributes significantly to the cognitive decline observed in old age and those with AD [3].

[a] *Uşak University, Faculty of Health Sciences, Department of Occupational Health and Safety, Uşak, Turkey*
[b] *Ege University, Faculty of Science, Department of Chemistry, Izmir, Turkey*
[c] *Department of Biochemistry, Faculty of Pharmacy, Ağrı İbrahim Çeçen University, Ağrı, Turkey*
[*] *Corresponding author: seda.yuksekdanaci@usak.edu.tr*

Changes have been observed in the amount of acetylcholine (ACh), which acts as a neuro mediator in the brain tissues of patients with AD [4]. Inhibitors of AChE/BChE, which hydrolyze and control the concentrations of these neuro mediators, have therefore become a valid option in the treatment of AD [2,5,6]. Because of this situation, many researchers around the world, have tried to identify new inhibitor candidates for these enzymes that appear as targets in AD treatment. AChE regulates the concentration of ACh, which is known to have a critical role in cognition and memory in humans [5]. Because of the loss of cholinergic neurons in AD, the inhibition of cholinesterases, which can hydrolyze ACh, has been adopted as a treatment strategy to increase this decrease in the amount of ACh. Since they act as AChE inhibitors, drugs such as neostigmine, tacrine and donepezil are used in the treatment of AD [5,7,8].

CAs are a class of metalloenzymes that catalyze the rapid hydration of CO_2 into bicarbonate and proton [9]. Since CAs contribute to important biological processes (Ensuring intracellular and extracellular ion balance, regulation of intracellular pH, calcification, resorption, etc.) in living organisms, they are found in the structure of many tissues [10-12]. Since they can regulate these biological processes, CA inhibitors and activators are used in glaucoma, edema, cancer, epilepsy, some cognitive disorders, etc. They are candidate drug molecules to be used in the treatment of diseases [13-18].

Oxidative stress has been cited as one of the causes for AD pathology. An increase in the concentration of intracellular reactive nitrogen and oxygen species can cause oxidative damage to many biomolecules. Modifications that occur in proteins due to oxidative damage can also change the catalytic activities of enzymes [19]. For example, a reduction in CA activity and a number of highly nitrated and/or carbonylated proteins, including hCA II, were observed in the hippocampus of individuals with AD and human brain samples from mild cognitive brain samples [20-21]. Moreover, the fact that hCA II isoenzyme has been identified among a large number of amyloid plaques suggests that it may play a pivotal role in plaque development or may occur together with plaque formation [22]. The high levels of hCA II found in the central [20,23] and peripheral systems [24] also raise the possibility that hCA II expression may represent a biomarker for AD [12]. In addition, promising preclinical evidence of the use of CAIs (CA inhibitors) in amyloidosis models has also been reported lately [25].

Benzimidazole is the heterocyclic compound formed by the fusion of imidazole and benzene. Benzimidazole derivatives are of broad interest due to their diverse biological activities. Several benzimidazole derivatives have been published to exhibit marked antifungal, antibacterial, antioxidant, antiparasitic, antihelmintics, antiproliferative, anti-HIV activities [26-31]. Moreover benzimidazole derivatives are considered as a new promising molecules for Alzheimer inhibitör [32-35].

As excellent intermediates, glucosyl isothiocyanates have been used to prepare various carbohydrate compounds of biological and pharmaceutical interest [36, 37]. In recent years, there have been many studies on synthesizing glycosyl isothiocyanates and their transformation into glycosyl thiourea derivatives. Furthermore, sugar thioureas have synthetic applications in neoglycoconjugate synthetic strategies such as neoglycoproteins, glycodendrimers, glycoclusters and pseudooligosaccharides [38]. In addition, studies have shown that glycosyl derivatives, just like benzimidazoles, have anticholinesterase activity [39-41].

There is a limited number of publications on the synthesis and biological activity of glycosyl thioureas with benzimidazole structure. So, in this paper, a new series of chiral benzimidazole-glycosyl thiourea derivatives (**5-10**) were synthesized and the structures of the compounds were verified by FTIR, ^{1}H-NMR, ^{13}C-NMR, and elemental analysis. After synthesizing and characterizing chiral benzimidazole-glycosyl thiourea derivatives (**5-10**), the inhibitory effects on two hCA isoenzymes (hCA I/hCA II) and commercially obtained AChE and BChE enzymes were investigated in this study.

RESULTS AND DISCUSSION

Chemistry

The syntheses of the chiral benzimidazole compounds were made according to the literature (**4a-c**) [42]. The three different amino acids (L-isoleucine, D-phenylglycine, L-phenylalanine) were reacted with sodium bicarbonate and di-*tert*-butyl dicarbonate in H_2O/THF solvent system in order to obtain *N*-Boc protected amino acids (**1a-c**). Then the amide derivatives (**2a-c**) were obtained from compounds **1a-c** by using *o*-phenylenediamine (OFD) and *N*,*N'*-dicyclohexylcarbodiimide (DCC) under N_2 atm for 24 hours [43]. Compounds **3a-c** were synthesized by the reaction of chiral amides (**2a-c**) with acetic acid at 70 °C. In the last step, *N*-protected benzimidazole derivatives (**3a-c**) were reacted with phosphoric acid in THF at room temperature for 24 h obtaining benzimidazole derivatives(**4a-c**) (Scheme 1).

The second part of the study follows the synthesis of glycosylated isothiocyanates. Selected sugars were reacted with sodium acetate and acetic anhydride to obtain monosaccharide acetates [44]. Glycosyl bromides were synthesised following the reaction of acetylated monosaccharides with HBr-AcOH (33%) solution [45]. This follows the synthesis of glycosyl isothiocyanates by the reaction of glycosyl bromides with lead(II) thiocyanate in dry xylene under N_2 atmosphere [46].

To obtain the biologically active target compounds, benzimidazole-glycosyl thiourea derivatives (**5-10**), benzimidazole derivatives (**4a-c**) were reacted with gylcosyl isothiocyanates in acetone at room temperature for 24 hours (Scheme 2). The yield of the reactions ranged from 45 % to 73 %.

The molecular structures of the newly synthesized thiourea compounds were proved by FTIR, ^{1}H-NMR, ^{13}C-NMR and elemental analysis methods. Accordingly, the FTIR results observed for the synthesized compounds showed C-N stretching vibrational bands at 1224-1260 cm^{-1}, C=S stretching stretching vibrational bands at 1360-1380 cm^{-1}, C=O stretching stretching vibrational bands at 1748-1770 and N-H stretching stretching vibrational bands at 3330-3350 cm^{-1}.

In the ^{1}H-NMR spectral data, the signals observed at 1.74-2.11 ppm ascertain the presence of acetyl groups with 12 protons. The sugar protons' signals have been observed at 4.00-6.10 ppm for the synthesised benzimidazole-glycosyl thiourea derivatives (**5-10**). The signals observed at 6.85-8.81 ppm belong to aromatic protons in all structures.

In the ^{13}C-NMR of the target compounds (**5-10**), the carbon-sulfur double bond signals were observed at about 183 ppm, and the carbon-oxygen double bond signals at about 170 ppm. The carbons in sugar have shown signals at 60-80 ppm, and the signal at about 20 ppm indicates the presence of –CH$_3$ carbons in the acetyl groups.
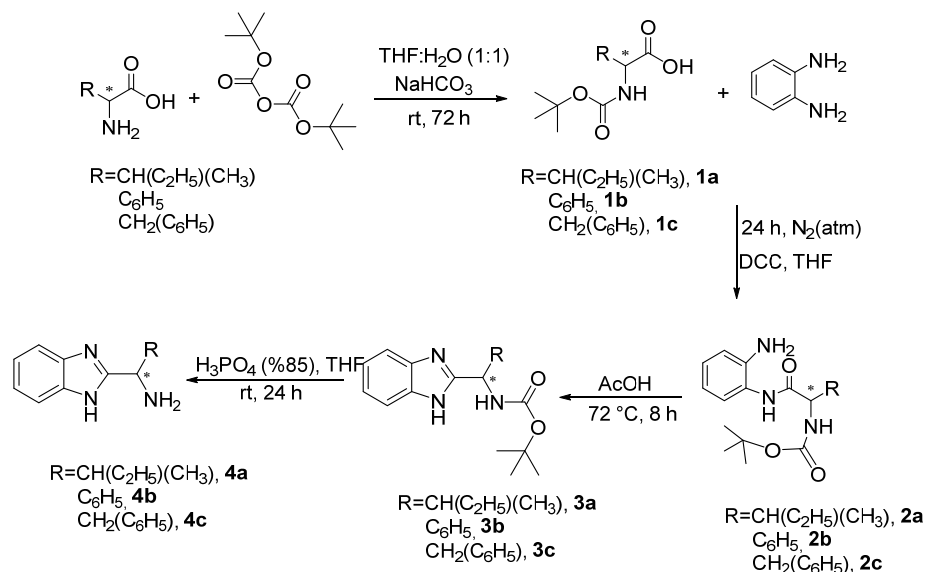
Scheme 1. Synthesis of benzimidazole derivatives (**4a-c**)
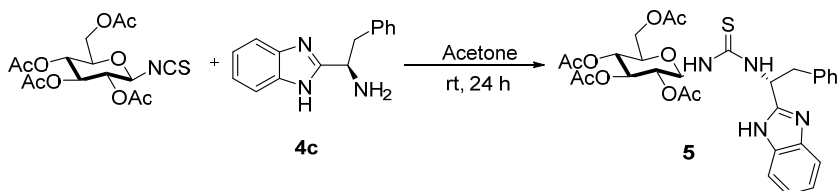
**Scheme 2.** Synthesis of benzimidazole-glycosyl thiourea compound

Biochemical Studies

This study reported on the synthesis of benzimidazoles (**5-10**). This study also determined the inhibition effects of the derivatives **5-10** on hCA I and hCA II enzymes activity.

It has been determined that AChE has essential functions in both cognition and memory. These cholinergic enzymes (AChE/BChE) catalyze the hydrolysis of ACh, causing a decrease in the level of neuronal communication of nerve cells with each other. This can lead to decreased brain function and, ultimately, to AD. Therefore, balancing the intracellular level of ACh can be used in treating AD [10-12, 14]. Numerous scientific studies have shown that inhibitors of cholinesterase enzymes (ChEIs) can be used in the treatment of neurodegenerative diseases. Currently, new ChEIs are being tried to be determined because of the low bioavailability of drugs used to treat AD and their gastrointestinal disturbances. In addition, studies conducted in recent years have shown that it can be used in CAIs, especially in the treatment of AD [11-17].

In this study, both CA and cholinesterase inhibitory potentials of **5-10** derivatives were investigated. As a result of this study, predictive models were also proposed for the substances with the most effective inhibitory effect for their interactions with hCA II and AChE enzymes, which are the primary targets in AD treatment (Figure 1).

In this study, the inhibitory effects of **5-10** benzimidazole derivatives (Figure 2) are reported for the first time using the p-nitrophenyl acetate substrate (esterase activity) of these hCA isozymes.
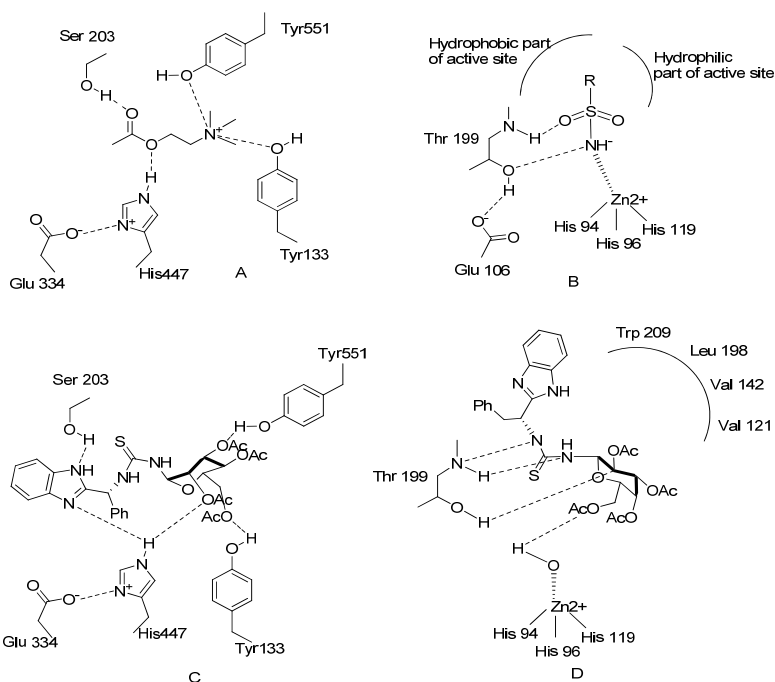
Figure 1. A: The interaction image of AChE enzyme and ACh [47], B: The binding image of hCA II enzyme and sulfonamide molecule [48, 49]. C: Estimated interaction image of AChE and compound 9. D: Estimated interaction image of hCA II and compund 8.
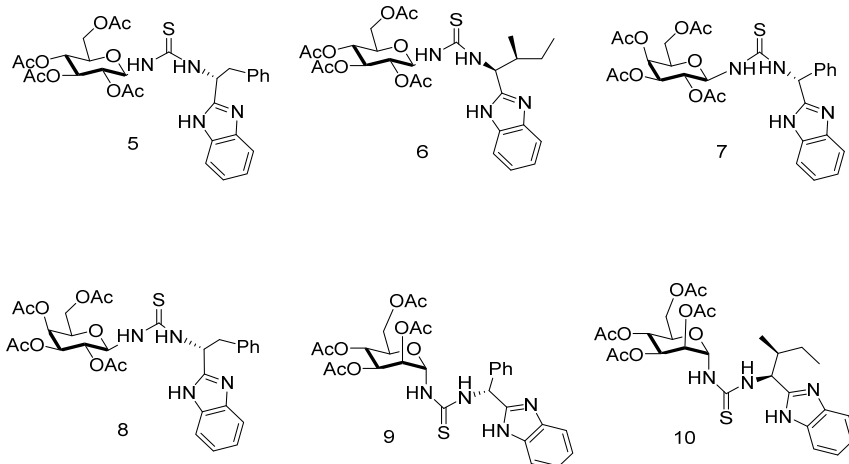
Figure 2. Benzimidazole-sugar compounds **5**-**10** Inhibition data for hCA I and hCA II measured using the esterase activity of these benzimidazole derivatives are shown below (Table 1):

Table 1. hCA I, hCA II, AChE and BChE inhibition
data benzimidazole derivatives **5-10**

	K_I / nM			
Inhibitor	hCA I	hCA II	AChE	BChE
5	7.57 ± 0.15	42.98 ± 0.65	16.59 ± 0.11	39.14 ± 0.43
6	6.65 ± 0.13	30.03 ± 0.51	8.71 ± 0.09	24.36 ± 0.27
7	11.33 ± 0.24	34.45 ± 0.54	11.73 ± 0.10	33.08 ± 0.35
8	13.82 ± 0.28	27.53 ± 0.32	5.32 ± 0.07	18.73 ± 0.19
9	9.56 ± 0.19	17.29 ± 0.29	12.20 ± 0.11	35.17 ± 0.38
10	6.03 ± 0.10	21.44 ± 0.30	8.36 ± 0.09	25.34 ± 0.27
Acetazolamide (AZA)	250 ± 0.52	12.0 ± 0.21	-	-
Donepezil	-	-	13.82 ± 0.18	2176 ± 23.1

(i) In inhibition experiments with the human CA I enzyme for benzimidazole derivative **5-10**, K_I values in the range of 6.03 ± 0.10-13.82 ± 0.28 nM were obtained. This study determined that compounds **5**, **6** and **10** followed a better inhibition profile than **7-9**. It has been determined that the **5-10** benzimidazole compounds examined show similar values with many previous studies (bromophenols, sulfonamide derivatives of amino acids, polyphenolic compounds, etc.) [7,12-18, 50].

(ii) It was observed that the K_I values obtained in inhibition experiments with benzimidazole derivative **5-10** for the hCA II enzyme were lower than that of the hCA I enzyme (Table 1). When the structure-activity evaluation for hCA II was made with the benzimidazole derivatives tested: we determined that compounds **5** and **6**, which contain methyl and benzyl groups as functional groups, are less effective than the other compounds. The best hCA II inhibitor among **5-10** derivatives is **9** containing the phenyl group in its structure, and the K_I of this substance was determined as 17.29 ± 0.29 nM.

(iii) Derivative **5** (K_I=16.59 ± 0.11 nM) showed the weakest inhibitory effect in the **5-10** agents against the AChE enzyme. When we look at the results of the inhibition obtained with the AChE enzyme for compounds **5-10**, compound **8** shows the best inhibition (K_I=5.32 ± 0.07 nM) and the compound **5** has the lowest inhibition value (K_I=16.59 ± 0.11 nM). This shows that the AChE enzyme interacts with the sugar group. Molecules **7** (K_I=11.33 ± 0.24 nM) and **9** (K_I =12.20 ± 0.11 nM) contain the same functional groups. The difference between these molecules is the position of the acetyl and thiourea groups in the molecule, and this effect has little effect on the inhibition values.

Molecules **6** (K_I=8.71 ± 0.09 nM) and **10** (K_I=8.36 ± 0.09 nM) contain the same functional groups. The difference between these molecules is the position of the acetyl, ethyl and thiourea groups in the molecule, and this effect has little effect on the inhibition values. Considering the K_I results obtained for benzimidazole derivatives **5-10** and AChE, it shows that the position of different functional groups in the molecule does not have a large effect on the inhibition values in general. The values obtained for AChE (5.32 ± 0.07-16.59 ± 0.11 nM) with the tested substances were lower and more effective when compared to the reference molecule donepezil (13.82 ± 0.18 nM).

(iv) Similar to the AChE enzyme, the weakest inhibitory effect of the six tested substances was determined in compound **5** (K_I=39.14 ± 0.43 nM) in the BChE enzyme. Among these six substances tested, the most potent inhibitor for the BChE enzyme appears to be compound **8** (K_I=18.73 ± 0.19 nM). The results of this study are essential in terms of showing that the BChE enzyme interacts with molecules derived from sugar groups, such as the AChE enzyme. Compound **7** (K_I=33.08 ± 0.35 nM) and **9** (K_I=35.17 ± 0.38 nM) contain the same functional groups. The difference between these molecules is the configuration of the acetyl and thiourea groups within the molecule, and this effect had little effect on the inhibition values. Molecules **6** (K_I=24.36 ± 0.27 nM) and **10** (K_I=25.34 ± 0.27 nM) contain the same functional groups. The difference between these molecules is the position of the acetyl, ethyl and thiourea groups in the molecule, and this effect has little effect on the inhibition values. According to these K_I results obtained for the BChE and its **5-10** benzimidazole derivatives, the position of the groups in the molecule generally shows that it does not have a significant effect on the inhibition value. Moreover, when the values obtained for the BChE (18.73 ± 0.19-39.14 ± 0.43 nM) in our study are compared to the reference molecule donepezil (2176 ± 23.1 nM), it is seen that they are much more effective.

In the inhibition studies carried out by different groups in the last twenty years, it has been discovered that they can show inhibition effects as well as sulfonamides, which are known as potent inhibitors of CA isoenzymes in the multi-bear functional group [12-18]. While this enables the detection of CA inhibitors that do not contain sulfonamide functional groups, it may also be advantageous in treating patients allergic to sulfonamide-derived drugs [13-18]. In some studies conducted in the last decade, it has been stated that hCA II inhibitors have positive effects in studies on AD models and can be used in the treatment of this disease [11,23]. In this study, both hCA isoenzymes and cholinesterase inhibition profiles of newly synthesized benzimidazole derivative (**5-10**) molecules were determined and their potential to be used in neurodegenerative diseases was tried to be determined.

CONCLUSIONS

It was determined that the synthesized benzimidazole-thiourea derivatives **5-10**, showed a compelling inhibition profile of both hCA isoenzymes and cholinesterase enzymes due to the functional groups (ethyl, acetyl, phenyl, benzyl and benzimidazole) in the structures. The findings indicate that these derivatives have inhibition values close to sulfonamides, so that they may be a new CAI class. In addition, inhibition values close to donepezil, the reference molecule, were obtained and determined to be an influential cholinesterase inhibitor group. It was determined by the esterase method that these benzimidazole derivatives obtained were effective CAIs even at nanomolar concentrations. The results of the study are essential in that these benzimidazole derivatives show that other hCA isoforms have the potential to produce strong CAI groups.

If we look at the findings, it shows that chiral benzimidazole-glycosyl thiourea derivatives (**5**-**10**) are potent inhibitors of the enzymes tested. As a result, it has been determined that this new inhibitor group we have identified has the potential to be a drug precursor or drug in treating AD. Comparison of benzimidazole derivatives (**5**-**10**) tested on CAs and cholinesterase enzymes here with current drug inhibitors and other compounds studied in the literature will help further expand the objectives for understanding the structure-activity relationship. These substances can also be used as building blocks in the determination of more effective drugs compared to known drug molecules.

EXPERIMENTAL SECTION

Synthesis of Benzimidazole compounds

The synthesis was essentially according to the amide formation procedure. L-isoleucine, D-phenylglycine and L-phenylalanine were selected as the starting amino acids.

Synthesis of Glycosyl Isothiocyanate

The glycosyl isothiocyanate derivatives can be easily synthesized from the corresponding sugars [51-53]. D-glucose, D-galactose and D-mannose were selected as the starting sugars.

General procedure for the synthesis of benzimidazole-containing gylcosyl thiourea derivatives (5-10)

The chiral benzimidazole compound (10 mmol) was dissolved in 15 mL of acetone under inert atmosphere. Glycosyl isothiocyanate (10 mmol) was added to the solution, and it was stirred at room temperature for 24 hours.

After the termination of the reaction, acetone was evaporated under reduced pressure. The remaining solid was crystallized from the CH_2Cl_2 / Hexane system to give the pure product.

N-[(R)-1-(1H-benzo[d]imidazol-2-yl)-2-phenylethyl)]-N-(2,3,4,6-tetra-O-acetyl-β-D-glucopyranosyl)thiourea (5)

White solid, 73 % Yield, M.P. = 137-140 °C, IR (NaCl, cm^{-1}): 3330, 3029, 2942, 1752 1534, 1439, 1368, 1226, 1038, 739. ^{1}H NMR (400 MHz, CDCl$_3$, ppm): δ= 1.94 (s, 3H, OCH$_3$); 1.95 (s, 3H, OCH$_3$); 1.97 (s, 3H, OCH$_3$); 1.99 (s, 3H, OCH$_3$); 3.28 (d, J= 8.0 Hz, 1H, CH-CH$_{2a}$-Ar); 3.42 (dd, J= 4.0 Hz, 1H, CH-CH$_{2b}$-Ar); 3.86 (t, J= 12.0 Hz, 1H, H$_5$); 4.14-4.08 (m, 2H, H$_{6b}$, H$_4$); 4.27 (dd, J=8.0 Hz, 1H, H$_{6a}$); 4.90 (m, 1H, H$_3$); 5.02 (t, J=8.0 Hz, 1H, H$_2$); 5.28 (q, J= 6.2 Hz, 1H, NH-CH-CH$_2$); 5.85 (bs, 1H, NH); 6.08 (s, 1H, H$_1$); 6.94 (m, 5H, Ar-H); 7.19 (m, 2H, Ar-H); 7.46 (m, 2H, Ar-H); 7.83 (bs, 1H, NH); 8.81 (bs, 1H, NH). ^{13}C NMR (100 MHz, CDCl$_3$, ppm): δ= 182.42; 171.40; 170.38; 170.00; 169.67; 136.28; 129.34; 128.89; 128.00; 127.14; 126.52; 124.51; 83.25; 72.36; 70.72; 68.82; 67.08; 60.99; 56.63; 38.24; 20.80; 20.66; 20.57; 20.50. Anal. Calcd for $C_{30}H_{34}N_4O_9S$: C, 57.50; H, 5.47; N, 8.94; S, 5.12. Found: C, 55.30; H, 5.41; N, 8.91; S, 5.12.

N-[(1S,2S)-1-(1H-benzo[d]-imidazol-2-yl)-2-methylbutyl]-N-(2,3,4,6-tetra-O-acetyl-β-D-glucopyranosyl)thiourea (6)

White solid, 45 % Yield, M.P. = 178-180 °C, IR (NaCl, cm^{-1}): 3350, 2963, 1752, 1541, 1366, 1226, 1038, 733. ^{1}H NMR (400 MHz, CDCl$_3$, ppm): δ= 0.80 (app. t, J= 6.5 Hz, 3H, CH$_2$CH$_3$); 0.87 (d, J= 6.4 Hz, 3H, CHCH$_3$); 1.18-1.21 (m, 2H, CHCH$_2$CH$_3$); 1.96 (s, 3H, OCH$_3$); 2.00 (s, 3H, OCH$_3$); 2,01 (s, 3H, OCH$_3$); 2.02 (s, 3H, OCH$_3$); 3.85-3.82 (m, 1H, CH$_3$CHCH$_2$); 4.12 (app. d, J= 9.8 Hz, 1H, H$_5$); 4.29 (app. d, J= 9.8 Hz, 1H, H$_{6a}$); 4.88 (s, 1H, H$_4$); 5.02 (t, J= 8 Hz, 2H, H$_{6b}$+H$_3$); 5.32 (t, J= 9.4 Hz, 1H, NH-CH-CH); 5.48 (s, 1H, H$_2$); 5.68 (s, 1H, H$_1$); 7.23 (s, 2H, Ar-H); 7.41 (s, 1H, Ar-H); 7.56 (s, 2H, Ar-H); 8.12 (bs, 1H, NH). ^{13}C NMR (100 MHz, CDCl$_3$, ppm): δ= 183.86; 170.88; 170.62; 169.83; 169.49; 154.20; 122.96; 122.92; 122.90; 122.86; 82.74; 73.44; 72.78; 70.96; 68.25; 61.73; 57.60; 25.48; 20.66; 20.53; 20.49; 20.33; 15.79; 10.55. Anal. Calcd for $C_{27}H_{36}N_4O_9S$: C, 54.72; H, 6.12; N, 9.45; S, 5.41. Found: C, 55.69; H, 6.14; N, 9.45; S, 5.38.

N-[(R)-1-(1H-benzo[d]imidazol-2-yl)(phenyl)methyl]-N-(2,3,4,6-tetra-O-acetyl-β-D-galactopyranosyl)thiourea (7)

White solid, 54 % Yield, M.P: = 138-140 °C, IR (NaCl, cm^{-1}): 3334, 3060, 1748, 1591, 1455, 1430, 1370, 1225, 1050, 914. ^{1}H NMR (400 MHz,

CDCl$_3$, ppm): δ= 1.91 (s, 3H, OCH$_3$); 1.96 (s, 3H, OCH$_3$); 2.02 (s, 3H, OCH$_3$); 2.11 (s, 3H, OCH$_3$); 4.07 (d, *J*= 8.6 Hz, 3H, H-6a+H-6b+H-5); 4.20-4.16 (m, 1H, H-2); 5.15 (s, 1H, NH-CH-Ar); 5.23 (t, *J*= 9.0 Hz, 1H, H-3); 5.44 (dd, *J*= 9.6 Hz, *J*= 3.0 Hz, 1H, H-4); 5.65 (s, 1H, H-1); 6.94 (bs, 1H, NH); 7.15-7.21 (m, 4H, Ar-H); 7.35 (d, *J*= 7.1 Hz, 3H, Ar-H); 7.45 (s, 2H, Ar-H); 8.35 (bs, 1H, NH); 8.59 (bs, 1H, NH). ^{13}C NMR (100 MHz, CDCl$_3$, ppm): δ= 183.59; 171.12; 170.70; 170.44; 170.13; 169.75; 153.02; 137.97; 128.89; 128.85; 128.42; 128.29; 127.71; 127.45; 122,95; 83.12; 72.16; 70.98; 68.36; 67.29; 60.90; 56.80; 20.70; 20.59; 20.53; 20.48. Anal. Calcd for C$_{29}$H$_{32}$N$_4$O$_9$S: C, 56.85; H, 5.26; N, 9.14; S, 5.23. Found: C, 56.89; H, 5.23; N, 9.11; S, 5.21.

N-[(*R*)-1-(1*H*-benzo[d]imidazol-2-yl)-2-phenylethyl]-*N*-(2,3,4,6-tetra-*O*-acetyl-β-D-galactopyranosyl)thiourea (8)

White solid, 48 % Yield, M.P. = 142-145 °C, IR (NaCl, cm^{-1}): 3330, 3030, 1770, 1520, 1380, 1260, 740. ^{1}H NMR (400 MHz, CDCl$_3$, ppm): δ= 1.95 (s, 3H, OCH$_3$); 1.96 (s, 3H, OCH$_3$); 2.02 (s, 3H, OCH$_3$); 2.05 (s, 3H, OCH$_3$); 3.41-3.48 (m, 2H, CH-CH$_2$-Ar); 4.02-4.06 (m, 3H, H-6a+H-6b+H-5); 4.12-6.12 (5H, H-1+H-2+H-3+H-4+NH-CH-CH$_2$); 5.60 (bs, 1H, NH); 6.85 (bs, 1H, NH); 7.05 (app d, *J*= 8.2 Hz, 1H, Ar-H); 7.13 (app d, *J*= 7.2 Hz, 2H, Ar-H); 7.17 (s, 1H, Ar-H); 7.19-7.23 (m, 3H, Ar-H); 7.49 (s, 2H, Ar-H); 7.90(bs, 1H, NH). ^{13}C NMR (100 MHz, CDCl$_3$, ppm): δ=183.44; 171.08; 170.52; 170.03; 169.70; 155.89; 153.43; 136.43; 129.13; 128.60; 126.90; 122.99; 82.92; 72.35; 70.87; 68.35; 67.15; 61.17; 53.88; 38.79; 20.63; 20.59; 20.48; 20.47. Anal. Calcd for C$_{30}$H$_{34}$N$_4$O$_9$S: C, 57.70; H, 5.47; N, 8.94; S, 5.12. Found: C, 57.74; H, 5.48; N, 8.96; S, 5.11.

N-[(*R*)-1-(1*H*-benzo[d]imidazol-2-yl)(phenyl)methyl]-*N*-(2,3,4,6-tetra-*O*-acetyl-α-D-mannopyranosyl)thiourea (9)

White solid, 71 % Yield, M.P. = 151-154 °C, IR (NaCl, cm^{-1}): 3335, 2960, 1752, 1550, 1360, 1225, 1032, 743. 1H NMR (400 MHz, CDCl3, ppm): δ= 1.93 (s, 3H, OCH$_3$); 1.94 (s, 3H, OCH$_3$); 1.98 (s, 3H, OCH$_3$); 2.00 (s, 3H, OCH$_3$); 3.94 (app d, *J*= 9.2 Hz, 1H, H-5); 4.02 (d, *J*= 11.4 Hz, 1H, H-6a); 4.08-4.13 (m, 1H, H-6b); 4.31 (dd, *J*= 12.2 Hz, *J*= 3.6 Hz, 1H, H-4); 5.06-5.25 (3H, H-2+H-3+NH-CH-Ar); 5.34 (s,1H, H-1); 5.93 (bs, 1H, NH); 7.17-7.21 (m, 4H, Ar-H); 7.32 (d, *J*= 3.8 Hz, 2H Ar-H); 7.41 (s, 3H Ar-H); 7.86 (bs, 1H, NH); 8.23 (bs, 1H, NH). ^{13}C NMR (100 MHz, CDCl$_3$, ppm): δ=183.58; 170.89; 170.80; 169.81; 169.41; 129.06; 128.99; 128.55; 127.87; 127.59; 123.13; 80.46; 69.69; 69.18; 69.04; 66.05; 61.95; 56.93; 20.74; 20.66; 20.64; 20.47. Anal. Calcd for C$_{29}$H$_{32}$N$_4$O$_9$S: C, 56.85; H, 5.26; N, 9.14; S, 5.23 Found: C, 56.80; H, 5.24; N, 9.15; S, 5.25.

N-[(1S,2S)-1-(1H-benzo[d]imidazol-2-yl)-2-methylbutyl)]-N-(2,3,4,6-tetra-O-acetyl-α-D-mannopyranosyl)thiourea (10)

White solid, 53 % Yield, M.P. = 149-151 °C, IR (NaCl, cm^{-1}): 3340, 2965, 1752, 1534, 1367, 1224, 1052, 749. 1H NMR (400 MHz, CDCl3, ppm): δ= 0.94 (d, J= 6.7 Hz, 6H, 2xCH$_3$); 1.29-1.37 (m, 2H, CH-C$\underline{H}_2$-CH$_3$); 1.64-1.69 (m, 1H, CH$_3$-C$\underline{H}$-CH$_2$) 1.97 (s, 6H, 2XOCH$_3$); 2.02 (s, 3H, OCH$_3$); 2.13 (s, 3H, OCH$_3$); 3.42-3.46 (m, 1H, H-5); 4.00 (s, 1H, H-6a); 4.08 (s, 1H, H-6b); 4.38 (d, J= 9.5 Hz, 1H, H-4); 5.12-5.41 (3H, H-3+H-1+NH-C$\underline{H}$-CH-CH$_3$); 5.68 (s, 2H, H-1+ NH); 7.21-7.23 (m, 2H, Ar-H); 7.41 (s, 2H, Ar-H); 7.67 (s, 1H, Ar-H); 8.52 (bs, 1H, NH). ^{13}C NMR (100 MHz, CDCl$_3$, ppm): δ= 183.19; 170.69; 169.95; 169.89; 169.39; 156.97; 133.05; 122.77; 119.96; 118.69; 111.59; 80.76; 70.05; 69.02; 68.65; 65.63; 61.74; 58.38; 33.81; 24.83; 20.77; 20.69; 20.61; 20.56; 15.72; 10.90. Anal. Calcd for C$_{27}$H$_{36}$N$_4$O$_9$S: C, 54.72; H, 6.12; N, 9.45; S, 5.41 Found: C, 54.70; H, 6.12; N, 9.43; S, 5.40.

Purification of human erythrocytes CA isozymes

Erythrocyte cells were purified using fresh human blood from Atatürk University Research Hospital Blood Center. Plasma and buffy coat were removed by centrifugation for ten minutes using a cooled centrifuge at 2000 rpm by taking 10 mL from the blood collected. The erythrocytes were separated and washed three times with 0.9% NaCl and hemolyzed with two volumes of ice-cold water. It was centrifuged again at 10000 rpm for 30 minutes. The pH of the resulting hemolysate was adjusted to 8.7 with solid Tris. The hemolysate was applied to the prepared Sepharose 4BL-aniline-sulfanilamide affinity column equilibrated with 25 mM Tris-HCl/0.1 M Na$_2$SO$_4$ (pH 8.7). The affinity gel was washed with 25 mM Tris-HCl / 22 mM Na$_2$SO$_4$ (pH 8.7). The human carbonic anhydrase (hCA-I and hCA-II) isoenzymes were washed with 1 M NaCl / 25 mM Na$_2$HPO$_4$ (pH 6.3) and 0.1 M CH$_3$COONa / 0.5 M NaClO$_4$ (pH 5.6), respectively. All procedures were performed at 4°C [14-17].

Biological activities for hCA I, hCA II, AChE and BChE

The Ellman method investigated the inhibitory activities between the synthesized benzimidazole derivatives (**5-10**) and cholinesterase enzymes [54]. Ellman's method is an in vitrobiological assay that is based on the reaction of thiocholine with DTNB to form 5-mercapto-2-nitrobenzoicacid (yellow compound). The yellow color can be quantified by its absorbance at 412 nm. First, 1 mg of each inhibitor was dissolved in 1 mL DMSO and then diluted to various concentrations with deionized water. To determine the cholinesterase inhibition activity, six serial dilutions of the inhibitors were measured. The

reaction system was composed of 5-60 µL inhibitor sample, 200 µL buffer (1 M, pH 8.0: Tris-HCl buffer for the AChE assay and phosphate buffer for the BChE assay), 50 µL DTNB (0.5 mM), 50 µL acetylthiocholine iodide/S-butyrylthiocholine chloride (10 mM) and 10 µL enzyme (0.28 units/mL for the AChE assay and 0.32 units/mL for the BChE assay). The reaction was initiated upon addition of the enzyme. The reaction system was prepared at room temperature in a quartz cuvette. The blank reading was composed of all chemicals except the inhibitör. The absorbance of the reaction mixture was measured at 412 nm within 5 minutes from the start of the reaction on a ThermoScientific Evolution 200 Series UV-VIS spectrophotometer. The absorbance for each reaction mixture was measured three times within 5 minutes of adding the enzyme, and the results are reported as mean ± standard deviation.

Carbonic anhydrase (hCA I and II) activity was assayed by following the change in absorbance at 348 nm of 4-nitrophenylacetate (NPA) to 4-nitrophenylate ion over a period of 3 min at 25 °C using a spectrophotometer (CHEBIOS UV–VIS) according to the method described by Verpoorte et al [55]. The enzymatic reaction, in a total volume of 3.0 mL, contained 1.4 mL of 0.05 M Tris–SO4 buffer (pH 7.4), 1 mL of 3 mM 4-nitrophenylacetate, 0.5 mL H2O and 0.1 mL enzyme solution. A reference measurement was obtained by preparing the same cuvette without enzyme solution. The inhibitory effects of synthesized compounds (**5-10**) and acetazolamide were examined. Donepezil for cholinesterases and acetazolamide for hCA isoenzymes were used as reference inhibitors. Each substance tested was assayed in at least three replicates for each concentration. Measurements were made for all these derivatives at different concentrations. The activity in the measurement (control) without inhibitor was accepted as 100%. % Activity-[Inhibitor] graphs are drawn for the substances tested. Measurements were made for all these derivatives (**5-10**) at different concentrations. The IC_{50} values determined for benzimidazole derivatives are shown in Table 1. Stock solutions of all substances used in the study were prepared as 1 mg/mL (using dimethylsulfoxide). The prepared stock solutions were diluted with distilled water at different concentrations. Six serial dilutions of these derivatives using distilled water were measured to determine the inhibitory activity of all the enzymes tested. This study used in the previous work [56]. The prepared stock solutions were diluted with distilled water at different concentrations**.**

REFERENCES

1. J. D. Ulrich; D. M. Holtzman; *ACS Chem. Neurosci.*; **2016**; *7*; 420-427.
2. L. S. Schneider; *Clinics in Geriatric Medicine*; **2001**; *17*; 337-358.
3. A. V. Terry; J. J. Buccafusco; *J Pharmacol Exp. Ther.*; **2003**; *306*; 821-827.
4. M. R. Picciotto; M. J. Higley; Y. S. Mineur; *Neuron*; **2012**; *76*; 116-129;
5. P. Bar-On; C. B. Millard; M. Harel; H. Dvir; A. Enz; L. Sussman; I. Silman; *Biochemistry*; **2002**; *41*; 3555-3564.
6. F. Comert Onder; K. Sahin; M. Senturk; S. Durdagi; M. Ay; *J. Mol. Graph. Modell*; **2022**; *115*; 108210.
7. M. Ozil; H. T. Balaydin; M. Senturk; *Bioorganic Chemistry*; **2019**; *86*; 705-713.
8. R. Cakmak; E. Basaran; M. Senturk; *Arch. Pharm.*; **2022**; *355*; e2100430.
9. C. T. Supuran; *Nat. Rev. Drug Discov.*; **2008**; 7; 168-181.
10. M. Hilvo; L. Baranauskiene; A. M. Salzano; A. Scaloni; D. Matulis; A. Innocenti; A. Scozzafava; S. M. Monti; A. Di Fiore; G. De Simone; *J. Biol. Chem.*; **2008**; *283*; 27799-27809.
11. G. Provensi; F. Carta; A. Nocentini; C. T. Supuran; F. Casamenti; M. B. Passani; S. Fossati; *Int. J Mol. Sci.*; **2019**; *20*; 4724.
12. S. Isik; D. Vullo; S. Durdagi; D. Ekinci; M. Senturk; A. Cetin; E. Senturk; C. T. Supuran; *Bioorg. Med. Chem. Lett.*; **2015**; *25*; 5636-5641.
13. T. Arslan; Z. Biyiklioglu; M. Senturk; *RSC Adv.*; **2018**; *8*; 10172-10178.
14. R. Yaseen; D. Ekinci; M. Senturk; A. D. Hameed; S. Ovais; P. Rathore; M. Samim; K. Javed; C. T. Supuran; *Bioorg. Med. Chem. Lett.*; **2016**; *26*; 1337-1341.
15. H. T. Balaydın; M. Senturk; A. Menzek; *Bioorg. Med. Chem. Lett.*; **2012**; *22*; 1352-1357.
16. I. Fidan; R. E. Salmas; M. Arslan; M. Senturk; S. Durdagi; D. Ekinci; E. Senturk; E. Cosgun; C. T. Supuran; *Bioorganic & Medicinal Chemistry*; **2015**; *23*; 7353-7358.
17. M. Guney; H. Cavdar; M. Senturk; D. Ekinci; *Bioorganic & Medicinal Chemistry Letters*; **2015**; *25*; 3261-3263.
18. S. Durdagi; N. Korkmaz; S. Işık; D. Vullo; D. Astley; D. Ekinci; R. E. Salmas; M. Senturk; C. T. Supuran; *Journal of Enzyme Inhibition and Medicinal Chemistry*; **2016**; *31*; 1214-1220.
19. D. A. Butterfield; T. Reed; S. F. Newman; R. Sultana; *Free Radic. Biol. Med.*; **2007**; *43*; 658-677.
20. R. Sultana; D. Boyd-Kimball; J. Cai; W. M. Pierce; J. B. Klein; M. Merchant; D. A. Butterfield; *J. Alzheimers Dis.*; **2017**; *11*; 156-164.
21. W. Meier-Ruge; P. Iwangoff; K. Reichlmeier; *Arch. Gerontol. Geriatr.*; **1984**; *3*; 161-165.
22. E. Drummond; S. Nayak; A. Faustin; G. Pires; R. A. Hickman; M. Askenazi; M. Cohen; T. Haldiman; C. Kim; X. Han; *Acta Neuropathol.*; **2017**; *133*; 933-954.
23. A. Pollard; F. Shephard; J. Freed; S. Liddell; L. Chakrabarti; *Aging*; **2016**; *8*; 2425-2436.
24. B. G. Jang; S. M. Yun; K. Ahn; J. H. Song; S. A. Jo; Y. Y. Kim; D. K. Kim; M. H. Park; C. Han; Y. H. Koh; *J. Alzheimers Dis.*; **2010**; *21*; 939-945.

25. F. Angiulli; M. E. Solesio; L. Debure; J. R. Cejudo; T. Wisniewski; S. Fossati; *Alzheimer's &Dement*; **2018**; *14*; 1296.
26. F. Fei; Z. Zhou; *Expert Opin. Ther. Pat.*; **2013**; *23*; 1157-1179.
27. Y. N. Wang; R. R. Y. Bheemanaboina; G. X. Cai; C. H. Zhou; *Inorg. Med. Chem. Lett.*; **2018**; *28*; 1621-1628.
28. Z. Wang; X. Deng; S. Xiong; R. Xiong; J. Liu; L. Zou; *Nat. Product. Res.*; **2017**; *32*; 2900-2909.
29. G. R. Morais; E. Palma; F. Marques; L. Gano; M. C. Oliveira; A. Abrunhosa; *J. Heterocyclic Chem.*; **2017**; *54*; 255-267.
30. Y. Bansal; O. Silakari; *Bioorg. Med. Chem.*; **2012**; *20*; 6208-6236.
31. R. S. Keri; A. Hiremathad; S. Budagumpi; B. M. Nagaraja; *Chem. Biol. Drug Des.*; **2015**; *86*; 19-65.
32. Y. Fang; H. Zhou; Q. Gu; J. Xu; *Eur. J of Med. Chem.*; **2019**; *167*; 133-145.
33. G. Sarıkaya; G. Çoban; S. Parlar; A. H. Tarikogullari; G. Armagan, M. A. Erdoğan; V. Alptüzün; A. S. Alpan; *Arch Pharm Chem Life Sci.*; **2018**; *351*; 1800076-1800093.
34. L. Dinparast; G. Zengin; M. B. Bahadori; *Biointerface Research in Applied Chemistry*; **2021**; *11*; 10739-10745.
35. T. Kim; H. Y. Yang; B. G. Park; S. Y. Jung; J. Park; K. D. Park; S. J. Min; J. Tae; H. Yang; S. Cho; S. J. Cho; H. Song; I. Mook-Jung; J. Lee; A. N. Pae; *Eur. J of Med. Chem.*; **2017**; *125*; 1172-1192.
36. A. B. Reitz; R. W. Tuman; C. S. Marchione; A. D. Jordan; C. R. Jr Bowden; B. E. Maryanoff; *J. Med. Chem.*; **1989**; *32*; 2110-2116.
37. H. Parrot-Lopez; H. Galons; A. W. Coleman; J. Mahnteau; M. Miocque; *Tetrahedron Lett.*; **1992**; *33*; 209-212.
38. A. S. Dandale; D. V. Mangte; S. P. Deshmukh; *The 14th International Electronic Conference on Synthetic Organic Chemistry*; **2010**.
39. Y. Wu; S. Ren; L. Wang; Y. Wang; S. Liu; W. Liu; D. Shi; Z. Cao; *Journal of Chemical Research*; **2020**; *44*; 363-366.
40. L. Yin; F. Cheng; Q. Li; W. Liu; X. Liu; Z. Cao; S. Shi; *Journal of Chemical Research*; **2016**; *40*; 545-548.
41. L. Cao; K. Jiang; Z. Shao; Y. Wang; S. Liu; X. Lu; Y. Wu; C. Chen; Z. Su; L. Wang; W. Liu; D. Shi; Z. Cao; *Russian J of Org. Chem.*; **2021**; *57*; 1513-1518.
42. D. Shendage; R. Fröhlich; G. Haufe; *Org. Lett.*; **2004**; *6*; 3675-3678.
43. N. Korkmaz; O. A. Obaidi; M. Senturk; D. Astley; D. Ekinci; C. T. Supuran; *Journal of Enzyme Inhibition and Medicinal Chemistry*; **2015**; *30*; 75-80.
44. M. L. Wolfrom; *Methods in carbohydrate Chemistry*. London: Academic; New York; San Francisco; **1963**.
45. F. Weygard; H. Ziemann; H. J. Bestmann; *Chem. Ber.*; **1958**; *91*; 2534-2537.
46. Z. Shusheng; Z. Tianrong; C. Kun; X. Youfeng; Y. Bo; *Eur. J. Med. Chem.*; **2008**; *43*; 2778-2783.
47. T. L. Rosenberry; X. Brazzolotto; I. R. Macdonald; M. Wandhammer; M. Trovaslet-Leroy; S. Darvesh; F. Nachon; *Molecules*; **2017**; *22*; 2098-2119.
48. V. M. Krishnamurthy; G. K. Kaufman; A. R. Urbach; I. Gitlin; K. L. Gudiksen; D. B. Weibel; G. M. Whitesides; *Chem. Rev.*; **2008**; *108*; 946–1051.

49. C. A. Lesburg; C. Huang; D. W. Christianson; C. A. Fierke; *Biochemistry*; **1997**; *36*; 15780–15791.
50. T. Arslan; M. B. Ceylan; H. Baş; Z. Biyiklioglu; M. Senturk; *Dalton Transactions*; **2020**; *49*; 203-209.
51. J. M. G. Fernandez; C. O. Mellet; *Advances in Carbohydrate Chemistry and Biochemistry*; **2000**; *55*; 35-135.
52. L. J. Haynes; F. H. Newth; *Advances in Carbohydrate Chemistry*; **1995**; *10*; 207-256.
53. H. Osborn; *Carbohydrates*; 1st ed.; Academic Press; United Kingdom; **2003**.
54. G. L. Ellman; K. D. Courtney; V. Jr Andres; R. M. Featherstone*; Biochem. Pharmacol.*; **1961**; *7*; 91-95.
55. J. A. Verpoorte; S. Mehta; J. T. Edsall; *J. Biol. Chem.*; **1967**; *242*; 4221-4229.
56. K. Zilbeyaz; N. Stellenboom; M. Guney; A. Oztekin; M. Senturk M; *J Biochem. Mol. Toxicol.*; **2018**; *32*; e22210.

THERMODYNAMIC STUDY OF SOME ALCOHOLS IN DILUTE AQUEOUS SOLUTION

Wedad J. FENDI[a], Zainab Abbas AL-DULAIMY[a], Dheefaf F. HASSAN[a], Azhar Farooq ABDULZAHRA[a] and Husam Saleem KHALAF[a*]

ABSTRACT. An apparent molar volume ϕv of 1-pentanol, 1-hexanol, 1-heptanol, and 1-octanol in dilute aqueous solution has been particular for density measurements at 298.15 K. A restrictive apparent molar volumes ϕv° at infinite dilution of these compounds were investigated based on Masson's equation. Based on the Jone-Dole equation, A and B viscosity constants for four alcohols have been identified. This liquid offers resilient solute-solvent interaction. The modified Jone-Dole equation has also been employed with the experimental consequences using four liquids as solutes in dilute aqueous solutions.

Keywords: Alcohols, Apparent molar volume, Modified Jone-Dole equation.

INTRODUCTION

Several facts about serious water-solute interaction in solution chemistry have been based on the familiarity of apparent molar volume. Indeed, in extremely dilute aqueous solution, the dual features of apparent molar volume and viscosity were required to build up an understanding of inter-molecular interactions [1,2]. In this paper, our converge is about dilute aqueous solutions, that provide wide-ranging characteristics for the structures of the solution. Henceforth volumetric and viscometric investigations about these organic liquids were implemented in extremely dilute aqueous media [3-5].

[a] *Department of Chemistry, "Ibn-Al-Haitham" College of Education for Pure Science, University of Baghdad, Baghdad, Iraq.*
[*] *Corresponding author: husam.s.k@ihcoedu.uobaghdad.edu.iq*

WEDAD J. FENDI, ZAINAB ABBAS AL-DULAIMY, DHEEFAF F. HASSAN,
AZHAR FAROOQ ABDULZAHRA, HUSAM SALEEM KHALAF

Alcohols are feasibly taken into consideration as derivatives of water in which an alkyl group substitutes one hydrogen atom. The unshared electron in an oxygen outer shell conveys significant characteristics in the structure of the alcohols. Alcohols are water-like in their natural characteristics since their hydroxyl ratio in the C-H bonding has been raised. Numerous reported papers about volumetric properties had discussed numerous mixes of alcohols and water.

Alcohols are applied as solvents, co-solvents, alcohols-water mixtures, at all times, acting as attention- grabbing due to their anomalous performance like the maximum presence of a viscosity-composition and lower partial molar volume [6-8] than their volume in the "pure'' alcohol state [9-12]. Alcohols stand for industrial biological amphiphilic materials in a liquid state in accordance with the hydrogen bonding of their O-H clusters. They are self-associated and polar liquids, and they are of specific interest as alcohols are powerful liquids with a three-dimensional system of hydrogen bonds and can be connected with any other group taking several degrees of polar attraction [13-15]. Water molecules might be bound to the biological solvent in the widespread techniques. Alcohols remarkably vary from other biological solvents and from each other based on the degree and extent of self-association [16-18]. An important consideration was paid in the past for altering hydrogen-bonded structures of alcohol pure water in a mixing activity. Previously, the water-alcohol hydrogen bond was, in general, sturdier than the alcohol-alcohol bond. Introducing water into pure alcohols can collapse the self-association in alcohols. The new hydrogen bonds are feasibly made among water molecules and alcohols [19-21]. While explaining the volumetric properties of powerfully interconnected systems like alcohol-water combinations.

It is essential to adopt these consequences. Accordingly, we investigated, in this paper, the partial molar volume for water in several alcohols with the intention of providing a superior interpretation of these factors that contribute significantly to a volumetric performance of powerfully related mixtures [22,23]. The current work inspected experimental data of viscosities (η), and densities (ρ) at 298.15 K, for (1-pentanol, 1-hexanol, 1-heptanol, and 1-octanol) in dilute aqueous solutions which were used to calculate apparent molar volume (ϕv) and Jone-Dole coefficients.

RESULTS AND DISCUSSION

For all alcohols, 1-pentanol, 1-hexanol, 1-heptanol, and 1-octanol, the values under dissimilar concentrations in aqueous solution were perceived. The data for viscosity for each solute under dissimilar concentrations were employed to determine the interaction parameter in aqueous solution. The interaction parameters were obtained based on Jon-Dole's Eq. [24, 25].

$$(\eta/\eta_\circ - 1)/\sqrt{C} = A + B\sqrt{C} \ \text{........ (1)}$$

Here, A and B stand for the constants regarding ion-ion besides ion-solvent interaction correspondingly, while C stands for a molar concentration. The B magnitudes were acquired based on linear plots between $(\eta/\eta_\circ - 1)/\sqrt{C}$ and $\sqrt{C}$. These plots were depicted in Fig. 1. A and B coefficients were considered from the intercepts and slope for each biological material as specified in Table 1.

Table 1. A and B coefficient for aqueous 1-pentanol, 1-hexanol, 1-heptanol, and 1-octanol under 298.15 K based on Jone-Dole equation

1-Pentanol			1-Hexanol			1-Heptanol			1-Octanol		
S. no.	$\sqrt{C}$	$(\eta/\eta_o-1)/\sqrt{C}$	S. no.	$\sqrt{C}$	$(\eta/\eta_o-1)/\sqrt{C}$	S. no.	$\sqrt{C}$	$(\eta/\eta_o-1)/\sqrt{C}$	S. no.	$\sqrt{C}$	$(\eta/\eta_o-1)/\sqrt{C}$
1	0.19644	0.21507	1	0.20164	0.22776	1	0.21608	0.30998	1	0.24222	0.33496
2	0.22614	0.25108	2	0.22863	0.27785	2	0.24479	0.37821	2	0.28078	0.42552
3	0.26876	0.27805	3	0.27081	0.32189	3	0.28084	0.45296	3	0.31084	0.49166
4	0.30237	0.30863	4	0.31283	0.38898	4	0.31549	0.52559	4	0.34479	0.54626
5	0.34319	0.35785	5	0.33314	0.45326	5	0.33835	0.55329	5	0.36828	0.60984
6	0.36364	0.37625	6	0.36388	0.51145	6	0.37116	0.59611	6	0.39595	0.66435
7	0.39148	0.42231	7	0.39829	0.57651	7	0.39865	0.63933	7	0.42243	0.77332
8	0.42033	0.44948	8	0.42291	0.60763	8	0.42064	0.70802	8	0.44467	0.79493
9	0.43866	0.47522	9	0.44472	0.62554	9	0.43845	0.74498	9	0.46312	0.84831
10	0.45339	0.49896	10	0.46679	0.64587	10	0.47615	0.78227	10	0.48546	0.90922

In view of that, A= -0.008 (dm$^{3/2}$.mol$^{-1/2}$), A= -0.1115 (dm$^{3/2}$.mol$^{-1/2}$), A= -0.0651 (dm$^{3/2}$mol$^{-1/2}$), A=-0.2443 (dm$^{3/2}$.mol$^{-1/2}$).
B= 1.0908 (L.mol^{-1}), B= 1.6762 (L.mol^{-1}), B= 1.8116 (L.mol^{-1}), B= 2.3524 (L.mol^{-1}).
Linearity=0.9899, 0.9886, 0.9919, 0.9938.
C=molar concentration (mol/L)
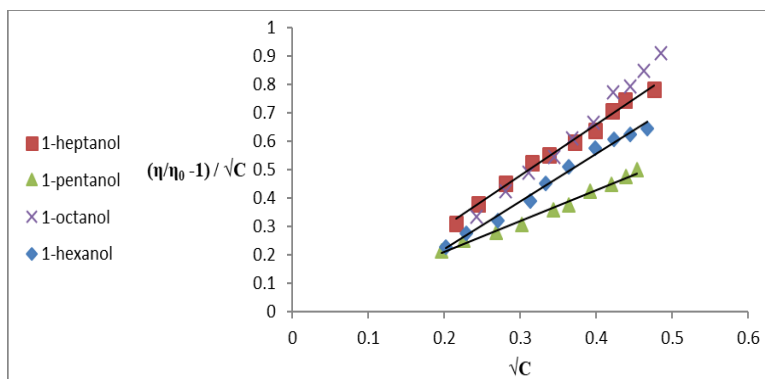
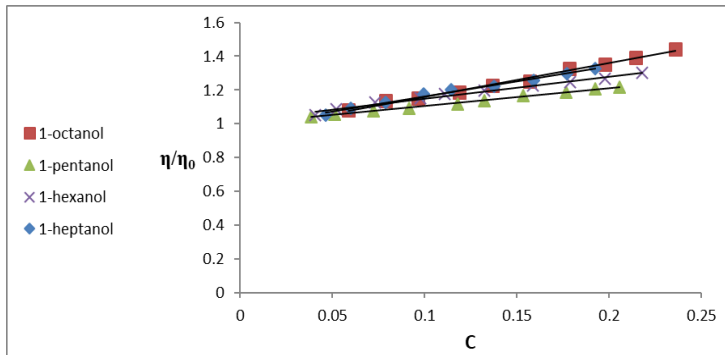**Figure 1.** Jone-Dole plot $\sqrt{C}$ versus $(\eta/\eta_o -1)/\sqrt{C}$ for alcohols at 298.

Table 2. Change of η/η_o with concentration of 1-pentanol, 1-hexanol, 1-heptanol and 1-octanol under 298.15 K

1-Pentanol			1-Hexanol			1-Heptanol			1-Octanol		
S. no.	Concen-tration (mol/L)	η/η_o	S. no.	Concen-tration (mol/L)	η/η_o	S. no.	Concen-tration (mol/L)	η/η_o	S. no.	Concen-tration (mol/L)	η/η_o
1	0.03859	1.04225	1	0.04066	1.04996	1	0.04669	1.06698	1	0.05867	1.08113
2	0.05114	1.05678	2	0.05227	1.08432	2	0.05992	1.09258	2	0.07884	1.11948
3	0.07223	1.07473	3	0.07334	1.12851	3	0.07887	1.12721	3	0.09664	1.15282
4	0.09143	1.09332	4	0.09786	1.15334	4	0.09954	1.16582	4	0.11888	1.18834
5	0.11778	1.12282	5	0.11098	1.17565	5	0.11448	1.18719	5	0.13653	1.22459
6	0.13224	1.13682	6	0.13241	1.18611	6	0.13776	1.22121	6	0.15678	1.26305
7	0.15326	1.16558	7	0.15864	1.22558	7	0.15892	1.25487	7	0.17845	1.32667
8	0.17668	1.18893	8	0.17885	1.24772	8	0.17694	1.29782	8	0.19773	1.35348
9	0.19242	1.20846	9	0.19778	1.26537	9	0.19224	1.32664	9	0.21448	1.39287
10	0.20557	1.22623	10	0.21789	1.30112	10	0.22672	1.37248	10	0.23567	1.44139

Accordingly, η is the viscosity of solution and η_o is the viscosity of water.

Evaluation of B coefficients for each alcohol was positive in aqueous solutions thereby signifying the existence of a strong ion-solvent interactions in the solution. These organic materials are like structure-makers in water. The A value gotten from all alcohols was negative and estimated for non-electrolytes as solute that stands for the ion-ion interaction measurement [26-

28]. A depiction of (η/η_o) verses concentration must be linear taking slope magnitude equivalent to B coefficient for non-electrolytes and the equation 2 applicability. The data from the experiments was employed for examining how the experimental consequences of viscosity agree with Eq.2 for non-electrolyte molecules. The magnitudes were shown in Table 2 and in Fig. 2.

Figure 2. Plot (C) versus (η/η_o) for alcohols at 298.15 K

$$\eta/\eta_\circ = BC + 1 \ \dots\dots \ (2)$$

Table 3. Ax and Bx amounts for aqueous 1-pentanol, 1-hexanol, 1-heptanol and 1-octanol under 298.15 K based on modified Jone-Dole equation

1-Pentanol		1-Hexaoll		1-Heptanol		1-Octanol	
S. no.	$(\sqrt{X_s/X_w})$	$\dfrac{(\eta/\eta_\circ-1)/}{\sqrt{X_s/X_w}}$	S. no.	$(\sqrt{X_s/X_w})$	$\dfrac{(\eta/\eta_\circ-1)/}{\sqrt{X_s/X_w}}$	S. no.	$(\sqrt{X_s/X_w})$	$\dfrac{(\eta/\eta_\circ-1)/}{\sqrt{X_s/X_w}}$	S. no.	$(\sqrt{X_s/X_w})$	$\dfrac{(\eta/\eta_\circ-1)/}{\sqrt{X_s/X_w}}$
1	0.04788	0.88238	1	0.05248	0.95198	1	0.05884	1.13834	1	0.06158	1.31747
2	0.06102	0.93038	2	0.08616	0.97865	2	0.07969	1.16175	2	0.08929	1.33812
3	0.07631	0.97927	3	0.12149	1.05778	3	0.10658	1.19376	3	0.11169	1.36825
4	0.09097	1.02579	4	0.13982	1.09669	4	0.13437	1.23406	4	0.13359	1.40979
5	0.11607	1.05811	5	0.15772	1.11367	5	0.14899	1.25635	5	0.15576	1.44187
6	0.12399	1.10348	6	0.16362	1.13742	6	0.17061	1.29668	6	0.18021	1.45976
7	0.14508	1.14132	7	0.19159	1.17737	7	0.19344	1.31756	7	0.21636	1.50985
8	0.15993	1.18133	8	0.20479	1.20963	8	0.22082	1.34867	8	0.22856	1.54652
9	0.16951	1.22978	9	0.21421	1.23887	9	0.23343	1.39933	9	0.24763	1.58657
10	0.18081	1.25119	10	0.23773	1.26665	10	0.26264	1.41822	10	0.27509	1.60448

As clarified in Table 3, the magnitudes for concentration were used for calculating xs and xw in addition to the obtained date. The linear plot $(\sqrt{X_s/X_w})$ vs. $(\eta/\eta_\circ-1)/\sqrt{X_s/X_w}$ ratifies a veracity modified Jone-Dole Eq. as specified below.

Notes: Ax= 0.7664, Ax= 0.8417, Ax= 1.0479, Ax= 1.2174, Bx= 2.6623, Bx= 1.7915, Bx=1.4203, Bx= 1.4169. Linearity= 0.9911, Linearity= 0.9905, Linearity= 0.911, Linearity=0.9891

$$\frac{(\eta/\eta_\circ)-1}{\sqrt{X_s/X_w}} = Ax + Bx\sqrt{X_s/X_w} \quad \text{........ (3)}$$

Where Ax and Bx stand for the coefficients. They represent the interactions measured among solute-solute and solute-solvent. A corresponding plot has been illustrated in Fig. 3. The positive magnitudes of Ax and Bx gotten in the paper indicate the existence of ion-solvent interaction and solute-solute interaction [29,30]. The concentration extent applied in the project was optimal for a veracity of Staudinger, Jone-Dole equation in addition to the modified Jone- Dole equation that behaves like a "structure maker" [31].
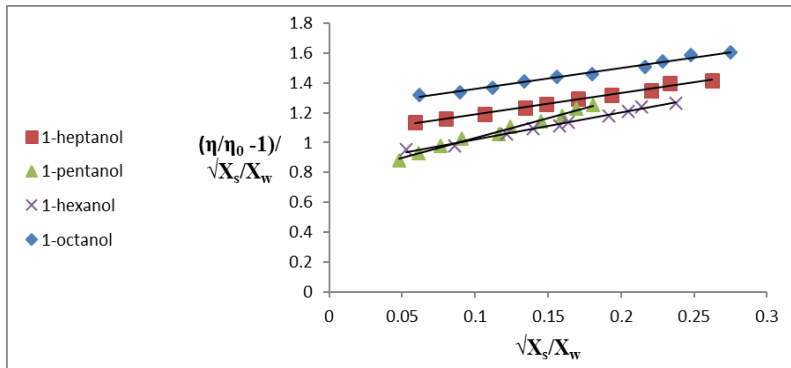
Figure 3. Modified Jone-Dole plot $\sqrt{X_s/X_w}$ versus $(\eta/\eta_\circ-1)/\sqrt{X_s/X_w}$ for alcohols at 298.15 K.

The apparent molar volumes (ϕv) of alcohols was determined based on the measured densities in dilute aqueous solution by [32-34].

$$\phi_v = \frac{M_s}{\rho_\circ} + \frac{1000(\rho_\circ-\rho)}{C} \quad \text{........ (4)}$$

Where Ms represents the molecular weight of alcohol, C is an alcohol concentration in mol/L and $\rho_\circ$ stands for a density of a pure solvent. The computed amounts of apparent molar volume for 1-pentanol, 1-hexanol, 1-heptanol, and

1-octanol are given in Table 5 and ploted in Fig.4. The magnitudes for apparent molar volumes (standard partial molar volume) (Vϕ˚) have been determined through least-squares fit to Masson's equation at infinite dilutions [35-37].

**Table 4.** A change of densities with concentration of 1-pentanol, 1-hexanol, 1-heptanol and 1- octanol under 298.15 K

	1-Pentanol			1-Hexanol			1-Heptanol			1-Octanol	
S. no.	Concen-tration (mol/L)	Density (gm/cm^3)	S. no.	Concen-tration (mol/L)	Density (gm/cm^3)	S. no.	Concen-tration (mol/L)	Density (gm/cm^3)	S. no.	Concen-tration (mol/L)	Density (gm/cm^3)
1	0.0000	0.997046	1	0.0000	0.997046	1	0.0000	0.997046	1	0.0000	0.997046
2	0.03859	0.99908	2	0.04060	0.99966	2	0.04669	1.00043	2	0.05867	1.00206
3	0.05114	0.99969	3	0.05227	1.00031	3	0.05992	1.00263	3	0.07884	1.00356
4	0.07223	1.00067	4	0.07334	1.00154	4	0.07887	1.0040	4	0.09664	1.00487
5	0.09143	1.00153	5	0.09786	1.00292	5	0.09954	1.00489	5	0.11888	1.00652
6	0.11778	1.00272	6	0.11098	1.00366	6	0.11448	1.00632	6	0.13653	1.00786
7	0.13224	1.00331	7	0.13241	1.00474	7	0.13778	1.00641	7	0.15678	1.00919
8	0.15326	1.00421	8	0.15864	1.00605	8	0.15892	1.00764	8	0.17845	1.01069
9	0.17668	1.00506	9	0.17885	1.00708	9	0.17694	1.00862	9	0.19773	1.01203
10	0.19242	1.00562	10	0.19778	1.00801	10	0.19224	1.00946	10	0.21448	1.0294
11	0.20556	1.00601	11	0.21789	1.00891	11	0.22672	1.01142	11	0.23567	1.01425

Table 5. Amounts ϕv of the Masson equation for aqueous 1-pentanol, 1-hexanol, 1-heptanol and 1-octanol under 298.15 K

	1-Pentanol			1-Hexanol			1-Heptanol			1-Octanol	
S. no.	$\sqrt{C}$	ϕ_v (cm^{3}mol^{-1})	S. no.	$\sqrt{C}$	ϕ_v (cm^{3}mol^{-1})	S. no.	$\sqrt{C}$	ϕ_v (cm^{3}mol^{-1})	S. no.	$\sqrt{C}$	ϕ_v (cm^{3}mol^{-1})
1	0.19644	35.31842	1	0.20164	37.69516	1	0.21608	43.73795	1	0.24222	46.50937
2	0.22614	36.30691	2	0.22863	39.51978	2	0.24479	44.77769	2	0.28078	47.19421
3	0.26876	37.52471	3	0.27081	40.64163	3	0.28084	45.74988	3	0.31084	48.77553
4	0.30237	38.90222	4	0.31283	41.86316	4	0.31549	46.52436	4	0.34479	49.97424
5	0.34319	39.72469	5	0.33314	42.23455	5	0.33835	47.92414	5	0.36828	50.39317
6	0.36364	40.50717	6	0.36388	43.67544	6	0.37116	48.39512	6	0.39595	52.06325
7	0.39148	41.09442	7	0.39829	44.96438	7	0.39865	49.64078	7	0.42243	52.97686
8	0.42033	42.44203	8	0.42291	45.57028	8	0.42064	50.83599	8	0.44467	53.58082
9	0.43866	43.21622	9	0.44472	46.19244	9	0.43845	51.62481	9	0.46312	55.14723
10	0.45339	44.14778	10	0.46679	47.13124	10	0.47615	52.69066	10	0.48546	56.21232

Notes: ϕv˚ = 28.801, ϕv = 31.326, ϕv˚ = 36.017, ϕv˚ = 36.224, Sv = 32.655, Sv = 33.75, Sv=34.775, Sv = 40.066. C= molar concentration (mol/L)
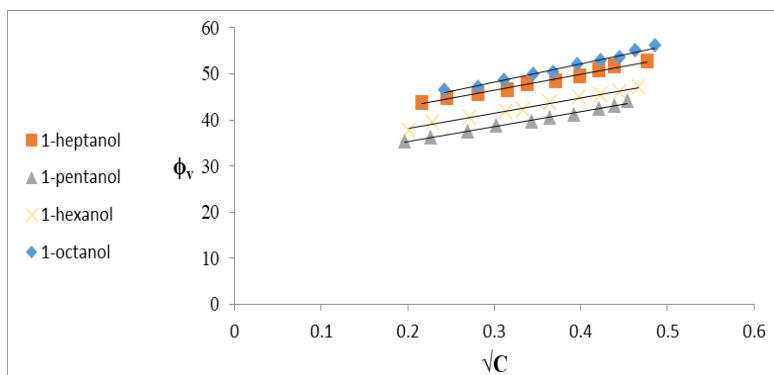
Figure 4. Masson plot apparent molal volumes (ϕ_v) versus ($\sqrt{C}$)
for alcohols at 298.15 K

$$\phi_v = \phi_v{}^\circ + S_v\sqrt{C} \ldots\ldots (5)$$

Where Sv is the experimental slope indicating solute-solute interaction and the (Vϕ°) values are separated solute-solute interaction at infinite dilution and only inverted the presence of solute-solute interaction among solute as well as solvent molecules. The ϕv magnitude is positive specifying the positive interaction among solute and solvent molecules [38, 39]. The Sv is positive signifying which ions possess the worthy complex ion-forming and resilient ion-ion interacting level in aqueous solution [40, 41].

CONCLUSIONS

In this analysis, density and viscosity parameters were used to investigate the existence of interactions in alcohol-water. The good value of the B-coefficient suggests that ion-solvent interaction is present in any system and it was concluded that there is a relationship between alcohols and water molecules because of hydrogen bonding. Accordingly, it stands for the structure maker in the aqueous solution. It can be said that the proposed modified Jon-Dole equation in this study can be a model for gaining more information in the field of molecular interaction studies.

EXPERIMENTAL

Alcohols (1-pentanol, 1-hexanol, 1-heptanol, and 1-octanol) were provided by Aldrich company with 98% purity. The viscosity measurements as a suspended level ubbelohde viscometer in a bath adjusted to ± 0.01 k at

298.15 k to determine the viscosities. Headed for giving the ending magnitudes, the experiments were repeated, at least three times, before the results were fixed.

ACKNOWLEDGMENTS

REFERENCES

[1] C. M. Romero; M. A. Esteso; *Chem. Chem. Eng. Sustain. Dev.*, **2020**, pp. 83–106.

[2] M. M. Hoffmann; R. H. Horowitz; T. Gutmann; G. Buntkowsky; *J. Chem. Eng. Data*, **2021**, *66(6)*, 2480–2500.

[3] U. Shahazidy; M. Asghar Jamal; M. Muneer; B. Naseem; A. Kaleem Qureshi; *J. Mol. Liq.*, **2022,** *350*, 54–57.

[4] Y. Cao*;* Y. Peng; D. Cheng; L. Chen; M. Wang; C. Shang; L. Zheng; D. Ma; Z. P. Liu; *ACS Catal.*, **2023**, *13(1)*,735–743.

[5] S. A. Yaseen; A. S. Alameen; F. A. Saif; S. B. Undre; P. B. Undre; *J. Mol. Liq.*, **2021**, *340*, 5–9.

[6] V. Sharma; C. Bhatia; M. Singh; C. Singh; S. K. Upadhyaya; K. Kishore; *J. Mol. Liq.*, **2020**, *308*, 5–9.

[7] S. Rasouli; M. R. Moghbeli; S. M. Hashemianzadeh; *Mater. Res. Express*, **2022**, *9(9)*,17–20.

[8] B. Lee; J. Kim; K. Shin; K. H. Park; M. Cha; S. Alavi; *Cryst. Eng. Comm.*, **2021**, *23(26)*, 4708–4716.

[9] P. Patanjali; I. Chopra; A. Mandal; R. Singh; *Indian J. Chem. Technol.*, **2021**, 28(1), 86–93.

[10] D. M. Li; J. Huang; Z. H. Ren; Y. J. Lu; Y. J. He; S. W. Liu; *J. Dispers. Sci. Technol.*, **2020,** *41(6)*, 856–862.

[11] C. M. Romero; Y. P. Cruz; and S. Perez-Casas; *Thermochim. Acta*, **2020**, *684*, 36–39.

[12] Y. N. Malakhova; A. A. Stupnikov; V. P. Chekusova; N. M. Kuznetsov; S. I. Belousov; *Bio nano science*, **2020**, *10(2)*, 403–408.

[13] S. Baluja; *J. Anal. Pharm. Res.*, **2021**,*10(5)*, 169–175.

[14] M. Ikeda; M. Aniya; *Key Eng. Mater.*, **2020**, *861* KEM, 264–269.

[15] C. E. Miller; P. C. Lozano; *Appl. Phys. Lett.*, **2020,** *116(25)*, 7–10.

[16] B. D. Prince; C. J. Annesley; R. J. Bemish; S. Hunt; *AIAA Propuls. Energy Forum Expo., 2019*, pp. 1–4.

[17] B. B. Nanda; M. Pradhan; P. Kar; B. Nanda; *Biointerface Res. Appl. Chem.*, **2020**, 10(4), 5901–5909.

[18] J. Article; *Biointerface Res. Appl. Chem.*, **2021**, 12(1), 339–350.

[19] L. Hnedkovsky; L. Rasanen; P. Koukkari; G. Hefter; *J. Chem. Eng. Data*, **2021**, 66(1), 38–44.

[20] A. Thakur; K. C. Juglan; H. Kumar; *J. Phys. Conf. Ser.*, **2020**, 1531(1), 1–11.

[21] M. Khandelwal; *Int. J. Eng. Res.*, **2020**, 9(06), 7–9.

[22] M. Almasi; *J. Chem. Eng. Data*, **2020**, 65(90, 4498–4502.

[23] S. Agarwal; D. K. Sharma; *Open J. Phys. Chem.*, **2021**,11(03), 168–181.

[24] A. F. Abdulzahra;, M. H. Saleem; I. M. Radhi; Z. A. Al-Dulaimy; *Int. J. Pharm. Res.*, **2020**, 12(2), 1229–1232.

[25] F. Koohyar; H. Ghasemnejad-Bosra; M. Sharifirad; *Studia UBB Chemia*, **2012**, *57(4)*, 217–231.

[26] O. Miyawaki; Y. Norimatsu; H. Kumaga; Y. Irimoto; H. Kumagai; H. Sakurai; *Biopolymers*, **2003**, 70(4), 482–491.

[27] S. K. Sharma; A. Thakur; *J. Mol. Liq.*, **2021**, *322*, 114527.

[28] B. S. Journal; *Baghdad Sci. J.*, **2011**, *8(2)*, 348–358.

[29] Z. A. H. Al-Dulaimy; D. T. A. Al-Heetimi; H. S. Khalaf; A. M. Abbas; *Orient. J. Chem.*, **2018**, 34(4), 2074–2082.

[30] H. S. Khalaf; Z. A. H. Al-Dulaimy; A. M. Abbas; M. H. Saleem; **2019**, *Asian J. Chem.*, 31(4), 820–824.

[31] S. K. Lai; C. C. Lim; *J. Comput. Chem.*, **2021**, 42(5), 310–325.

[32] H. Kumar; R. Sharma; *J. Chem. Thermodyn.*, **2021**, *152*, 28–31.

[33] B. S. Journal; *Baghdad Sci. J.*, **2006**, 3(1), 147–155.

[34] T. A. Salman; K. A. Abd; *Baghdad Sci. J.*, **2013**, *10(2)*, 432–441.

[35] P. G. Raundal; A. A. Sheikh; S. S. Kasim; *J. Adv. Sci. Res.*, **2021**, *12(01)*, 99–105.

[36] M. Shakeel; K. Mahmood; *J. Chinese Chem. Soc.*, **2020**, *67(9)*,1552–1562.

[37] T. Mallik; S. Ghosh; D. Ekka; *J. Serbian Chem. Soc.*, **2022**, *87(10),*1171–1184.

[38] D. T. A. Al-Heetimi; Z. A. Al-Dulaimy; A. A. Al-Jawary; O. S. Al-Khazrajy; *Studia UBB Chemia*, **2019**, *64(1)*, 103–112.

[39] M. M. Budeanu; V. Dumitrescu; *Appl. Sci.*, **2022**, *12(1)*, 5–8.

[40] A. Thakur; K. C. Juglan; H. Kuma; K. Kaur; *Phys. Chem. Liq.*, **2020**, 58(6), 803–819.

[41] H. G. Attiya; Z. A. H. Al-Dulaimy; K. A. Sadiq; M. H. Saleem; *Orient. J. Chem.*, **2019**, *35(1)*, 337–342.

KETOCONAZOLE-PAMAM DENDRIMER SUPRAMOLECULAR COMPLEX FOR PROLONGED DELIVERY BY IN VITRO AND IN VIVO STUDIES

Irina KACSO[a], Ioana BÂLDEA[b], Maria MICLĂUŞ[a], Augustin MOŢ[a,c], Remus MOLDOVAN[b], Flavia MARTIN[a,*]

ABSTRACT. The current study investigates the potential of the supramolecular complex between the antifungal agent Ketoconazole (KTZ) and PAMAM dendrimer G5 generation to be used as a topically applied antimycotic drug. The new drug-dendrimer formulation was confirmed by combining XRPD, FT-IR and DSC analytical techniques, and presents improved aqueous solubility and delayed in vitro release profile compare to pure KTZ. The biological assays data showed the biocompatibility of the supramolecular complex and improved delivery of the encapsulated KTZ into the superficial layers of skin and mucosa at the mycotic infections site, leading to a better outcome of the infection.

Keywords: Ketoconazole, PAMAM dendrimer, Drug-dendrimer complex, Solubility, Cell viability, Mouse ear sensitization test

INTRODUCTION

Invasive fungal infections are a major cause of morbidity and mortality in premature infants, immuno-compromised patients or in those with acquired immune deficiency syndrome [1, 2].

[a] *National Institute for R&D of Isotopic and Molecular Technologies, 67-103 Donat str., RO-400293 Cluj-Napoca, Romania*

[b] *Department of Physiology, Iuliu Haţieganu University of Medicine and Pharmacy, 1 Clinicilor str., RO-400006 Cluj-Napoca, Romania*

[c] *Department of Chemistry, Faculty of Chemistry and Chemical Engineering, 11 Arany Janos str., RO-400028 Cluj-Napoca, Romania*

[*] *Corresponding author: flavia.martin@itim-cj.ro*

IRINA KACSO, IOANA BÂLDEA, MARIA MICLĂUȘ, AUGUSTIN MOȚ,
REMUS MOLDOVAN, FLAVIA MARTIN

Azole antifungal agents represent the most important class of drugs used in clinical treatment of fungal infections. **Ketoconazole** (**KTZ**, $C_{26}H_{28}Cl_2N_4O_4$, *cis*-1-acetyl-4-[4-[2-(2,4-dichlorophenyl)-2-(1H-imidazol-1-ylmethyl)-1,3-dioxolan-4-yl]methoxy]phenyl]piperazine, **Figure 1**) was the first broad-spectrum oral antifungal Active Pharmaceutical Ingredient (API) approved by U.S. Food and Drug Administration (FDA) in 1981.
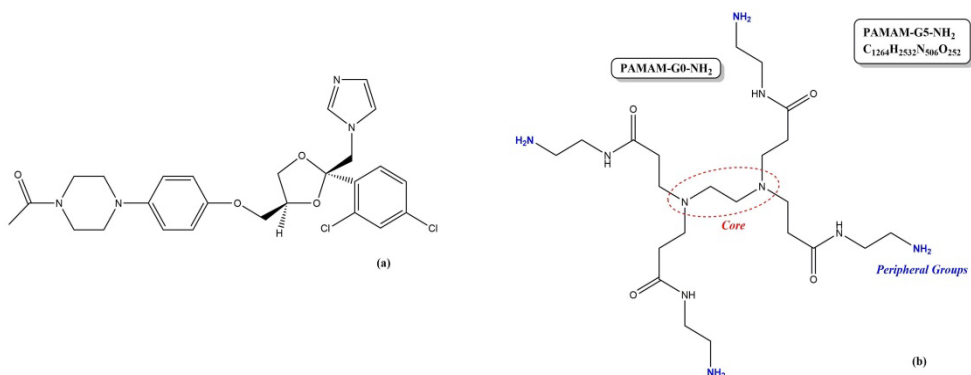
Figure 1. Chemical structure of **Ketoconazole (KTZ)** (a) and polyamidoamine dendrimer of G5 generation **(PAMAM-G5-NH₂)** (b)

According to Biopharmaceutics Classification System, **KTZ** is a class II drug, with low solubility and high permeability [3]. It's very low aqueous solubility, 0.017 mg/mL [4], limits its bioavailability, because the drug is eliminated from the gastrointestinal tract before it is completely dissolved, reducing its absorption into the blood circulation. Despite post-marketing reports of drug-related hepatotoxicity, it's been used, off-label, as a second-line therapy for castration-resistant prostate cancer [5], and in 2014 the European Medicines Agency approved *Ketoconazole HRA* for oral use as a second-line drug in Cushing's disease [6]. Because poor systemic absorption was observed from topical formulations, **KTZ** is often used for dermatological conditions [7].

In order to enhance the solubility and bioavailability of **KTZ,** different solid forms, salts or cocrystals, obtained by *crystal engineering* approach and using different co-formers, *e.g.*, dicarboxylic acids [8, 9], *p*-amino-benzoic acid [10], some phenolic acids [11], have been reported. Another way for its solubility enhancement is based on *formulations*, as solid dispersions [12], hot-melt extrusion [13] or inclusion complexes with beta-cyclodextrins [14].

The ability of *dendrimers* to encapsulate and form complexes with drugs and biologically active products rely on their unique properties, such as hyperbranching, well-defined spherical structure, and high compatibility with the

biological systems [15-17]. One of the most-studied starburst macromolecules is represented by *PAMAM (polyamidoamine) dendrimers*, their specific properties and low toxicity make them suitable as drug delivery systems and with the ability of controlled drug release [18, 19]. **KTZ** pharmaceutical formulations based on PAMAM dendrimers were also reported. Two studies have evaluated the **KTZ** solubility in the presence of PAMAM-NH_2 dendrimers of G1-G3 low generations, in hydrogel [20] and in solution forms [21].

The aim of this study is to evaluate the potential of the PAMAM dendrimer of higher generation, G5, with amine peripheral groups to encapsulate and to act as a carrier for the antifungal agent **KTZ** for topical therapy of cutaneous mycosis. The encapsulation is performed by the lyophilization method, a simple and reproductible one, often used for preparing this type of formulations. The physico-chemical and performance attributes of the new **KTZ-PAMAM-G5-NH_2** supramolecular complex were investigated by various thermo-analytical and spectroscopic techniques. The biocompatibility was assessed on normal dermal fibroblasts and hepatic cell line HepG2 and the risk for allergy induction following cutaneous exposure with the KTZ-dendrimer formulation was tested by the mouse ear swelling test.

RESULTS AND DISCUSSION

Generally, high generation PAMAM dendrimers possesses high-density amino groups on the surface with positive charge, while low generation PAMAMs contain a reduced and incompact peripheral structure. The interaction between the selected dendrimer, **PAMAM-G5-NH_2**, and the active substance **KTZ** is of host-guest type (e.g., electrostatic interactions, hydrogen bonds) and consist in simple encapsulation of the API in dendrimer cavities [22]. The physical entrapment approach of guest molecules into dendrimer cavity is usually performed in a single stage, as compared to the chemical conjugation method, which requires multiple stages [23, 24].

1. Identification of the supramolecular complex

Powder X-ray Diffraction

The powder X-ray diffraction (PXRD) patterns of the pure **KTZ** [8] and the lyophilized **KTZ-PAMAM-G5-NH_2** supramolecular complex are shown in **Figure 2**.
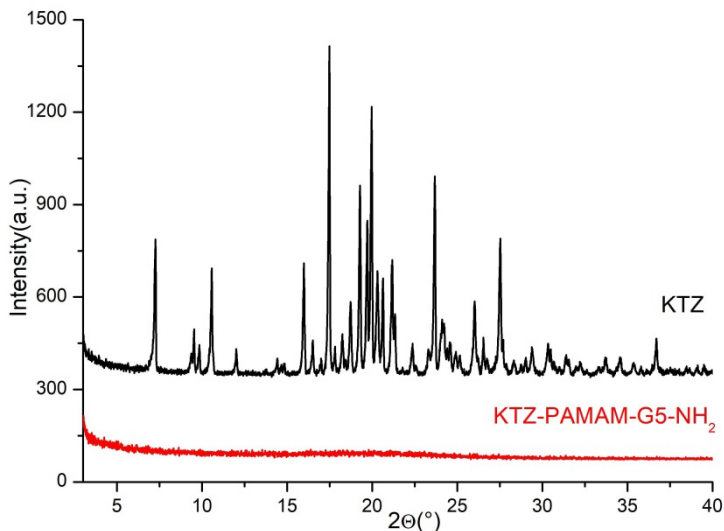
Figure 2. Experimental PXRD patterns of the **KTZ** and **KTZ-PAMAM-G5-NH$_2$**
supramolecular complex

The powder diffraction pattern of the supramolecular complex displays an amorphous structure, characterized by long-range ordering. Thus, the disappearance of all the characteristic diffraction lines of **KTZ** is observed, proving its encapsulation in the cavity of **PAMAM-G5-NH$_2$** dendrimer.

FT-IR spectroscopy analysis

FT-IR was used to study the interaction between **KTZ** and **PAMAM-G5-NH$_2$** dendrimer, and the structural changes in the complex compared to free dendrimer. FT-IR spectra of the pure **KTZ**, **PAMAM-G5-NH$_2$** dendrimer and **KTZ**-**PAMAM-G5-NH$_2$** supramolecular complex are exposed in **Figure 3**.

In the FT-IR absorption spectra of the supramolecular complex the characteristic bands of the two components, **KTZ** [25, 26] and **PAMAM-G5-NH$_2$** dendrimer [27] can be identified with their slight modifications, consisting in the broadening of the bands and the displacement of the maxima of some bands or even the absence of others, due to compounds interactions and amorphous character of the supramolecular complex. Compared to the FT-IR spectrum of pure **KTZ**, one can observe: the characteristic bands of the stretching vibrations of the -NH groups at 3118 cm^{-1} and 2883 cm^{-1} are not found on the supramolecular complex spectrum, the weak intensity stretching vibration of the C=O carbonyl group from 1726 cm^{-1} shifts and appears as a weak shoulder of the amide band of dendrimer at 1743 cm^{-1}, the vibrational band

140
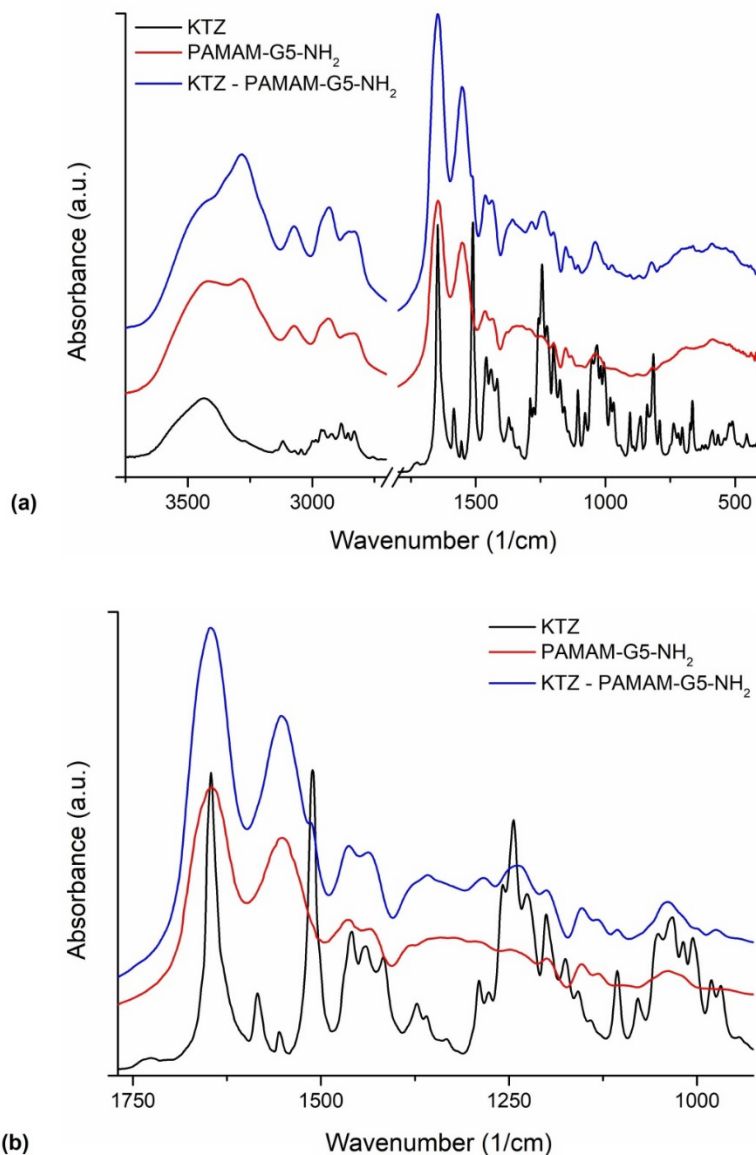
Figure 3. FT-IR spectra of **KTZ**, **PAMAM-G5-NH₂** and **KTZ-PAMAM-G5-NH₂**
in the 3750–500 cm^{-1} (a) and 1770-925 cm^{-1} (b) spectral domain

of KTZ from 1510 cm^{-1} shifts and appears as a shoulder at 1514 cm^{-1} and the bands from 1373 cm^{-1} and 1360 cm^{-1} are shifted and appear as a broad band with a shoulder at 1378 cm^{-1} and the maximum at 1358 cm^{-1}; the vibrational

bands located at 1258, 1244 and 1223 cm^{-1} appear as a broad band with ~~a~~ maximum at 1237 cm^{-1}. The vibrational bands of the C-Cl bond appear as broad bands or shoulders, being shifted from 1006, 826, and 822 cm^{-1} to 1000, 737, and 733 cm^{-1}, respectively. Regarding the occurred changes in the spectrum of the dendrimer after complexation, one can observed the shift of the vibration bands from 1644, 1435 and 1250 cm^{-1} at 1647, 1437 and 1238 cm^{-1}, respectively. The resulting changes are due to weak interactions (electrostatic interactions, hydrogen bonds), which are formed between the two components.

Differential Scanning Calorimetry thermal analysis

The thermal behavior of the supramolecular complex is illustrated by the DSC curve in the temperature range 20-250 °C (**Figure 4**). Several endothermic signals appear, among which can be identified: the broad peak of dendrimer **PAMAM-G5-NH₂** from 118.9 °C moved to 114.8 °C; a sharp endothermic signal with a maximum at 117 °C; the melting signal of **KTZ** at 149.5 °C appears as a broad low-intensity peak with a maximum at 146.9 °C.
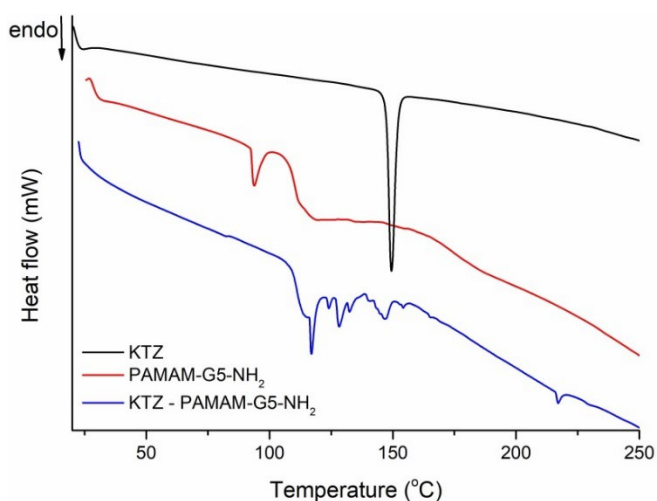
**Figure 4.** DSC traces of **KTZ**, **PAMAM-G5-NH₂** and **KTZ-PAMAM-G5-NH₂**

The differences identified on DSC curve of the supramolecular complex compared to DSC curves of the starting substances **KTZ** and **PAMAM-G5-NH₂** denote the presence of weak interactions between them with the formation of a material with a high degree of amorphous content, as determined already by XRPD, and different thermal events compared to the starting components.

2. Aqueous solubility of supramolecular complex

The evolution of the dissolution process over time in aqueous systems is an indicative of how a solid form is absorbed into the body. The aqueous solubility of the **KTZ-PAMAM-G5-NH$_2$** supramolecular complex was investigated using the optical nephelometric method [28]. This analytical technique involves measuring the degree of relative turbidity, due to the diffusion or scattering of monochromatic light, as Tyndall effect, caused by the insoluble particles dispersed in the solution. **Figure 5** and **6** show the scattered light spectra in the 500 – 700 nm spectral domain, for both **KTZ** and **KTZ-PAMAM-G5-NH$_2$** complex solutions, at different concentrations.
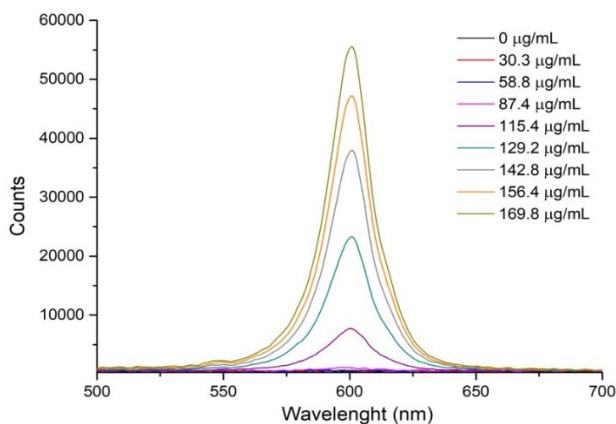
Figure 5. Spectra of scattered light for **KTZ** solutions at increasing concentrations
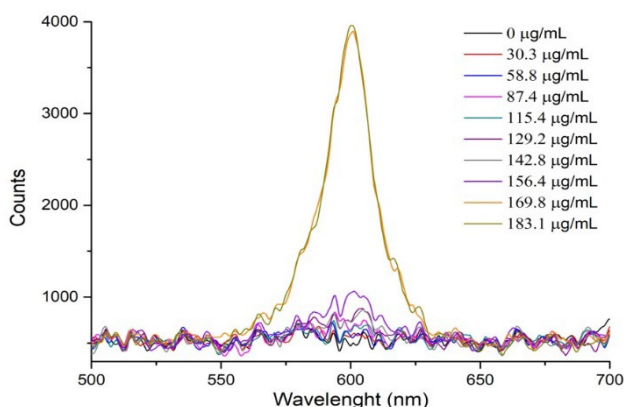
Figure 6. Spectra of scattered light for **KTZ-PAMAM-G5-NH$_2$** solutions
at increasing concentrations

143

The aqueous solubility of pure **KTZ** and the **KTZ**-dendrimer formulation can be evaluated from the diffuse light intensity profile as a function of the concentration of the tested compound, as illustrated in **Figure 7**.
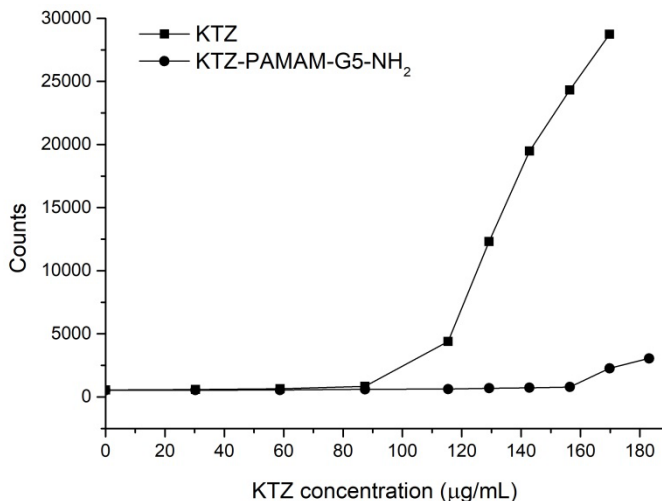
Figure 7. Evaluation of the limit solubility of **KTZ** and **KTZ-PAMAM-G5-NH₂** tested samples, from the variation of the diffuse radiation intensity at λ=590 nm depending on the concentration, in double-distilled water

In the case of the pure active substance **KTZ**, the solubility limit is detected by a sudden increase in the amount of suspended particles in double-distilled water at a concentration of 87.4 µg/mL.

On the other hand, the solubility limit for the supramolecular complex is detected at 156.5 µg/mL, but the precipitation process is very slow compared to that detected for **KTZ**. Thus, the encapsulated molecules of **KTZ** in the dendrimer cavity, through non-covalent bonds, are slowly released, so the solid particles will accumulate and finally precipitate in the aqueous solution.

3. In-vitro release profile of KTZ from the dendrimer supramolecular complex by the dialysis method

The stability of supramolecular complex and the encapsulation propensity of the **PAMAM-G5-NH₂** dendrimer were investigated by *the dialysis method* against double-distilled water [29, 30]. The *in vitro* release profile of pure **KTZ** and the **KTZ** encapsulated in the PAMAM dendrimer cavity was monitored by UV-Vis spectrophotometry (**Figure 8**).
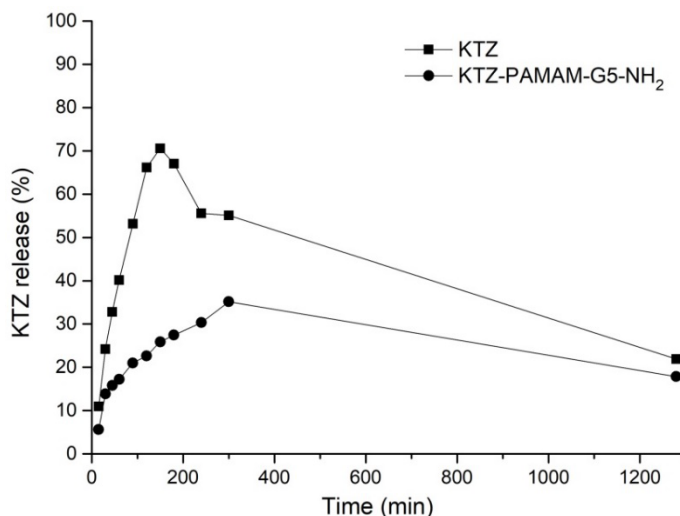
Figure 8. *In vitro* release of **KTZ** in **PAMAM-G5-NH$_2$** dendrimer aqueous solution compared with the pure **KTZ** release behavior

In the dialysis *in vitro* release experiment for pure **KTZ** during 150 minutes about 70% of the total amount of the active substance was released in the external aqueous phase, but, after 180 minutes, a decrease to 67% of the amount of KTZ was observed. This decrease in the amount of dissolved **KTZ** is due to the precipitation of the active substance in the external aqueous solution.

On the other hand, in the case of the **KTZ-PAMAM-G5-NH$_2$** complex, a slow release of the encapsulated drug was observed, thus after 90 minutes only ~20% of the amount of **KTZ** was released, and after 5 hours about 36%. Therefore, a continuous and considerably slower process of the **KTZ** released from the complex compared to pure **KTZ** occurred, without precipitation of the active substance in the external solution during the first 5 hours of the experiment. The *in vitro* release profile of **KTZ** from the dendrimer complex shows a controlled process vs. pure **KTZ,** probably due to its hydrophobic character, which allows it to remain longer embedded in the dendrimer cavities, suggesting that electrostatic interactions play an important role in drug release from dendritic complexes [21]. Our results are comparable to those reported for Ketoconazole- dendrimers PAMAM-G1-G3-NH$_2$ solution or hydrogel formulations [20, 21], but the *in vitro* release experiments were carried out in different conditions, as acidic pH or hydrogel components, which potentiates the solubility of KTZ.
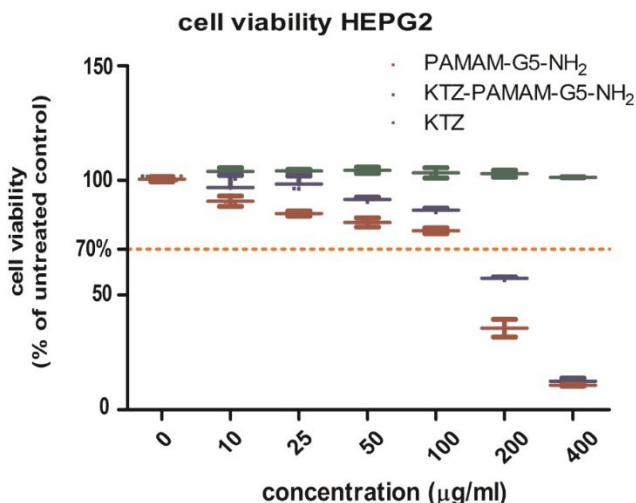
Cell viability

Fibroblasts. Cell viability was reduced in a concentration-dependent manner in all treated groups. The concentration of 100 µg /mL decreased the cell viability below the toxic level of 70% in the case of **KTZ** and very close in the case of **PAMAM-G5-NH₂** and **KTZ-PAMAM-G5-NH₂**, respectively. These data confirm the toxicity of the compounds at a concentration greater than or equal to 100 µg/mL. Cells exposed to concentrations below 100 µg/mL demonstrated good viability. There are also no significant differences in viability between **KTZ** and **KTZ-PAMAM-G5-NH₂** treated groups at these concentrations (**Figure 9**).
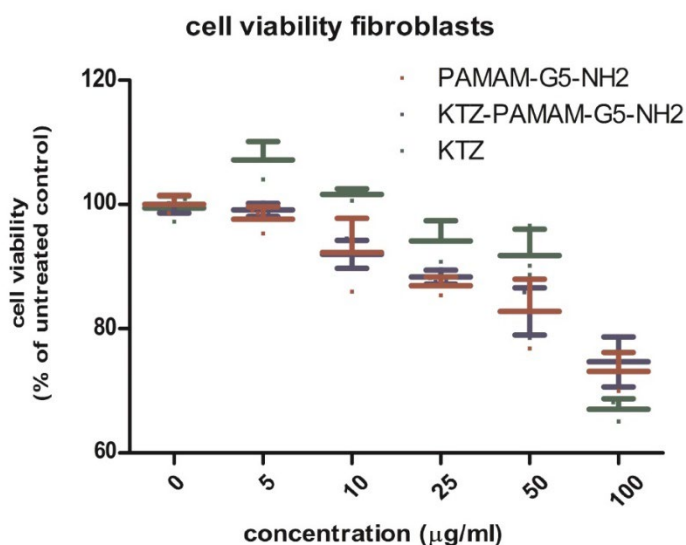
Figure 9. Cell viability of normal dermal fibroblasts (BJ) treated with **KTZ**,
PAMAM-G5-NH₂ dendrimer and **KTZ- PAMAM-G5-NH₂**,
data are expressed as % of untreated controls.

Hep-G2. Cell viability was decreased in the **PAMAM-G5-NH₂** and **KTZ-PAMAM-G5-NH₂** groups in a dose-dependent manner but was maintained above the toxicity limit (70%) at concentrations below 200 µg/mL. **KTZ** did not cause a significant decrease in viability at all tested concentrations. These data confirm good liver cell viability at the **KTZ-PAMAM-G5-NH₂** complex up to a concentration of 100 µg/mL. In liver cells, **KTZ-PAMAM-G5-NH₂** showed toxicity at higher doses, compared to **KTZ** (**Figure 10**).

Figure 10. Cell viability of hepatic carcinoma cells (Hep-G2) treated with **KTZ**,
PAMAM-G5-NH₂ dendrimer and **KTZ- PAMAM-G5-NH₂**,
data are expressed as % of untreated controls

4. Epicutaneous auricular sensitization test in mouse model

Mice were observed for any distress sign due to the cutaneous application of the substances. All mice survived and there was no weight loss, or hair loss during the exposure period. The mice in the dinitrochlorobenzene (DNCB) group showed swelling of the treated ear, as well as the tendency to scratch and at rechallenge, they showed signs of local pain-retraction of the head and vocalization, when the treated ear was touched, localized erythema, edema. All the other groups showed no macroscopic ear modifications at any of the measurement points (**Figure 11**).
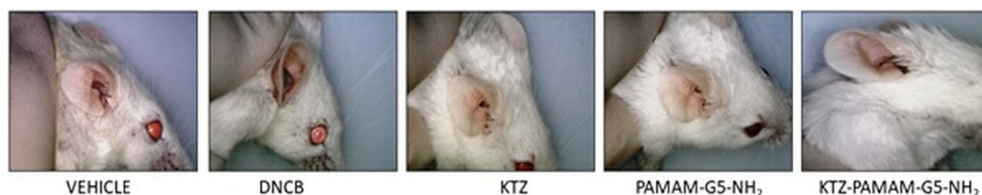
Figure 11. Comparative images of BALB c mice ears treated with vehicle - negative control, DNCB - positive control and the test compounds: **KTZ**, **PAMAM-G5-NH₂** and **KTZ-PAMAM-G5-NH₂**

147

The obtained data from the MEST show a statistically significant increase in ear thickness in the DNCB group, the positive control group, which confirms the validity of the test model. In the other groups, no significant differences were obtained compared to vehicle-control, at any of the time points when measurements were made (**Figure 12**). Therefore, data show the validity of the model with epicutaneous sensitization in the positive control-DNCB group and no sensitization following exposure to the **KTZ**, **PAMAM-G5-NH₂** and respectively **KTZ- PAMAM-G5-NH₂**.
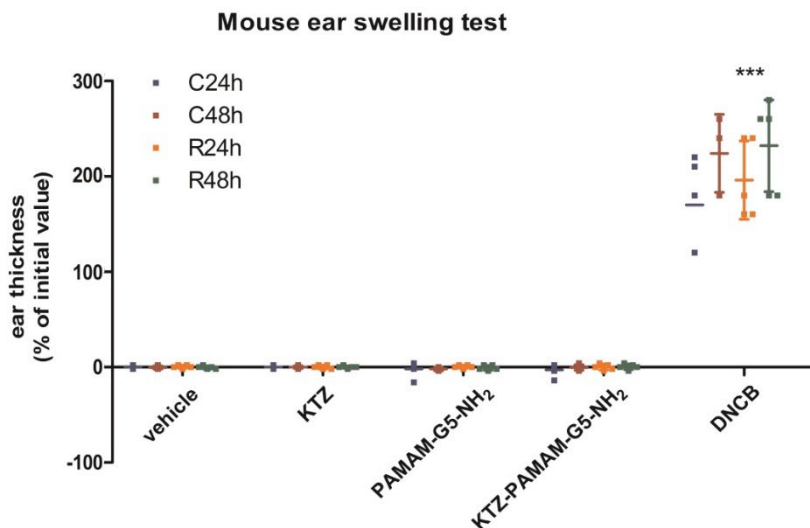
Figure 12. Epicutaneous mouse ear sensitization test using 5 experimental groups (n=5animals/group): control – vehicle, positive control - DNCB, and the test compounds: **KTZ**, **PAMAM-G5-NH₂**, and **KTZ-PAMAM-G5-NH₂** (***= p<0,0001)

Ear thickness measurements for each group after challenge at 24h (C24h), challenge at 48h (C48h) and respectively rechallenge at 24h (R24h) and 48h (R48h) are presented as % of initial ear thickness as media± standard deviation.

Cell viability tests proved that **KTZ-PAMAM-G5-NH₂** was well tolerated by the skin cells, dermal fibroblasts, in concentrations bellow 100 µg/mL and very well by the hepatic carcinoma cells, at concentrations up to 400 µg/mL.

CONCLUSIONS

Drug-dendrimer complexation is a widely used approach in pharmaceutical industries to increase stability, solubility, bioavailability and controlled release of drugs.

The current study evaluated the potential of the **PAMAM-G5-NH$_2$** dendrimer as drug carrier for the active antifungal **KTZ**. Being a BCS class II drug, its very low aqueous solubility represents a major disadvantage for its efficacy. Therefore, an increase of its solubility/bioavailability would lower the dose required for the therapeutic effect, and at the same time, provide hepatoprotection.

The new drug-dendrimer based formulation, obtained through non-covalent bonds, was confirmed by combining XRPD, FT-IR, DSC techniques. The supramolecular complex presents improved aqueous solubility over pure **KTZ**, and the *in vitro* release profile exhibited the delayed release of the encapsulated **KTZ,** being also achieved in a controlled manner compared to pure API. The biological assays data showed the biocompatibility of the tested compound and are encouraging for the potential application of the **KTZ-PAMAM-G5-NH$_2$** supramolecular complex in topical therapy of cutaneous mycosis. **KTZ-PAMAM-G5-NH$_2$** can improve the delivery of **KTZ** into the superficial layers of the skin and mucosa, at the mycotic infections site, due to their better stability, leading to a better outcome of the infection. However, more studies are needed to prove the bioavailability and the enhancement of the antimycotic properties, which will be addressed in future research.

EXPERIMENTAL SECTION

Materials

Ketoconazole, commercial form, was purchased from Melone Pharmaceutical Co. Ltd., China, and used without further purification. Amine-terminated fifth-generation PAMAM (polyamidoamine) dendrimer with ethylenediamine core (molecular weight = 28824.81 g/mol, 128 amine end groups) as 5% methanolic solution was purchased from Sigma-Aldrich Chemical Company, USA. Reagent grade solvents were purchased from Merk. Balc c mouse model were purchased from Cantacuzino Institute, Bucharest, Romania. All lab animal experiments were approved by ethics committee of the University of Medicine and Pharmacy Cluj-Napoca and the Veterinary Health Directorate, Romania (authorization number 329 / 17 08 2022).

Encapsulation of Ketoconazol in PAMAM-G5-NH₂ dendrimer

20 mg KTZ was dissolved in 1 mL methanol and magnetically stirred for 30 min at room temperature, following which 1.36 mL methanolic solution of **PAMAM-G5-NH₂** was added (**KTZ:PAMAM-G5-NH₂** = 10:1 molar ratio). The reaction mixture was stirred for 24h in the dark, then lyophilized for 24h to remove methanol. The **KTZ-PAMAM-G5-NH₂** supramolecular complex was obtained in the form of translucent sticky clay. The solvent removal was performed with an Alpha 1-2 LD type freeze dryer, at -55 °C and 0.010 atm.

Powder X-ray Diffraction

X-ray patterns were collected at room temperature using a Rigaku SmartLab multipurpose diffractometer, with Cu Kα1 radiation (λ = 1.54056 Å), equipped with a 9 kW rotating anode. For the acquisition of the experimental data, Smart- Lab Guidance software was used. The samples were ground to a fine homogeneous powder using an agate pestle and mortar and mounted on a sample holder. The measurements were performed in the 3°–40° 2θ range using steps of 0.01°.

FT-IR spectroscopy analysis

FT-IR spectra were obtained with a resolution of 4 cm^{-1} using a JASCO 6100 FT-IR spectrometer in the 4000–400 cm^{-1} spectral domain by employing the KBr pellet technique. Each sample has been dispersed in about 300 mg of anhydrous KBr, and the resulting powder was ground in an agate mortar. The pellet was obtained by pressing the ground mixture into an evacuated die. The spectra were collected and analysed with Jasco Spectra Manager v.2 software.

Differential Scanning Calorimetry analysis

Thermal measurements were performed with a DSC-60 Shimadzu differential scanning calorimeter and a SDT Q600 TA Instruments thermogravimeter. For the DSC measurements, standard aluminum crimped pan was used as sample holder and alumina as reference sample. An amount about 1.5–1.7 mg of each sample has been analysed in the 20–300 °C temperature range under dry nitrogen flow (3.5 L h^{-1}) with a 10 °C min^{-1} heating rate. Each measurement was performed in triplicate. For data collection and analysis, the Shimadzu TA-WS60 and TA60 2.1 software were employed. The DSC calorimeter was calibrated with reference standards of zinc and indium.

Aqueous solubility evaluation by Nephelometric method

The experimental device is equipped with a Silver Nova CCD simultaneous detector, and the experiments were performed using an LED with a wavelength of λ=590 nm, and the integration time was set to 500 ms. The solubility test was performed in double-distilled water at room temperature and the stock solutions of substances **KTZ**, **PAMAM-G5-NH$_2$** dendrimer and **KTZ-PAMAM-G5-NH$_2$** supramolecular complex were prepared in DMSO. For each analyzed sample, the diffuse radiation spectrum was measured, for a series of solutions at increasing concentrations in 30 – 185 μg/mL range. Analytical samples were prepared by adding increasing volumes (5 – 10 μL) of the stock solution, in a volume of 1 mL double-distilled water.

In-vitro release profile of KTZ from the supramolecular complex by the dialysis method

The *in-vitro* release study consisted of the following steps: (i) methanolic solutions of pure **KTZ** and supramolecular complex **KTZ-PAMAM-G5-NH$_2$** (concentration 2 mg/mL relative to **KTZ**) are transferred to cellulose dialysis bags (MCO=14000 Da, Sigma Aldrich); (ii) dialysis bags are placed in beakers, each containing 40 mL double-distilled water, under magnetic stirring at room temperature; (iii) samples of 1 mL each are collected from the external aqueous phase at different time intervals (15 min ÷ 24 h), supplementing the external phase with 1 mL double-distilled water at each extraction; (iv) the accumulation of **KTZ** in the external aqueous phase by diffusion from the dialysis bags was followed by measuring the absorbance at 230 nm. Previously, the calibration curve was drawn using dilutions of known concentrations of **KTZ** stock solution (0.19 mM in H$_2$O:CH$_3$OH 1:1 (v:v)).

UV-VIS Spectrophotometer Jasco V-750, (Able Jasco, Japan) was used to estimate the amount of drug incorporated in the dendrimer, with characteristics: wavelength range: 160-900 nm, speed of variable scanning between 10 ÷ 4000 nm/min, scanning speed at spectral preview of 8000 nm/min. The measurements were made in quartz cells, using H$_2$O:CH$_3$OH 1:1 (v:v) mixture, solvents of analytical purity, as internal standard.

Cell viability

Cytotoxicity of the **KTZ**, **PAMAM-G5-NH$_2$** dendrimer, and **KTZ-PAMAM-G5-NH$_2$** supramolecular complex was tested on two human cell lines: human dermal fibroblasts (BJ, ATCC CRL-2522™Manassas, Virginia, USA) and hepatocellular carcinoma (HepG2-HB-8065, ATCC). Cells were maintained in DMEM (Dulbecco's Modified Eagle Medium) with high glucose, supplemented

with 5% fetal calf serum and penicillin/streptomycin, amphotericin (all purchased from Biochrome AG, Berlin, Germany), in standard culture conditions, medium was changed twice a week.

All compounds were dissolved in DMSO to make a stock solution of 10 mg/mL, and then the solutions were further diluted with medium to reach the final concentrations, used to treat the cells. Final DMSO concentration was <0.5%, nontoxic to the cells. Briefly, 104cells/well were seeded for 24h on 96 well plaques, and then exposed to increasing concentrations of each of the tested compounds 0-100 µg/mL for the dermal fibroblasts and respectively 0-400 µg/mL for the Hep-G2 cells. Cell viability of the cells was assessed by using CellTiter 96® AQueous Non-Radioactive Cell Proliferation Assay (Promega Corporation, Madison, USA), as indicated by the producer, measurement was done at 540 nm. Each experiment was done in triplicate, and the results are expressed as % of untreated control [10].

Epicutaneous auricular sensitization test in mouse model

The epicutaneous auricular sensitization test on an animal model (MEST- mouse ear sensitization test) was performed on the Balc C mouse model, females, 3 months old, average weight 21 g±3g. The animals were purchased from Cantacuzino Institute, (Bucharest, Romania). During the experiments, the animals were kept at humidity 65%, 21 °C, day/night cycles of 12 h, fed with standard food and water ad libitum. The food of the animals was supplemented with vitamin A (250UI/g) to enhance the sensitivity of the epicutaneous sensitization test.

The mice were divided into 5 groups (n=5/group): control – vehicle, 70% ethanol; positive control – 200 µg/mL dinitrochlorobenzene (DNCB) dissolved in 70% ethanol; **KTZ** – 100 µg/mL, dissolved in 70% ethanol; **PAMAM-G5-NH₂** – 100 µg/ml, dissolved in 70% ethanol; **KTZ-PAMAM-G5-NH₂** – 100 µg/mL, dissolved in 70% ethanol. On the first day, Freund's adjuvant (Sigma Aldrich) was injected into the right flank, subcutaneously, to stimulate the allergic response to the test substances [31, 32].

Skin sensitization was performed on the shaved abdominal skin by daily topical application of 100 µL solution for 6 days, followed by the application of 50 µl solution on the right ear on day 8 (challenge=C) and day 15 (rechallenge=R). Ear thickness was measured with a digital caliper before application of the solution (day 8 - initial thickness) and subsequently after each application at 24h (C24h, respectively R24h) and 48h (C48h, respectively R48h). The calculation was made according to the formula: % ear thickness = $100*(A-B)/B$, A = ear thickness after treatment, B = initial ear thickness [31-35].

The mice were followed for signs of distress like loss of appetite, weight loss, hair loss, local pruritus and pain. Macroscopic pictures were taken to document the inflammatory changes in the mice ears.

Statistical analysis

The statistical interpretation of the obtained data was done using the program GraphPad Prism version 4.00 for Windows, Software, San Diego, CA, USA, the one-way ANOVA test, followed by Dunnet's multiple comparations posttest, $p < 0.05$ was considered significant (www.graphpad.com).

ACKNOWLEDGMENTS

REFERENCES

1. A. H. Groll; J. Lumb; *Future Microbiol*., **2012**, *7*, 179-184
2. D. T. Mlynarczyk; J. Dlugaszewska; A. Kaluzna-Mlynarczyk; T. Goslinski; *JCR*, **2021**, *330*, 599-617
3. G. L. Amidon; H. Lennernäs; V. P. Shah; J. R. Crison; *Pharm Res*., **1995**, *12(3)*, 413-420
4. S. Basa; T. Muniyappan; P. Karatgi; R. Prabhu; R. Pillai; *Drug. Dev. Ind. Pharm*., **2008**, *34*, 1209-1218
5. E. N. Lo; L. A. Beckett; C. -X. Pan; D. Robles; J. M. Suga; J. M. Sands; P. N. Lara; *Prostate. Cancer. Prostatic. Dis*., **2015**, *18*, 144-148
6. European Medicines Agency. Ketoconazole HRA; http://www.ema.europa.eu/ ema/index.jsp?curl=pages/medicines/human/medicines/003906/human_med_ 001814.jsp&mid=WC0b01ac058001d124
7. F. D. Choi; M. L. W. Juhasz; N. A. Mesinkovska; *J. Dermatolog. Treat*., 2019, *30(8)*, 760-771
8. F. A. Martin; M. M. Pop; G. Borodi; X. Filip; I. Kacso; *Cryst. Growth. Des.,* 2013, *13(10)*, 4295-4304
9. I. Kacso; L. M. Rus; F. Martin; M. Miclaus; X. Filip, M. Dan; *J. Therm. Anal. Calorim.,* **2021**, *143*, 3499-3506
10. F. Martin; M. Pop; I. Kacso; I. G. Grosu; M. Miclăuş; D. Vodnar; I. Lung; G. A. Filip; E. D. Olteanu; R. Moldovan; A. Nagy; X. Filip; I. Bâldea; *Molec. Pharmaceutics*, **2020**, *17(3)*, 919-932

11. X. Chen; D. Li; Z. Deng; H. Zhang; *Cryst. Growth Des*., **2020**, *20*, 6973-6982

12. A. K. Aggarwal; S. Jain; *Chem. Pharm. Bull.,* **2011**, *59*, 629-638

13. P. K. Mididoddi; M. A. Repka; *Eur. J. Pharm. Biopharm.,* **2007**, *66*, 95-105

14. J. Taraszewska; M. J. Kozbial; *Inclusion Phenom. Mol. Recognit. Chem*., **2005**, *53*, 155-161

15. A.S. Chauhan; *Molecules*, **2018**, *23(4)*, 938-947

16. A. Santos; F. Veiga; A. Figueiras; *Materials*, **2020**, *13(65)*, 1-31

17. V. Patel; P. Patel; J. V. Patel; P. M. Patel; *J. Indian Chem. Society*, **2022**, *99(7)*, 100516

18. N. P. Silva JR; F. P. Menacho; M. Chorilli; *J. Pharma.,* **2012**, *2*, 23-30

19. R.V. de Araújo; S. da Silva Santos; F. E. Igne; J. Giarolla; *Molecules*, **2018**, *23*, 2849-2876

20. K. Winnicka; M. Wroblewska; P. Wieczorek; P.T. Sacha; E. Tryniszewska; *Molecules,* **2012**, *17*, 4612-4624

21. J. Jose; R. N. Charyulu; *Optoelectronics and advanced materials – Rapid Communications*, **2016**, *10(7-8)*, 604–608

22. A. Chauhana; B. Antona; M. K. Singh; Dendrimers for drug solubilization, dissolution and bioavailability, *in Pharmaceutical Applications of Dendrimers*, A. Chauhan, H. Kulhari Eds.; Elsevier, **2019**, Chapter 3, pp. 59-92

23. B. Yavuz; S. B. Pehlivan; N. Unlu; *Sci. World J.,* **2013**, 732340

24. S. Svenson; *Chem. Soc. Rev*., **2015**, *44(12),* 4131-44

25. P. Papneja; M. Kumar Kataria; A. Bilandi; *EJPMR*, **2015**, *2(5),* 990-1014

26. A. Karolewicz; A. Górniak; E. Owczarek; A. Żurawska-Plaksej; J. Pluta Piwowar; *J. Therm. Anal. Calorim*., **2014**, *115,* 2487-2493

27. S. Uppuluri; P. R. Dvornic; J. W. Klimash; P. I. Carver; N. C. Beck Tan; The Properties of Dendritic Polymers I: Generation 5 Poly(amidoamine) Dendrimers, **2022**

28. C. D. Bevan; R. S. Lloyd; *Anal. Chem*., **2000**, *72(8)*, 1781-1787

29. S. D'Souza; *Advances in Pharmaceutics*, **2014**, Art. ID 304757, 1-12

30. J. Jose; R. N. Charyulu; *Int. J. Pharm. Investig*., **2016**, *6(2)*, 123-127

31. J. -L. Garrigue; J. -F. Nicolas; R. Fraginals; C. Benezra; H. Bour; D. Schmitt; *Contact Dermatitis*., **1994**, *30(4)*, 231-237

32. P. S. Thorne; C. Hawk; S. D. Kaliszewski; P. D. Guiney; *Fundam. Appl. Tox.,* **1991**, *17*, 807-820

33. C. G. Shayne; J. D. Brendan; D. W. Dobbs, C. Reilly, R. D.Walsh, *Toxicol and Applied Pharmacol*, **1986**, *84:(1),* 93-114

34. L. Tordesillas; R. Goswami; S. Benedé; G. Grishina; D. Dunkin; K. M. Järvinen; S. J. Maleki; H. A. Sampson; M. C. Berin; *J. Clin. Invest.* **2014**, *124(11)*, 4965-7

35. S. Danescu; G. A. Filip; R. Moldovan; D. Olteanu; A. Nagy; X. Filip; F. Martin; I. Kacso; I. Baldea; *Inflammopharmacology,* **2021**, *29(3)*, 721-733